DISSERTATION

DEVELOPMENT OF A HIGH ENERGY DIODE PUMPED CHIRPED PULSE AMPLIFICATION LASER SYSTEM FOR DRIVING SOFT X-RAY LASERS

Submitted by

Brendan A. Reagan

Department of Electrical and Computer Engineering

In partial fulfillment of the requirements

For the Degree of Doctor of Philosophy

Colorado State University

Fort Collins, Colorado

Spring 2012

Doctoral Committee:

Advisor: Jorge Rocca

Carmen Menoni
Mario Marconi
David Krueger

ABSTRACT

DEVELOPMENT OF A HIGH ENERGY DIODE PUMPED CHIRPED PULSE AMPLIFICATION LASER SYSTEM FOR DRIVING SOFT X-RAY LASERS

There is significant interest in the development of compact high repetition rate soft x-ray lasers for applications. This dissertation describes the development of a high energy, laser diode pumped, chirped pulse amplification laser system for driving soft x-ray lasers in the 10-20 nm spectral region. The compact laser system combines room temperature and cryogenically-cooled Yb:YAG amplifiers to produce 1.5 Joule pulses at up to 50 Hz repetition rate. Pulse compression results in 1 J pulses of 5 ps duration. A room temperature pre-amplifier maintains bandwidth for short pulse operation and a novel cryogenic cooling technique for the power amplifier was developed to enable high average power operation of this laser. This laser was used to drive a soft x-ray laser on the 18.9 nm line of nickel-like molybdenum. This is the first demonstration of a soft x-ray laser driven by an all diode-pumped laser.

TABLE OF CONTENTS

Chapter 1

Introduction

1.1 Extreme Ultraviolet and Soft X-Ray Radiation

Throughout history scientists and engineers have used electromagnetic radiation to study and manipulate the universe around them. The visible region of the spectrum was, as expected, the first to be understood and developed. The rest of the spectrum ranging from radio waves, with wavelengths of meters and longer, to gamma rays, with wavelengths shorter than the diameter of atomic nuclei was later discovered, and electromagnetic radiation sources have been developed leading to numerous discoveries and applications. Following its first demonstration in 1960 [1], the laser has become one of the most important tools in experimental physics and one of the most important devices for enabling advancements in technology. However, the extreme ultraviolet (EUV) and soft x-ray region of the spectrum has remained relatively unexplored [2]. This region, shown in Figure 1.1, bridges the gap between vacuum ultraviolet radiation and hard x-rays. Although there is no universally agreed upon definitions of where the EUV and soft x-ray regions of the spectrum begin and end, photon energies from about 25 eV to the carbon k-shell absorption edge at 275 eV (wavelengths from 40 nm to 5 nm) are generally referred to as extreme ultraviolet

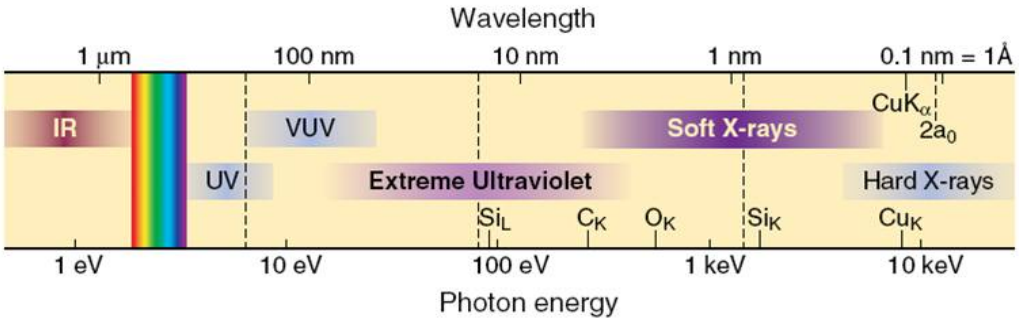

Figure 1.1: The extreme electromagnetic spectrum where the EUV and soft x-rays occupy the region between the vacuum ultraviolet and hard x-rays. From [2]

while the soft x-ray region extends from 275 eV to several keV (5 nm to 0.3 nm). The soft x-ray laser community defines this entire region as soft x-rays. The many atomic resonances make this an interesting region for spectroscopic studies of elements and molecules [2]. Additionally, there are many applications of this radiation that take direct advantage of the short wavelength such as high resolution microscopy [3, 4, 5] and nanopatterning [6, 7]. This comes from the fact that the smallest feature that can be resolved in a microscope or printed via lithography, $\Delta r_{\text{Rayl.}}$, is proportional to wavelength and is given in [2] as:

$$\Delta r_{\text{Rayl.}} = \frac{0.610\lambda}{NA} \tag{1.1}$$

where NA is the numerical aperture of the optical system. For this reason the semiconductor indsutry is investing heavily to develop EUV lithography to print the next generation of microprocessors [8]. Furthermore, in addition to the exploitation of the high energy and short wavelength characteristics of EUV and soft x-rays, the high intrinsic bandwidth of this radiation is being used to generate extremely short duration optical pulses. While visible and near infrared (NIR) laser pulses are limited in duration by their optical cycle to a few femtoseconds, intense EUV pulses created through high harmonic generation can have durations on the order of hundreds of attoseconds [9, 10, 11], and potentially even shorter [12, 13]. These ultrashort pulses are currently

being used to probe the dynamics of atomic electrons with unprecedented temporal resolution.

Just as the invention of the laser revolutionized the field of infrared and visible optics, the further development of coherent EUV sources can be expected to advance science and technology. Currently there are four main sources of EUV radiation: synchrotrons, free electron lasers (FEL), high harmonic generation (HHG), and soft x-ray lasers. The former two sources currently require large facilities, while the latter two can be compact and constructed in modest-sized laboratories.

Synchrotrons are large cyclic particle accelerators in which the accelerated particles are are guided into a circular path by magnetic fields. In synchrotron radiation sources, electrons are accelerated to relativistic speeds, typically with GeV energies. When these electrons are accelerated, such as by the magnetic fields that confine the beam on a circular path a broad bandwidth cone of radiation is emitted [14]. Older, second generation synchrotron radiation sources were constructed with beam ports to use the emitted radiation. Newer, third generation synchrotron sources are constructed with many straight sections where the electrons propagate through a periodic magnetic field created by a an undulator or a wiggler [2]. The radiation emitted can be filtered both spatially and in frequency resulting improved coherence. Synchrotrons are high average power, wavelength-tunable sources EUV and soft x-ray radiation.

In free electron lasers, a beam of high energy electrons is created by a linear accelerator. These high energy electrons are passed through a wiggler emitting radiation. Since the electron motion is in phase with the radiation the emission is coherent. The emitted radiation is wavelength-tunable, has high spatial coherence, partial temporal coherence, and reaches unsurpassed peak spectral brightness for EUV and soft x-ray sources [15, 16]. Seeding these sources with low energy, temporally coherent pulses, created through high harmonic generation results in improved temporal coherence

[17]. FELs and synchrotrons are high power sources of EUV and soft x-ray radiation, however they are large, expensive, and are few user (synchrotron) or single user (FEL) facilities.

The two main approaches to compact sources of coherent EUV radiation are up-conversion of short near infrared (NIR) or visible laser pulses through high harmonic generation and soft x-ray lasers. In HHG, high intensity laser pulses, usually a few 10s of femtoseconds in duration, are focused into a medium, usually a noble gas. Through a nonlinear interaction between the intense laser field and the bound electrons of the gas, photons with odd integer multiples of the laser frequency are generated. These newly-created photons are generated in phase with the driving laser and retain the same polarization and k-vector and are therefore both spatially and temporally coherent [18]. The spectrum resulting from HHG is a broad frequency comb extending from the driving laser wavelength into the EUV and soft x-ray regions of the spectrum. The highest photon energy created is proportional to the driving laser intensity [19, 18]. Soft x-ray lasers can also be quite compact sources. In these sources, the lasing medium is always a plasma created either by a fast electrical discharge or by an intense optical laser. The pulses produced by soft x-ray lasers are usually significantly higher energy than that produced by HHG and are more monochromatic, but they are also longer duration and usually operate at lower repetition rate. These lasers are discussed in detail in the following section.

1.2 Soft X-Ray Lasers

From an atomic point of view the excitation mechanism used to develop lasers operating at EUV and soft x-ray wavelengths is fundamentally the same as lasers in the visible and infrared. They require there to be an external energy source to create a population inversion between two electronic energy levels of an atom or molecule

resulting in stimulated emission. However, visible and infrared laser transitions have energies of less than a few eV while soft x-ray lasers have energies of greater than 30 eV, which is greater than the ionization energy of any neutral element. Therefore, these lasers operate in ions that have higher energy transitions than neutral atoms. For this reason, most atomic soft x-ray lasers demonstrated to date make use of very hot dense plasmas. As hot dense plasmas tend to expand and cool very quickly, the gain duration of soft x-ray lasers is typically very short, lasting from about a picosecond up to nanoseconds depending on the excitation scheme. This, combined with the unavailability of high reflectivity mirrors at these wavelength severely limits the use of optical cavities used in visible and infrared lasers. Consequently, the vast majority of soft x-ray lasers demonstrated to date are single-pass amplified spontaneous emission (ASE) lasers, in which spontaneous emission from one end of the plasma is amplified through stimulated emission as it traverses the active region. There are however distinct techniques for achieving population inversion at these wavelengths: collisional pumping of the laser upper level through electron impact excitation, recombination into an excited state, and inner-shell photoionization lasers. The following section describes these techniques as well as relevant demonstrations of these lasers.

1.2.1 Soft X-ray Laser Schemes

Recombination soft x-ray lasers

The first experimental achievement of population inversion at EUV wavelengths was reported in 1974 in a hydrogen-like carbon plasma [20]. In this and following experiments a solid carbon target was ablated by an intense laser pulse producing a fully-ionized plasma, in other words effectively all bound electrons are stripped from the carbon nuclei [20, 21]. As this plasma expands and cools, free electrons recombine forming H-like C ions. This takes place through three-body recombination in which an electron recombines while a second free electron carries away the excess energy lost

by the newly bound electron. Three-body recombination preferentially populates the higher energy levels, and, as the bound electron cascades down through the excited states, a population inversion can be created on the Balmer α (n=3 n=2) transition. As can be shown from basic quantum mechanics, the energy levels of H-like ions scale as:

$$E_{\mathrm{n}} = -13.6\frac{Z^2}{n^2}(eV) \tag{1.2}$$

where Z is the nuclear charge. For H-like carbon (Z=6), the ionization energy (the energy required to remove the last electron) is 490 eV, and the wavelength of Balmer α transition shifts from 656nm in the visible with Z=1 to 18.2 nm in the EUV with Z=6. Gain through recombination into excited states has also been demonstrated on the Lyman α (2p 1s) transition of H-like Li at 13.5 nm by coupling intense laser pulses into LiF microcapillaries [22]. In order for a large population inversion to occur in these lasers, the electron temperature, $\mathrm{T_e}$, must cool very quickly after achieving full ionization because the rate of three body recombination is proportional to ${T_{\mathrm{e}}}^{-9/2}$. This is difficult to achieve, and these lasers have not yet achieved gain saturation. Nevertheless, the first demonstration of large amplification of a soft x-ray laser was realized by Suckever et al [23] on the 18.2 nm line of C VI in a plasma column confined by a magnetic field.

Photoionization soft x-ray lasers

A second type of soft x-ray laser is the photoionization laser in which an inner shell electron of a neutral atom or ion is liberated by a single high energy photon. This leaves the ion in a highly excited state, with a very short lifetime, from which stimulated emission can occur. A number of lasers of this type have been demonstrated in the visible and vacuum ultraviolet [24, 25], however, until very recently, none had been demonstrated at EUV or soft x-ray wavelengths. A soft x-ray photoionization laser was first proposed in 1967 [26], and their study was later expanded upon in the

1970's [27] and in the 1990's [28]. A photoionization laser in which a column of neon gas is irradiated by femtosecond pulses of 1 keV photon energy from the Stanford Liniac Coherent Light Source (LCLS) FEL [16] was demonstrated to produce laser emission at 849 eV [29]. This is the shortest wavelength atomic laser demonstrated to date.

Collisional soft x-ray lasers

The most successful plasma-based soft x-ray lasers demonstrated so far have been collisionally driven. In these lasers, the laser upper laser level is pumped through electron impact excitation in a similar fashion to visible gas discharge ion lasers such as the well-known argon-ion laser which emits on several blue and green lines [30]. In these ion lasers, neutral argon atoms are ionized through electron collisions. The upper laser level in the Ar^+ ions is subsequently populated by electron impact excitation leading to a population inversion and gain. Collisional soft x-ray lasers function in essentially the same manner, however instead operating in singly or doubly ionized plasmas, they operate with much higher levels of ionization. Collisional EUV lasers were first proposed in the 1970s [31, 32], and the first demonstration of a collisional soft x-ray laser in was made in a plasma in which selenium atoms were 24 times ionized to the Ne-like configuration [33]. This plasma was generated by focusing kilojoule-level laser pulses of 450 ps duration into a 1 cm long by 200 μm wide line on a thin foil that was coated with Se. The plasma was heated through inverse-bremsstrahlung or free-free absorption of the laser energy by free electrons. In this work, clear evidence of lasing with gain-length products up to 6.5 cm^{-1} was observed on two lines of Se^{+24} near $\lambda = 21$ nm.

It is possible to produce thermalized and transient plasmas in which a large fraction of the ions are in the Ne-like state. This is because the Ne-like ion state , with 10 electrons, is a closed-shell configuration and therefore the energy required to ionize

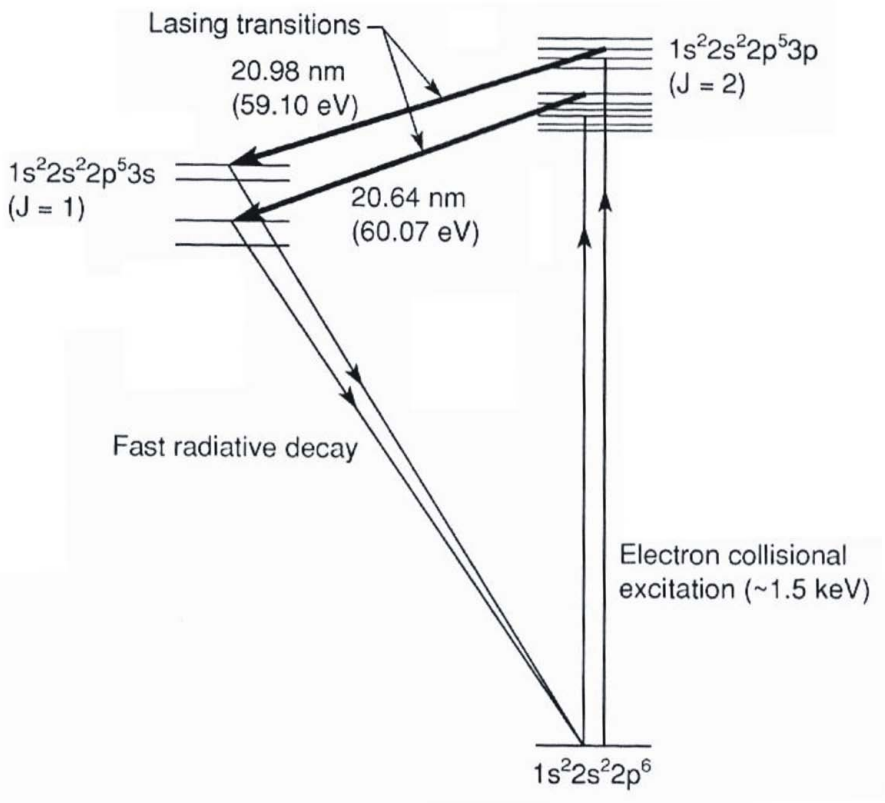

Figure 1.2: Energy level diagram of the Ne-like selenium ion showing the two laser lines and the most important processes from [2]. Although Ne-like Se is shown the diagram is representative of all Ne-like ions.

from the next lower ionization state (Na-like) is much lower than that required to ionize a Ne-like ion. For example, the energy required to ionize Na-like selenium to the Ne-like state is 1036 eV, while the energy required to ionize Ne-like Se is 2540 eV [2]. A plasma with a temperature around 1 keV leads to a large number of Se atoms in the Ne-like state. A simplified Grotrian diagram of the Ne-like laser system is shown in Figure 1.2. Monopole electron impact excitation from the ground state of the ion produces a large population on the 3p laser upper levels as radiative decay to the ground state is forbidden. The 3s laser lower levels are quickly depleted through radiative decay leading to a large population inversion. Figure 1.3 shows the laser wavelengths of the Ne-like isoelectronic series as a function of ion charge. Also shown in Figure 1.3 is the wavelength of the $3d^9 4d \quad 3d^9 4p$ lasing transition

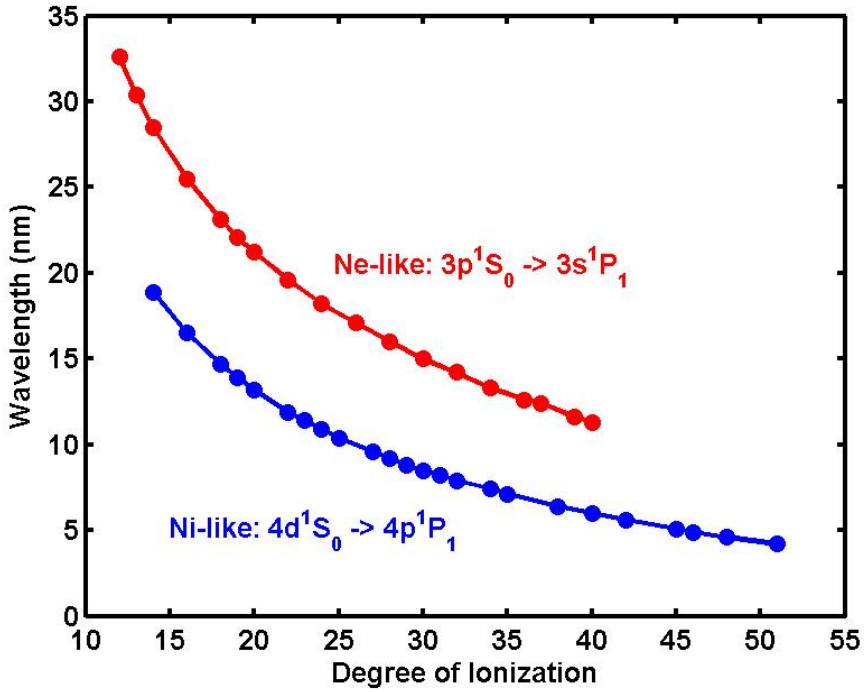

Figure 1.3: Lasing wavelengths of Ne-like and Ni-like soft x-ray lasers as a function of ion charge.

of the Ni-like isoelectronic series, which is also a favorable soft x-ray laser system. The Ni-like system has several advantages over the Ne-like series that allow shorter wavelength lasers to be generated with lower plasma temperatures and therefore less driving laser energy. The laser transitions scale to shorter wavelength faster with degree of ionization, as shown in Figure 1.3. Figure 1.4 shows a simplified energy level diagram for Ni-like Mo, which lases on the $4d^1S_0 \quad 4p^1P_1$ transition at a wavelength of 18.9nm. A number of Ne-like and Ni-like lasers have been demonstrated at a variety of wavelengths, with the shortest being at 3.56 nm in Ni-like Au [34]. A significant advance in the development of collisional soft x-ray lasers was transient excitation utilizing two or more laser pulses to create and rapidly heat the plasma [35]. In this scheme, a pulse of modest intensity ablates a solid target, creating a plasma. After allowing the plasma to expand for a duration up to several nanoseconds, a second short pulse (typically 1-10 picoseconds) rapidly heats the plasma causing a large pop-

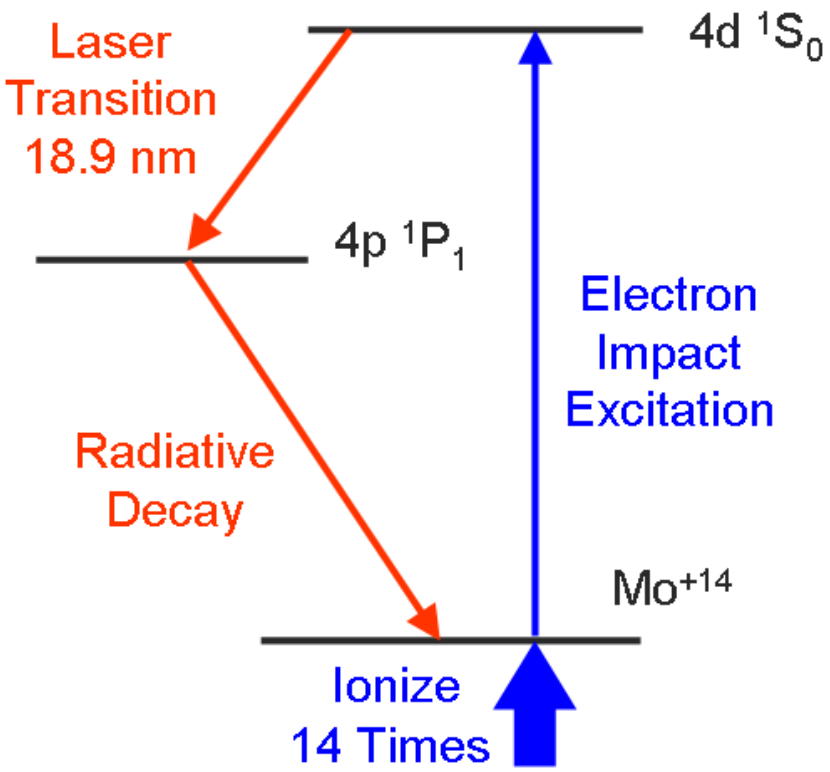

Figure 1.4: Simplified energy level of nickel-like molybedum, showing the laser transition at 18.9nm. Although Ni-like Mo is shown this diagram is similar for all Ni-like isoelectronic configurations.

ulation inversion and high gain [36]. This technique has been used to reduce the total laser energy required to pump soft x-ray lasers from hundreds of Joules to ≈10 J [36]. Using this technique, a number of Ne-like and Ni-like lasers have been demonstrated to reach gain-saturation [37], where a large fraction of the energy stored in population inversion is extracted by the soft x-ray laser pulse.

Another technique to drive collisional soft x-ray lasers consists in the use of ultrashort laser pulses to quickly ionize a column of gas through optical field ionization (OFI) in which the electric field of the laser is strong enough to suppress the Coulomb potential binding electrons to the parent nucleus [38]. In this regime, bound electrons can tunnel-ionize through this suppressed potential. If the laser pulse is sufficiently intense, high ionization states can be achieved. Furthermore, by circularly polarizing the driving laser, the freed electrons can retain a large portion of the ponderomotive

energy, the total energy of the electron in an oscillating electric field. This allows them to efficiently pump the soft x-ray laser upper level in Ni-like and Pd-like ions by collisional excitation [39, 40]. These lasers, while not achieving the pulse energies of other soft x-ray lasers, require significantly less driving laser energy, typically hundreds of millijoules.

Another type of collisional soft x-ray laser is the capillary discharge driven soft x-ray laser [41]. The most succseful demonstration of this type of soft x-ray laser is the Ne-like argon laser which lases most strongly at 46.9 nm. In this demonstration, a short, several tens of kA amplitude current pulse is driven through a capillary tube containing argon at low pressure. Using this scheme, a compact setup has been demonstrated to generate laser pulse energies greater than 100 μJ at repetition rates up to 10 Hz, allowing high average power operation [42]. This laser has enabled many applications including interferometry of dense plasmas [43], nanopatterning [6, 7], and high resolution microscopy [4].

1.2.2 Laser-driven compact soft x-ray lasers

A significant reduction of laser pump energy required to drive soft x-ray lasers can be achieved by heating the plasma at grazing incidence. This reduces the size and complexity of these sources and allows higher repetition rate operation. In the traditional normal incidence pumping configuration a large portion of the pump energy is absorbed in a region of the plasma where density gradients cause strong refraction, limiting effective amplification. The index of refraction of a plasma is usually dominated by the free electron contribution and is given by:

$$n = \sqrt{1 - \frac{n_e}{n_c}} \tag{1.3}$$

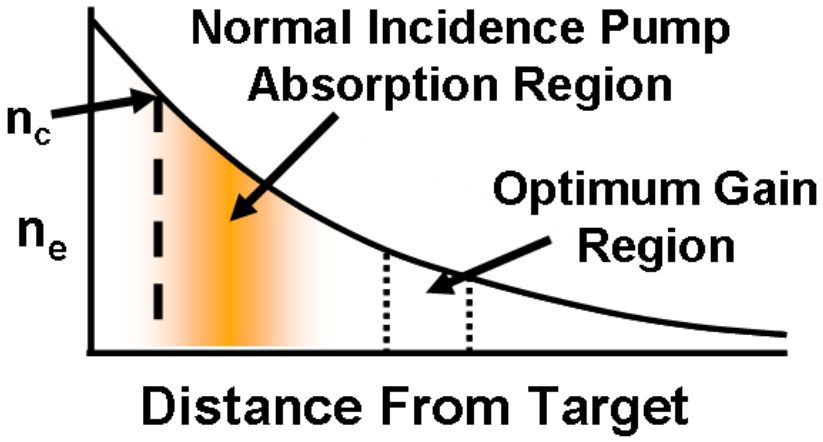

Figure 1.5: Electron density (n_e) of a laser created plasma as a function of distance from the solid target surface. For laser pulses that impinge at normal incidence most of the laser energy is deposited near the critical density (n_c). In this region there are strong density gradients that refract the beam out of the gain region.

where n_e is the electron density and n_c is the critical density. n_c is wavelength-dependant and is given by:

$$n_c = \frac{\epsilon_0 m_e}{e^2}\omega^2 \approx \frac{1 \times 10^{21}}{\lambda^2(\mu m)}(cm^{-3}). \tag{1.4}$$

In this equation, ϵ_0 is the permittivity of free space, m_e and e are the electron mass and charge, respectively, and ω is the radial frequency of the electromagnetic wave. The critical density for a given wavelength is defined as the electron density at which the plasma frequency, the frequency at which free electrons will naturally oscillate, is equal to the frequency of the radiation. At plasma densities above the critical density, light can no longer propagate and is reflected. For plasmas created through laser ablation of a solid, the density is usually highest near the target surface and decreases approximately exponentially with distance as shown in Figure 1.5. The laser energy is mostly deposited in the region near the critical density. At this region of the plasma, strong density gradients cause an index of refraction that is lowest near critical density and increasing with distance from the target. This strongly refracts the x-ray emission limiting the achievable amplification. The optimal density

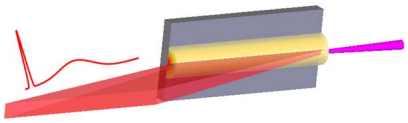

(a)

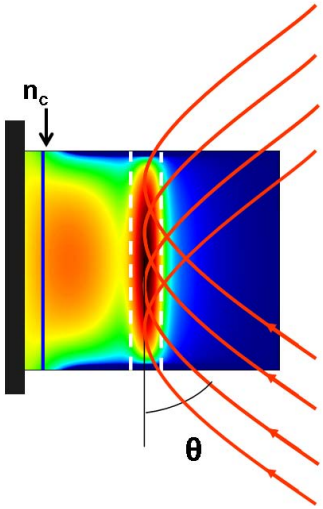

(b)

Figure 1.6: (a) Illustration of grazing incidence pumping. (b) Total external reflection allows the penetration depth of the laser to be tuned by changing the grazing incidence angle θ.

region for amplification occurs at lower density. However, this lower density region is not efficiently pumped by normal incidence laser pulses. It was recognized that this limitation can be overcome by heating the plasma at grazing incidence [44]. In this configuration, the laser heating pulse is focused into a preformed plasma at a grazing incidence angle as shown in Figure 1.6(a). Because of total external reflection within the plasma (as can be seen from equation 1.3 the refractive index of a plasma is less than 1) the laser pulse does not penetrate all the way to the critical density. Instead, for an angle of incidence θ it is refracted back when it reaches a density n_{em}:

$$sin\theta = \sqrt{\frac{n_{em}}{n_c}}. \tag{1.5}$$

It is clear that by adjusting the angle of incidence, it is possible to efficiently pump the plasma region where the conditions are most favorable for laser amplification. Fig-

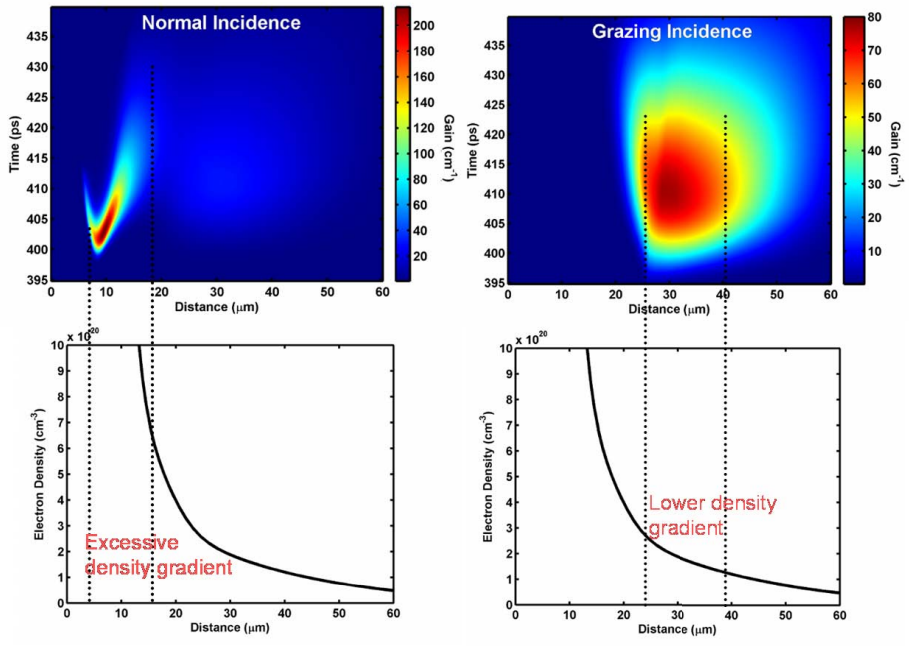

Figure 1.7: Simulated small signal gain and electron density for Ni-like Pd 14.7 nm lasers driven at normal incidence and at 20° grazing incidence. At normal incidence, the peak gain occurs in a region of the plasma with large density gradients that rapidly refracts the beam out of the narrow gain region. At grazing incidence the pump beam heats the plasma at a lower density producing a large gain region with lower density gradients. The plasma was created by 120 ps, $2.4 \times 10^{12} \frac{W}{cm^2}$ prepulse with a 8 ps, $8 \times 10^{13} \frac{W}{cm^2}$ arriving 300 ps later. This model was developed by Mark Berrill at Colorado State university. From [45].

ure 1.7 shows simulated small signal gain maps and plasma densities for a palladium target pumped at normal and grazing incidences. As can be seen from this figure, while the gain is higher for normal incidence pumping, it exists in a dense region of the plasma with strong gradients which have correspondingly strong refraction. When pumped at grazing incidence the gain exists in a larger region with relaxed density gradients. An added benefit of grazing incidence pumping is that it naturally accomplishes travelling wave excitation. This can be important if the population inversion lasts for a duration comparable to or shorter than the time it takes light to traverse the plasma.

In 2003, two groups demonstrated lasing at 18.9nm in Ni-like Mo using the grazing

incidence pumping technique [46, 47]. In [46], only 150 mJ of total pump power was used to observe lasing. In this experiment a 70 mJ pulse with a duration of 200 ps was focused into a 15 um x 5mm long line on a molybdenum target at normal incidence. After allowing the plasma to expand for an optimum delay of 500 ps, a 2 ps, 80 mJ laser pulse was focused into an overlapping line at a grazing incidence angle of $\theta = 14^{\circ}$ producing lasing at 18.9nm. This laser operated at 10 Hz repetition rate. In the same year, using a similar setup researchers at Colorado State University demonstrated gain-saturation of this laser line using 1.35 J of total pump power at 5 Hz repetition rate. In this experiment, lasing was also observed on the 22.6 nm line of Ni-like Mo. Additionally, a number of other Ni-like lasers at wavelengths as short as 10.9 nm [48, 49, 50] have been demonstrated with less than 2 J of total pump power as illustrated in Figure 1.8 [48]. By increasing the total pump energy to 5 J, a 20 μW average power laser at 13.9 nm was achieved using this scheme [51] along with saturation of Ni-like Te at 10.9 nm [52]. These lasers were used to implement a soft x-ray microscope in transmission [53] and reflection [5] modes with resolutions of 38 nm and 55 nm respectively. Furthermore, the spatial and temporal coherence of these lasers was demonstrated to be significantly improved by seeding the plasma with femtosecond high harmonic pulses. This scheme resulted in high brightness, phase-coherent pulses ranging from 32 nm to 13.2nm [54, 55, 56].

An increase in the average power of these compact and soft x-ray lasers will enable a number of applications at these wavelengths such as some types of microscopy [5], nanopatterning [6, 7], and nanomachining [57]. The average power of these lasers is limited by the repetition rate of the driving laser. In all previous work to date, the driving lasers were flashlamp-pumped, high energy chirped pulse amplification (CPA) lasers which, as discussed in the following section, are limited to pulse repetition rates of less than 10 Hz. Additionally, the physical size, power supplies and cooling requirements for flashlamp-pumped lasers leads to these laser systems occupying a

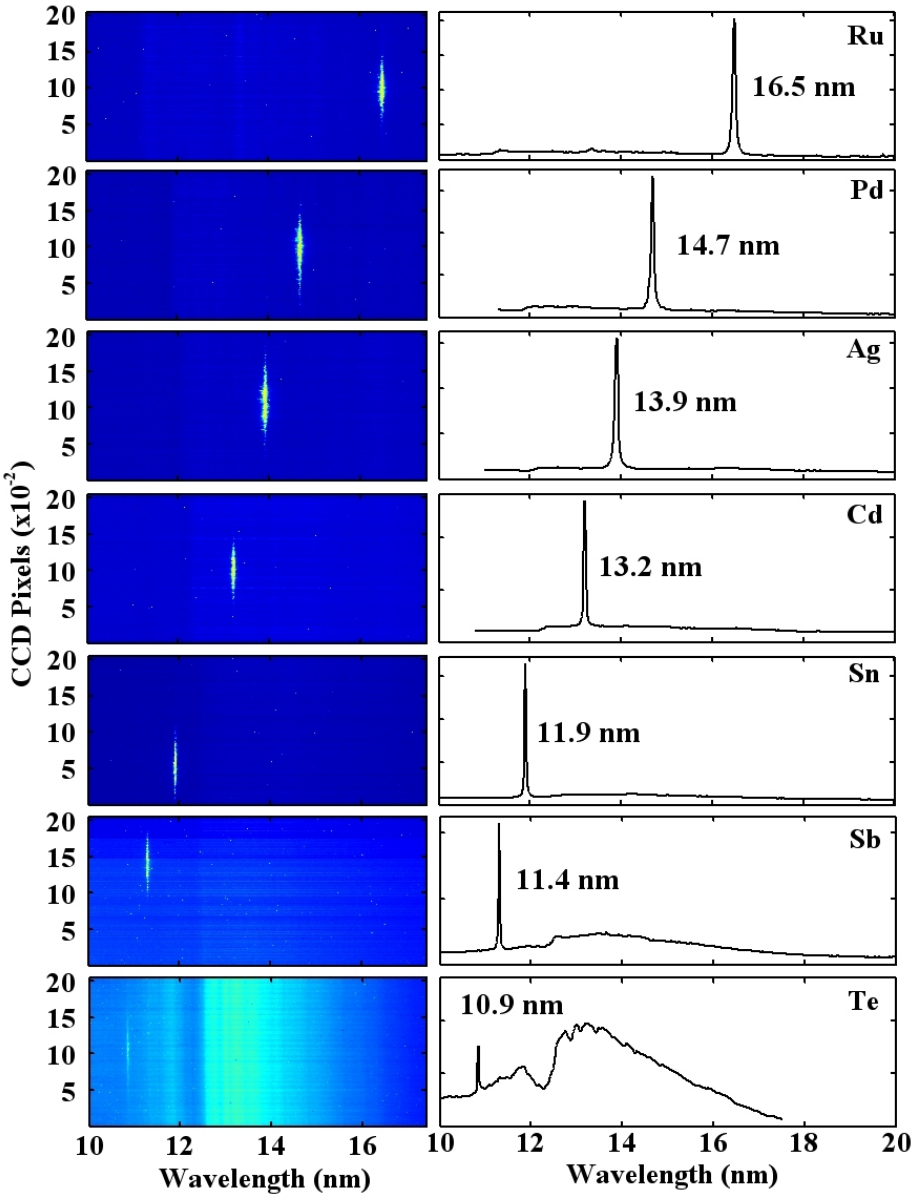

Figure 1.8: Extreme ultraviolet spectra of Ni-like lasers between 16.5nm and 10.9nm. From ref. [48]

significant amount of optical table area. A method to increase the average power and further decrease the size of soft x-ray lasers is to directly pump the driving laser with laser diodes. This is the subject of the work described in this dissertation and is addressed in more detail in the following sections.

1.3 Chirped Pulse Amplification Lasers

The primary technique for generating high energy laser pulses with pulsewidths of less than 100 ps is chirped pulse amplification (CPA). In this technique, first demonstrated in 1985 [58], temporal stretching prior to amplification avoids optical damage and nonlinear effects that are possible with high intensity laser pulses. Short duration laser pulses of initially low energy are stretched in time, amplified in one or more amplifiers to high energy, and subsequently compressed in time producing high energy, short duration laser pulses. This process is shown schematically in Figure 1.9.

The initial low energy, short duration pulses are typically generated by a mode-locked oscillator. In these laser oscillators, many longitudinal cavity modes are made to oscillate in phase. Since the spacing of cavity modes in frequency is equal to the inverse of the cavity round trip time, interference of multiple modes results in a train of pulses spaced in time by the round trip delay. The temporal pulsewidth depends on the bandwidth determined by the number of oscillating modes. A more detailed description of mode-locking is given in Section 2.3. Typical mode-locked oscillators produce pulses with energies of 1-50 nJ and durations ranging from a few femtoseconds in octave-spanning titanium sapphire oscillators [59] to hundreds of picoseconds in narrow bandwidth laser materials. The repetition rate of such oscillators is typically in the range of 10 MHz to several hundred MHz depending on cavity length.

To stretch the laser pulses, a strongly dispersive element is used to add a wavelength dependant delay. As the short pulses are necessarily broad bandwidth, this

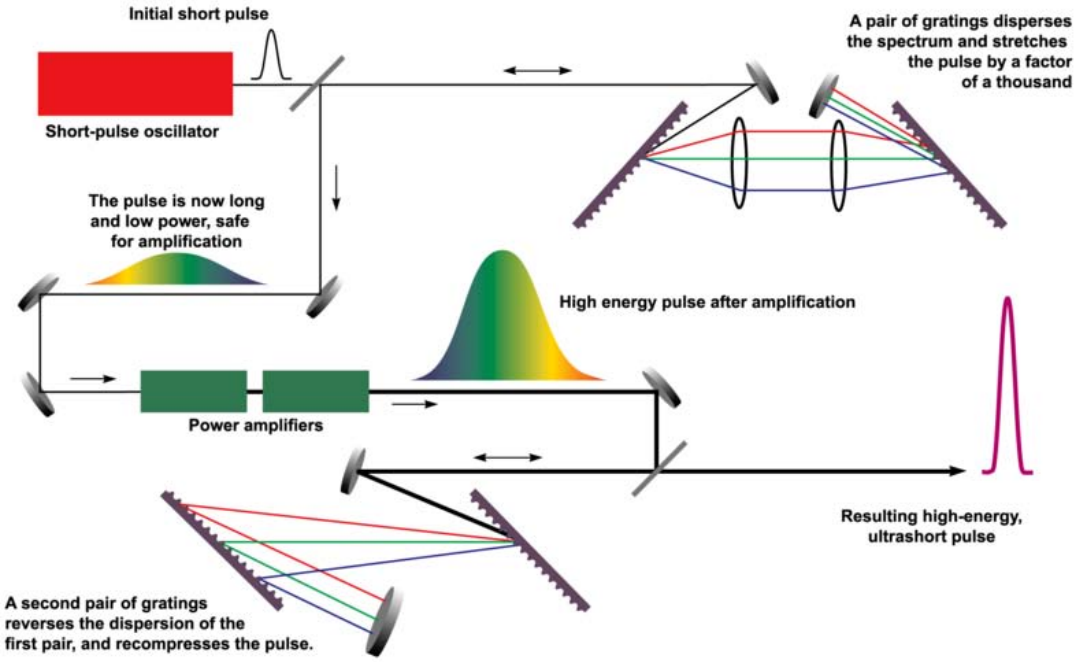

Figure 1.9: Schematic of the chirped pulse amplification process. From ref. [60]

allows the different spectral components to separated in time. This time-dependant frequency is the origin of the term "chirp" in this context. Several techniques have been used to accomplish this dispersion including a pair of diffraction gratings, bulk dispersion (in glass for example), optical fibers, a pair of prisms, and dispersive multilayer coatings (commonly called chirped mirrors). The first is the most commonly used technique. The dispersion acquired by passing a laser pulse through a pair of parallel gratings was first described in 1969 by Treacy [61]. He showed that for any angle of incidence and grating separation the group delay dispersion (GDD), which is the first order variation of delay with wavelength, is always negative (known as anomalous dispersion). This means that short wavelengths travel a shorter distance than the long wavelengths. The dispersion associated with transmission through most transparent materials, such as glass, is usually positive (normal dispersion), and the first CPA systems used a long optical fiber with positive dispersion to stretch the pulse and a Treacy grating pair with negative dispersion to compress the amplified laser pulses [58]. In 1984, Martinez demonstrated that a grating pair with a pair of

lenses forming a telescope between the gratings can be used as positive dispersion stretcher [62]. A visual way to understand this is to recognize that the telescope forms an image of the first grating *behind* the second grating resulting in a negative path length and therefore opposite signed-dispersion (positive dispersion). For an appropriately designed grating stretcher and grating compressor, there can be zero net dispersion allowing perfect compression of optical pulses. In the implementation in real CPA laser systems, the compressor is on purpose not perfectly matched to the stretcher in order to compensate for dispersion within the amplification system, such as the material dispersion of the gain material. Using this technique, amplified pulse durations can be achieved that are nearly bandwidth-limited.

Technically, any laser material may be used as the amplification medium in CPA systems. However nearly all modern CPA system employ solid state laser materials in which the lasing atom is an ion dopant in a crystal or amorphous material such as silicate or phosphate glasses. For these systems the most common dopants are transition metals such as chromium and titanium or rare earth elements such as neodymium, ytterbium, and erbium. The majority of these systems have made use of titanium^{3+}-doped sapphire (Ti:Al_2O_3) or neodymium^{3+}-doped glass (Nd:glass). Both materials emit in the NIR and are 4-level laser systems with broad absorption and emission spectra [63]. Nd-doped materials can lase at several NIR wavelengths but most commonly are operated at λ = 1050 - 1065 nm. A variety of glasses have been specially developed to host Nd, and typically the Nd:glass laser transition has a bandwidth of 15-30 nm FWHM capable of supporting sub-500 fs laser pulses. The upper laser level in Nd:glass has a lifetime around 300 μs and can be pumped from the ground state by several absorption lines in the visible and NIR. Because of these spectral characteristics Nd:Glass is nearly always pumped by flashlamps which emit pulse of hundreds of microsecond duration over a broad spectrum. The highest energy CPA lasers developed implement flashlamp-pumped Nd:glass amplifiers. These

include petawatt peak power laser pulses[1] [64]. The average power and therefore repetition rate of all solid state lasers is limited by the onset of thermal effects. These include: thermal focusing, in which the thermal gradient within the lasing material leads to a refractive index profile that can reduce the beam quality and eventually cause optical damage, and thermal birefringence which leads to a spacial depolarization of the beam. In the very high power regime, strong thermal gradients can lead to stress fracture of the laser material. Nd:glass has a low thermal conductivity of 0.8-1.5 $\frac{W}{mK}$ which, combined with flashlamp restrictions, limits the repetition rate of these lasers to typically less than 10Hz. In many cases, high energy Nd:glass systems are operated in a single shot regime.

Ti:Al_2O_3 has an exceptionally broad fluorescent bandwidth of 230 nm centered at $\lambda = 790$ nm. This bandwidth can support pulse durations under 5 femtoseconds. Ti:Al_2O_3 also has a high stimulated emission cross section that resuls in a low saturation fluence which allows efficient energy extraction with moderate laser fluences. However, this broad bandwidth and high gain is accompanied by a short upper laser level lifetime of 3.2 μs, which requires very short duration pump sources for pulsed operation. Because of this, Ti:Al_2O_3 amplifiers are usually pumped with frequency-doubled nanosecond pulses from flashlamp-pumped Nd lasers. The combination of high gain and pump pulses that are significantly shorter than the fluorescent lifetime allow these amplifiers to operate with very high efficiencies. Additionally, sapphire has one of the highest thermal conductivities of any laser host allowing it to support high average power operation. However, the repetition rate and average power of Ti:Al_2O_3 systems is limited by the pump lasers. In practice, the repetition rate of flashlamp-pumped, high energy (>1J) Ti:Al_2O_3 CPA systems is still limited to under 10 Hz by the inefficiencies of flashlamp-pumping.

High energy flashlamps emit over a broad spectral region from the UV to infrared

[1]The first such system was a hybrid Ti:Al_2O_3 - Nd:glass system employing a Ti:Al_2O_3 oscillator and preamplifiers with Nd:glass power amplifiers.

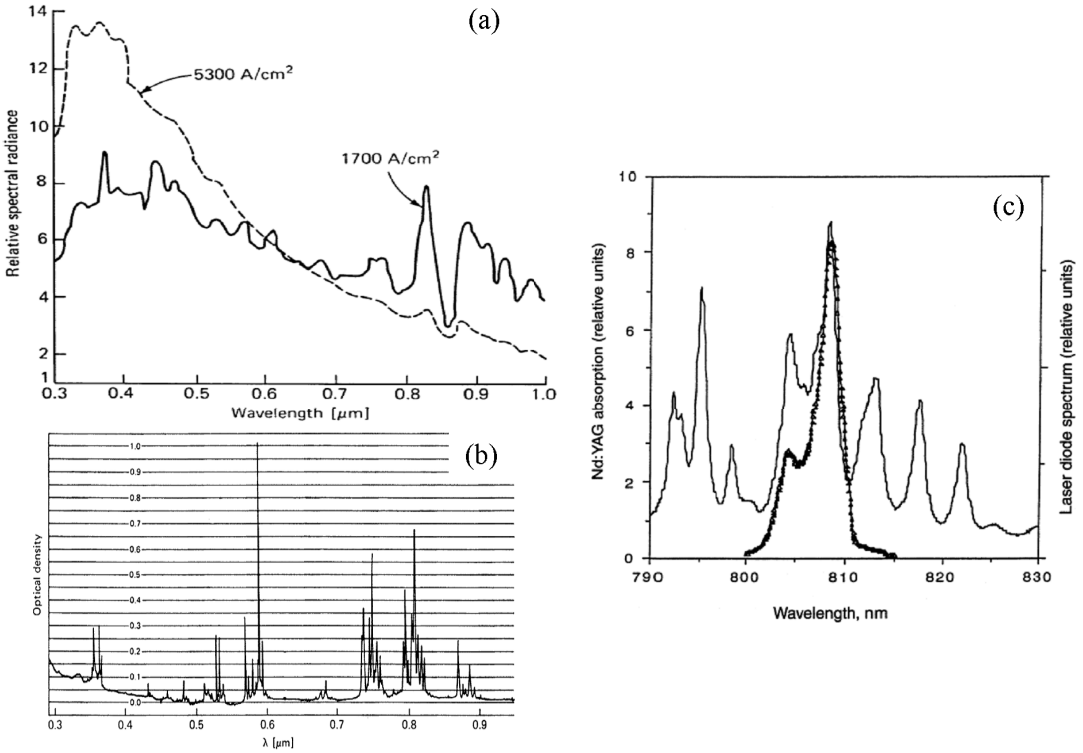

Figure 1.10: a Emission spectra for two different current densities from a flashlamp filled with 0.4 atm xenon. (b) Absorption spectrum of Nd:YAG. (c) Detail of absorption spectrum of Nd:YAG near 808 nm (solid line) and the emission spectrum of a high power GaAlAs laser diode array (bold trace). From ref [63]

as shown in Figure 1.10 (a). However, as can be seen from Figure 1.10 (b), Nd lasers can only absorb light on narrow transitions, principally near 880 nm, 808 nm, 750 nm, and 590 nm. As a result, only a small fraction, typically around 10%, of the light emitted from a flashlamp is useful for pumping these lasers, and the vast majority contributes to heating of the laser medium. This heating complicates the cooling systems that must be used. More importantly, the low efficiency of conversion from electrical energy to *useful* pump light, typically less than 5%, severely limits the average power of flashlamp-pumped lasers.

The major advances in the development of high power laser diodes in the past 20 years allow for a viable alternative to flashlamp pumping. Diode-pumped solid state lasers have several very important advantages over flashlamp driven lasers that

allow them to be much more compact and operate at higher average powers. These advantages are discussed in the following section.

1.3.1 Laser Diode-Pumped CPA Lasers

The primary advantage of laser diodes over flashlamps for pumping solid state lasers is the narrow spectral width of laser diodes that can be made to coincide with absorption bands in the lasing material. High power NIR laser diode arrays usually are made to have a spectral width less 5 nm that can be use to very efficiently pump a single transition. This can be seen in Figure 1.10 (c), which shows the absorption spectrum of Nd:YAG near one of its strongest pump lines at 808 nm. On the same plot, the emission spectrum of a high power array of AlGaAs laser diodes is shown to be very well-matched to this transition. In this case, virtually all light emitted from the laser diode can contribute to pumping the laser upper level. The development of InGaAs laser diodes emitting at 900-980 nm has allowed the advancement of Yb-doped laser materials, which only have a few narrow pump transitions in the NIR which are not efficiently pumped by flashlamps. As is discussed in the following chapter, Yb^{3+}-doped materials have a very simple energy level structure with a small thermal defect, the fraction of pump power locally converted to heat, and a long fluorescence lifetime which makes them ideal for diode-pumped, solid state amplifiers. Furthermore, laser diodes are extremely efficient, with electrical to optical efficiencies exceeding 50%.

Modern NIR laser diodes are commercially available in very high average powers. For example, Figure 1.11 shows a laser diode array that is commercially available from Coherent [65] that emits 4.5 kW average power at 940 nm. This array is a *stack* of 45 bars of 10 emitters each. The package is water-cooled through microchannels allowing very efficient heat removal. Furthermore, this high power is delivered in a very small package. This stack is only about 1 cm wide x 7.5 cm tall x 3 cm deep. This is much smaller than any equivalent power optical source. Due to the

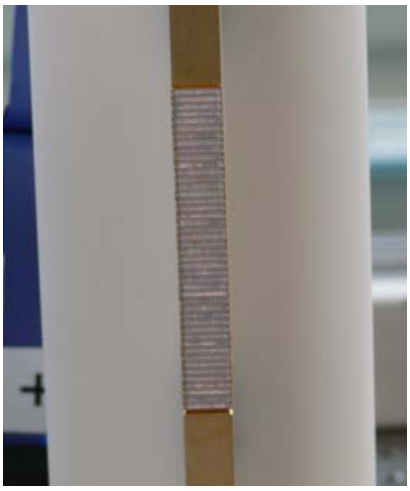

Figure 1.11: Photograph of a 4.5 kW laser diode stack manufactured by Coherent. This stack emits at a wavelength of 940 nm.

asymmetrical geometry of laser diode emitters, the laser diode radiation has a large divergence angle in one direction known as the fast axis, and a moderate divergence on the other axis, the slow axis. The emission from each bar is collimated by a microlens to reduce the divergence of fast axis of the emitters to about 0.5°. The divergence of the slow axis is about 10°. The diode laser output is highly directional which is a major advantage when compared to flashlamps which emit in all directions. This directionality allows longitudinal or end-pumping of solid state lasers, which is not possible with flashlamps. This increases the efficiency and improves mode quality as the pump light can be mode-matched to the seed laser beam. Laser diodes can also be coupled to optical fibers simplifying design and improving pump beam quality. Furthermore, laser diodes do not require high voltage and high current electrical pulses or emit damaging UV light as do flashlamps.

However, there are a few drawbacks to laser diode pumping. Laser diodes are currently low peak power devices when compared with flashlamps or nanosecond lasers. This limits efficient diode-pumped pulsed amplifiers to materials with long upper laser level lifetimes. At very high repetition rates, when the time between pulses approaches the upper level lifetime, this limitation disappears. Another disadvantage of

laser diodes is that they are relatively fragile, and at present are expensive. However, there is a great amount of work being done to increase the power and reduce costs.

1.3.2 Current State of the Art Diode-Pumped CPA Lasers

The development of directly diode-pumped, short pulse lasers is a very active area of current research. A number of groups are developing high energy, high repetition rate diode-pumped CPA systems for a variety of applications including driving of soft x-ray lasers [66, 67] and as pump sources for optical parametric chirped pulse amplifiers (OPCPA) for the production of ultrashort laser pulses [68, 69]. The first demonstration of a diode-pumped CPA system was made in 1997 [70]. In this demonstration, a diode-pumped Yb:YAG regenerative amplifier produced pulses of hundreds of microjoule energy at 1 kHz repetition rate that could be compressed to about 2 ps duration. This laser made use of a *thin disk, active mirror* configuration, in which the laser crystal is very thin, typically 100 μm to 1 mm. In such gain media one face of the crystal is anti-reflection coated while the other face is a high reflector. The mirror surface is soldered to a heat sink. Since the amount of material for the heat to dissipate through is minimal, this is a very efficient cooling geometry. Additionally, the thermal gradient is longitudinal, which is the direction of laser propagation. This further reduces thermal effects such as thermal lensing and depolarization. This and other solids state laser geometries are discussed in more detail in Chapter 2. Following this first demonstration of diode-pumped CPA there has been much effort put toward increasing the pulse energy and average power.

Figure 1.12 summarizes the diode pumped, high energy CPA lasers demonstrated to date. This figure shows the pulse energy and repetition rate of these systems along with the average power and year corresponding to each demonstration. The great interest in the development of these lasers is evident by the large number of publications in the past two years. The first few demonstrations of >1 mJ diode-pumped

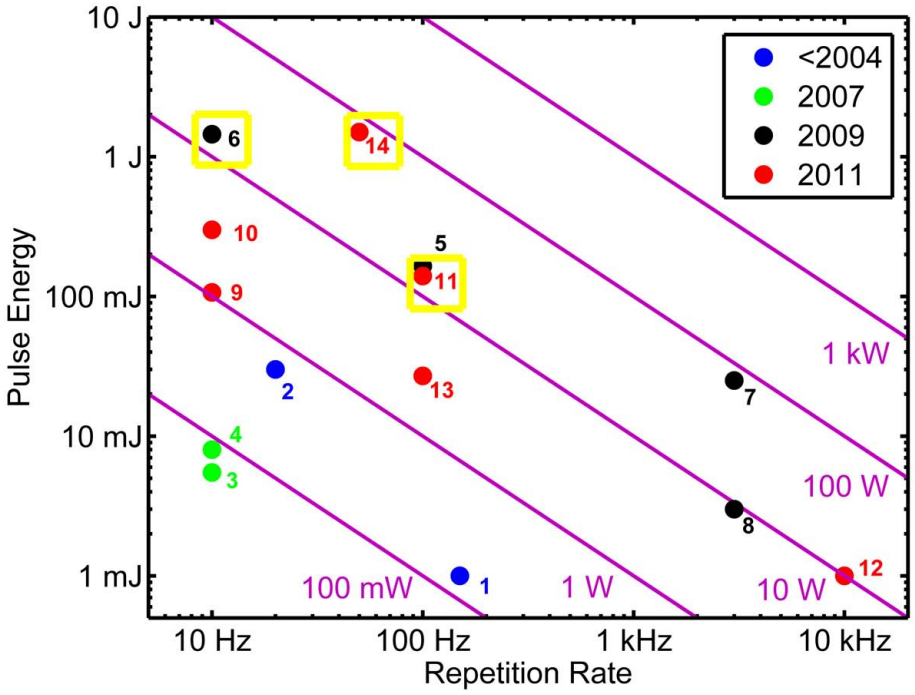

Figure 1.12: Summary of high energy, laser diode pumped CPA systems demonstrated to date. Diode pumped, CPA lasers producing greater than 1 mJ energy at repetition rates greater than 5 Hz are included. Uncompressed pulse energy is plotted on the vertical axis while repetition rate is plotted on the horizontal axis, both are in logarithmic scale. The lines are contours representing average power, and the color of the symbol represents the year of each demonstration. Our work is highlighted with yellow boxes. 1: [71], 2: [72], 3: [73], 4: [74], 5: [66], 6: [67], 7: [75], 8: [76], 9: [77], 10: [68], 11: [78], 12: [79], 13: [80], and 14: this work.

CPA laser systems were made in room temperature Yb:Glass and cryogenically-cooled Yb:YLF, Yb:YAG, and Yb:KYW amplifiers and were limited to less than 1W average power with mJ laser pulses [71, 72, 73, 74]. In 2009, several groups, including this work, demonstrated higher energy and average power systems using Yb:YAG. Tummler, et al. demonstrated a room temperature, thin disk system that could produce 165 mJ pulses at 100 Hz repetition rate [66]. These pulses had bandwidth that could support 2 ps compressed pulse duration. Metzger, et al. demonstrated a room temperature Yb:YAG thin disk laser that produced 25 mJ pulses at 3 kHz repetition rate. The pulses were compressed to 1.6 ps FWHM duration [75]. This work was also

interesting because they observed a region of deterministic chaos in the pulse energy when the time between pulses was near the lifetime of the material. Also in 2009, we demonstrated the first diode-pumped laser to produce more than 1 J of energy in picosecond pulses [67]. This laser system was based on cryogenically-cooled Yb:YAG amplifiers and produced 1.45 J pulses at 10 Hz repetition rate that were compressed to 8.5 ps duration pulses with 1 J energy.

Chapter 2 describes the development of a diode-pumped CPA laser system that produces 5 ps duration pulses with 1 J energy at 50 Hz repetition rate and discusses its performance. Chapter 3 describes the demonstration of a soft x-ray laser driven by a version of this all-diode-pumped laser. Chapter 4 is a summary and discussion while Appendix A describe a computer model of amplified spontaneous emission, which is a limiting effect in the design of high energy amplifiers.

Chapter 2

Development of a Diode Pumped, High Repetition Rate, High Energy Picosecond Laser

2.1 Introduction

The first chapter gave a description of soft x-ray lasers and mentions the motivations for the development of more compact, higher repetition rate and average power chirped pulse amplification (CPA) laser systems. The inefficiency of flashlamp-based lasers limits these systems to low repetition rates. Directly-pumping with laser diodes is much more efficient than flashlamp pumping and allows operation at significantly higher average powers.

This chapter describes the design and performance of a high energy, all diode pumped CPA laser system. This system produces 1.5 J pulses at 50 Hz repetition rate. These pulses were compressed producing 1 J pulses of 5 ps duration. Furthermore, this system is very compact, occupying only one 12' x 5' optical table excluding the pulse compressor. The choice of laser materials is discussed in the next section

followed by an overview of the layout of the system. This is followed by a description of the oscillator and grating stretcher that produce low energy seed pulses. The design of the amplifiers is described next, followed by a presentation of the results obtained and a discussion of the performance of this system.

2.2 Yb Laser Materials

As briefly mentioned in the previous chapter, ytterbium^{3+}-doped materials have several characteristics that make them an excellent solid state laser material for pumping with laser diodes. Even though the Yb laser materials haven been known since the 1960s, they were largely overlooked until the development of high power InGaAs laser diodes. Figure 2.1 shows the energy level digram of Yb-doped materials. The Yb energy level configuration is very simple consisting of only two manifolds each containing several energy levels. As can be seen from this figure, the laser transition is around 1030 nm and can be pumped on several transitions from the ground state at wavelengths between 930nm and 980 nm, where high power laser diode arrays are commercially available. Furthermore, the absorption peaks are relatively broad, when compared to other diode-pumped lasers such as Nd:YAG, which relaxes the pump wavelength accuracy required. At room temperature the main absorption peak of Yb:YAG at 941 nm has a bandwidth of about 18 nm [81], which is about 10 times broader than the 808 nm absorption line of Nd:YAG [63]. This greatly simplifies the temperature control required for pump laser diodes.

In addition, Yb materials have relatively long upper level lifetimes when compared to other laser materials. This is important for high energy amplifiers, as it allows high energy storage when pumping with low peak intensity laser diodes. For example the lifetime of Yb:YAG and Yb:YLF, two common materials, are 1.0 ms and 2.2 ms respectively [82]. This is much longer than the 230 μs lifetime of Nd:YAG or 3.2 μs

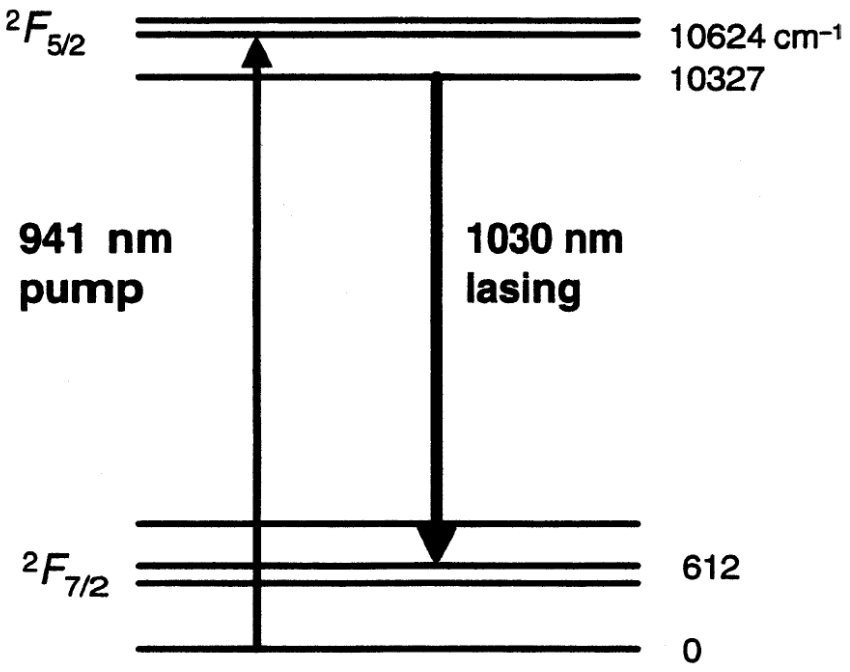

Figure 2.1: Energy level diagram of Yb:YAG. The normal pump and laser transitions are shown. Although Yb:YAG is shown, all Yb-doped laser materials have a similar energy level configuration. From [63]

lifetime of Ti:Al_2O_3 [63]. This long fluorescence lifetime permits the use of long pump pulses from peak power-limited laser diodes and therefore high energy amplifiers are possible with reasonable-sized laser diode arrays.

Additionally, Yb-doped materials have several other features that make them excellent for high power solid state laser amplifiers. Figure 2.1 shows that Yb lasers are typically pumped at a wavelength near 940 nm and lase at a wavelength near 1030 nm. Since the energy of the laser transition is only about 9% smaller than that of the pump transition, only this small fraction of the pump power is locally converted to heat. This thermal defect is much smaller than that of other solid state laser materials such as Ti:Al_2O_3, which has a thermal defect of 34% when pumped at 532 nm. Additionally, the presence of only one excited state manifold eliminates the problems of excited state absorption and up-conversion of other rare earth laser systems [63]. Furthermore, in many laser crystals including YAG and YLF a trivalent Yb ion replaces a trivalent Y ion. Since Yb^{3+} and Y^{3+} ions are nearly the same size

very high doping densities are possible, theoretically up to 100%, with up to 10% being common. This is a much higher dopant concentration than is possible with Nd, which helps Yb lasers overcome their relatively weak absorption cross section.

There are also a few disadvantages of Yb lasers. First, both the stimulated emission cross section and the absorption cross sections are relatively small, about an order of magnitude smaller than Nd:YAG at room temperature. This low stimulated emission cross section complicates the design of pulsed amplifiers as it increases the laser fluence required for efficient energy extraction. The saturation fluence is defined as:

$$J_{\text{sat}} = \frac{h\nu}{\sigma_{\text{e}}\gamma} \tag{2.1}$$

where $h\nu$ is the laser photon energy, σ_{e} is the stimulated emission cross section, and γ is a parameter which is 1 for a four level laser system and 2 for a three level system with no degeneracy [63]. In a pulsed amplifier, the laser fluence must exceed the saturation fluence for high extraction efficiency. At room temperature the peak stimulated emission cross section of Yb:YAG is about 2.1×10^{-20} cm^2 leading to a saturation fluence of about 9.2 $^{J}/_{cm^2}$. This fluence is higher than the damage fluence of most currently available optical coatings for pulse durations typical of CPA lasers. This leads to amplifiers that require many passes through the gain material to achieve efficient energy extraction. Furthermore, while the lower laser level being very close to the ground state lowers the thermal defect, it also has the drawback that a significant fraction of atoms can thermally populate the lower laser level leading to a quasi-three level behavior. This leads to increased pump requirements and to lower efficiency when compared to four level systems such as Ti:Al_2O_3 or Nd lasers. At room temperature, a calculation of the Boltzmann distribution reveals that the thermal population of the lower laser level in Yb:YAG is 5.5%. Without pumping, Yb:YAG absorbs light at 1030 nm, and, at steady state, it must be excited with a pumping density of about 1.7 kW/cm^3/%-doping to achieve transparency. The

advantages of diode-pumping Yb lasers outweigh these drawbacks. Moreover, we will see in the next section that these limitations are reduced when the gain medium is cooled to cryogenic temperature. The following section focuses on Yb:YAG, which is well suited to high average power operation and is the material we chose for our diode-pumped CPA system.

2.2.1 Yb:YAG

Of all available crystal hosts, yttrium aluminum garnet, $Y_3Al_5O_{12}$ or YAG, is one of the most widely used. YAG is cubic, isotropic crystal that is transparent from the near UV to the infrared. It has a relatively high index of refraction of about 1.82 near $\lambda = 1\ \mu$m. YAG is also one of the tougher laser materials available with a tensile strength of 280 MPa. The Nd:YAG laser was one of the first lasers to be demonstrated [83] and is now one of the most highly developed solid state laser material. Because of the more than 40 years experience in manufacturing this material, crystalline YAG can be grown in relatively large sizes with high quality, and is commercially available. YAG is also available in very large sizes in ceramic form. Yb:YAG has a number of properties that make it an ideal material for high power and high energy chirped-pulse-amplifiers, these are summarized in Table 2.1. Additionally, a number of these parameters are improved significantly when Yb:YAG is cooled to cryogenic temperature, as can be seen from this table.

At room temperature, YAG has a thermal conductivity of $\kappa = 10.3\ ^{W}/_{mK}$, which is higher than most laser host materials including YLF or glass [84]. The thermal conductivity improves nearly an order of magnitude, to about 90 $^{W}/_{mK}$, when cooled to the boiling temperature of liquid nitrogen (77 K). This is very advantageous for high average power lasers, as all repetition rate-limiting thermal characteristics, such as peak temperature, thermal lens power, and degree of thermal depolarization are inversely proportional to the thermal conductivity of the materials. Additionally, the

thermal-optic coefficient, which is the derivative of the refractive index with respect to temperature decreases by about a factor of 8. These two terms are the physical parameters that determine the primary thermal lensing behavior of a laser material. For example, the temperature profile of uniformly pumped cylindrical rod of radius r_0 and length L, thermal conductivity κ, thermal-optic coefficient dn/dt, and thermal power density ρ can be shown to be parabolic and is:

$$T(r) = T(r_0) + \frac{\rho}{4\kappa}({r_0}^2 - r^2) \tag{2.2}$$

This temperature profile leads a refractive index profile that is parabolic and is highest in the center of the rod for most materials. From [63], the focal length of this profile is:

$$f = \frac{2\kappa}{\rho L(dn/dt)} \tag{2.3}$$

Another component of thermal lensing arises when the thermal gradient is sufficiently strong to cause a strong enough stress within the material to significantly distort the surfaces of the laser crystal [63]. This component is typically weaker than the refractive index gradient component discussed here. This effect scales with the thermal expansion coefficient, α, which for Yb:YAG is also improved significantly upon cool-

Parameter	300 K	77 K
Thermal conductivity (W/mK)	10	90
Thermo-optic coefficient, dn/dT (10^{-6}/K)	7.8	0.9*
Expansion coefficient, α (10^{-6}/K)	6.14	1.95*
Peak stimulated emission cross section (10^{-20}cm^2)	2.1	11
Emission Bandwidth (FWHM nm)	9	1.5
Saturation fluence (J/cm^2)	9.2	1.7

Table 2.1: Summary of spectroscopic and thermal properties of Yb:YAG at room temperature and cryogenic temperature. From [84, 85].

ing to cryogenic temperature. In typical solid state amplifiers, the thermal lens must be longer than about 10 meters in order to properly compensate for the distortion with lens combinations. With aggressive compensation or a phase conjugation setup, more powerful thermal lenses can be tolerated. Of currently available solid state laser host materials only sapphire has superior thermal characteristics than YAG. Yb:YAG is one of the best materials available for high average power diode pumped lasers.

In addition to its excellent thermal properties, the spectroscopic characteristics of Yb:YAG make it an ideal material for high energy, picosecond laser amplifiers. As Yb:YAG is predominately thermally broadened, the spectral bandwidth and magnitude of the absorption and emission cross sections are very dependant on temperature. The absorption cross section as a function of wavelength of Yb:YAG at ambient and cryogenic temperatures is shown in Figure 2.2. As can be seen from this figure the broad absorption peak near 940 nm is ideal for pumping with high power InGaAs laser diodes. This transition remains fairly broad when cooled to liquid nitrogen temperature which relaxes the wavelength specification and temperature control requirements of the pump laser. At liquid nitrogen boiling temperature the absorption cross section peaks at 941nm at a value of about 1.6 $\times 10^{-20}$ cm^2, which allows absorption of about 98% of the pump power in a length of 1 cm with 2% atomic doping density when pumped with a narrow source [81]. When pumped with a 5 nm FWHM spectral width laser diode, as is typical for high power laser diode arrays, pump absorption still remains high, absorbing about 90% in a length of 1 cm with 2% doping [81].

Figure 2.3 shows the pertinent emission properties of Yb:YAG at both room and cryogenic temperature. As can be seen from Figure 2.3 (a) the fluorescence bandwidth narrows and increases significantly when Yb:YAG is cooled to cryogenic temperature. The peak emission occurs near 1030 nm at both temperatures. The stimulated emission cross section increases from about 2.1 $\times 10^{-20}$ cm^2 at room temperature to about 1.1 $\times 10^{-19}$ cm^2 at cryogenic temperature. This reduces the saturation fluence from

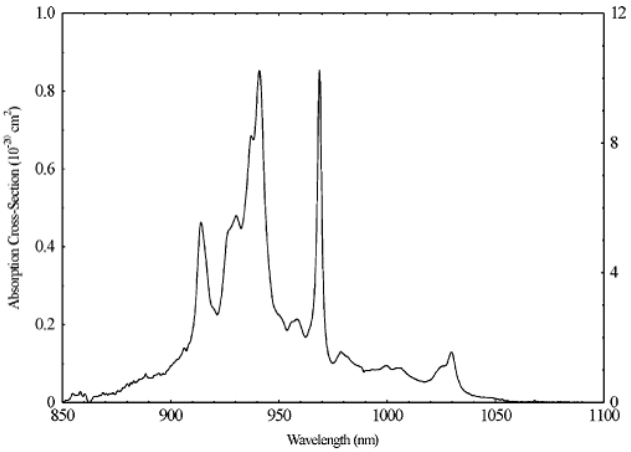

(a)

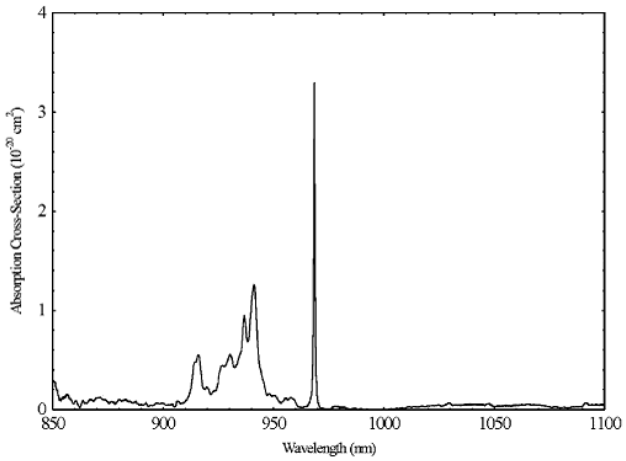

(b)

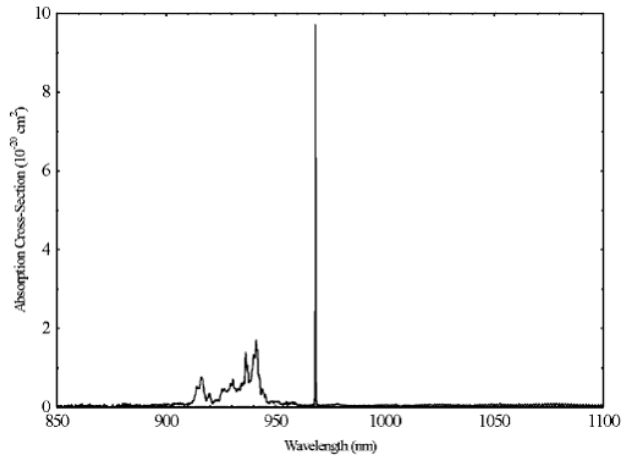

(c)

Figure 2.2: Absorption cross section of Yb:YAG as a function of wavelength for temperatures of (a) 300 K, (b) 175 K, and (c) 75 K. Note the change in scale for each plot. From [81]

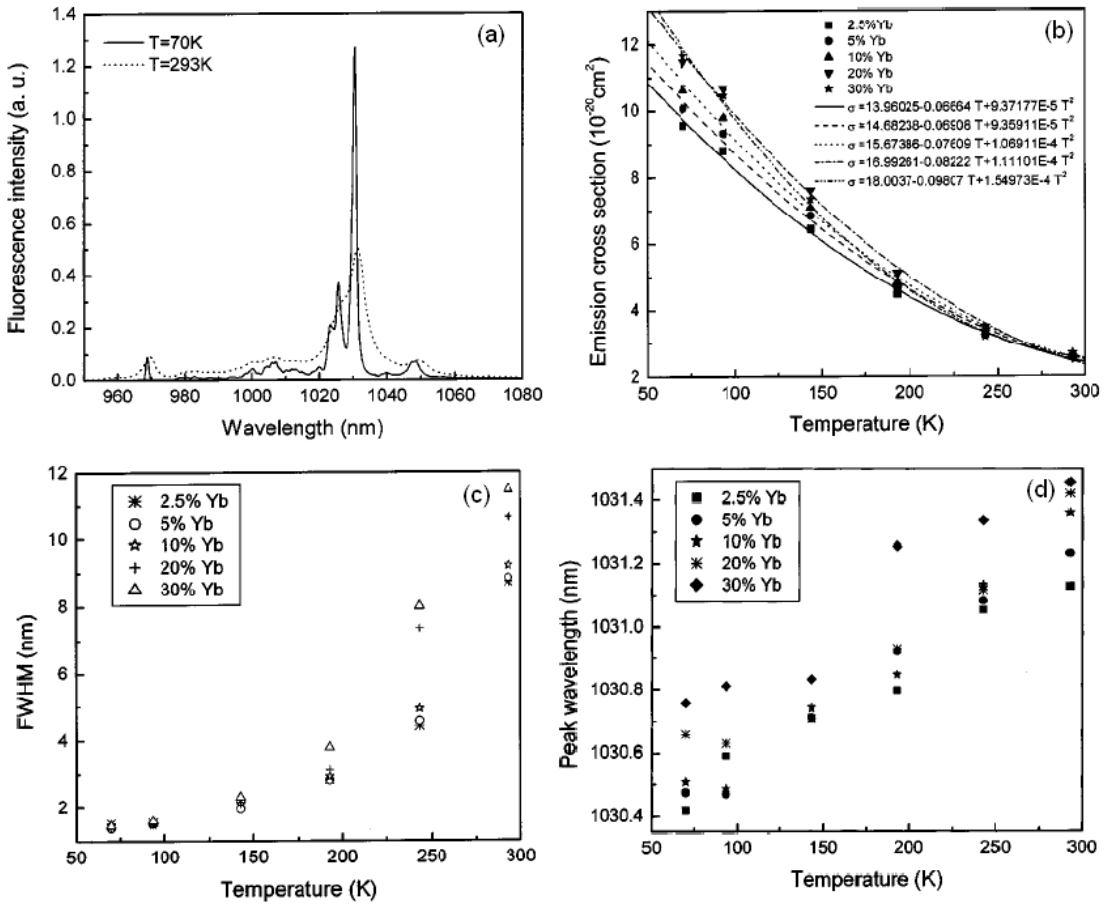

Figure 2.3: Yb:YAG emission characteristics. (a) Fluoresence spectra at room and cryogenic temperature. (b) Peak emission cross section as a function of temperature for different Yb doping densities. (c) Emission bandwidth as a function of temperature for different Yb doping densities. (d) Wavelength of peak fluorescence intensity as a function of temperature for different Yb doping densities. From [86].

about 9 $^{J}/_{cm^2}$ to less than 2 $^{J}/_{cm^2}$. This is very important, as previously mentioned, because amplifiers must operate near the saturation fluence to achieve efficient energy extraction in a reasonable number of passes through the gain material. Laser fluences below 2 $^{J}/_{cm^2}$ for stretched pulse durations typical of CPA systems usually do not cause optical damage on currently available anti-reflection and high reflector coatings. Additionally, operation at lower fluences and with a limited number of passes through the gain material is desirable to reduce nonlinear effects that can disrupt temporal compressibility and reduce beam quality. The degree of nonlinear effects is normally evaluated with a parameter know as the *B-integral* that is given by:

$$B = \frac{2\pi}{\lambda} \int_0^L n_2 I(z) dz, \tag{2.4}$$

where n_2 is the Kerr nonlinear index of refraction of the material of length L in which the beam is propagating, and I(z) is the peak laser intensity. As the product of I and n_2 is the change in refractive index due to the Kerr effect it can be seen the the B-integral is the total accumulated phase shift between the most intense and least intense portions of the beam. For B-integral values of less than 1, nonlinear effects are generally not noticeable. However for values greater than 3 there is a risk that self-focusing can occur. At even higher values, filamentation can occur, in which different sections of the beam locally focus causing *hot spots* which can cause optical damage.

Accompanying this increase of the stimulated emission cross section is a narrowing of the bandwidth as can be seen from Figure 2.3 (c). When cooled to 77 K, the emission bandwidth narrows from around 9 nm to about 1.5 nm FWHM. This narrow bandwidth combined with the sharply peaked spectral shape limits the shortest duration pulses that can be achieved. In fact, for CPA systems with only cryogenic Yb:YAG amplifiers, no pulse duration less than 8 ps FWHM has been reported

[67, 74, 87]. In contrast, laser pulses from CPA systems with room temperature Yb:YAG amplifiers typically can be compressed to 2 ps duration [66, 75] with sub-ps pulse durations possible with aggressive spectral shaping [68]. Additionally, the peak emission wavelength is dependant upon temperature and Yb density as can be seen in Figure 2.3. For laser systems combining Yb:YAG amplifiers operating at different temperatures or with very different doping, attention must be paid to matching the center wavelength.

Furthermore, as mentioned above, at room temperature Yb:YAG is a quasi-3 level laser system, with about 5% of the Yb ions occupying the lower laser level. At cryogenic temperature, the fraction of ions in the lower level is dramatically reduced to a negligible 10^{-5}, allowing the it to function as a four level laser system. This reduces the pump power required and increases the achievable efficiency.

For these reasons, cryogenically-cooled Yb:YAG is an excellent laser material for amplifiers producing high energy, picosecond laser pulses at high repetition rates in an all diode pumped system. The design and performance of the 1.5 J, 50 Hz, diode-pumped CPA system is described in the following sections.

2.3 Laser System Overview

Figure 2.4 shows a block diagram of the laser system. As can be seen from this figure, the system makes use of a diode-pumped mode-locked oscillator that produces short, low energy pulses that are stretched to several hundred picosecond duration by a grating stretcher to produce the seed pulses for the amplifiers. This system combines room temperature and cryogenic Yb:YAG amplifiers to exploit the relatively broad bandwidth of the material at room temperature while taking advantage of the high gain and excellent thermal properties of cryogenically-cooled Yb:YAG. The stretched seed is amplified in three stages of amplification: a room temperature regenerative pre-

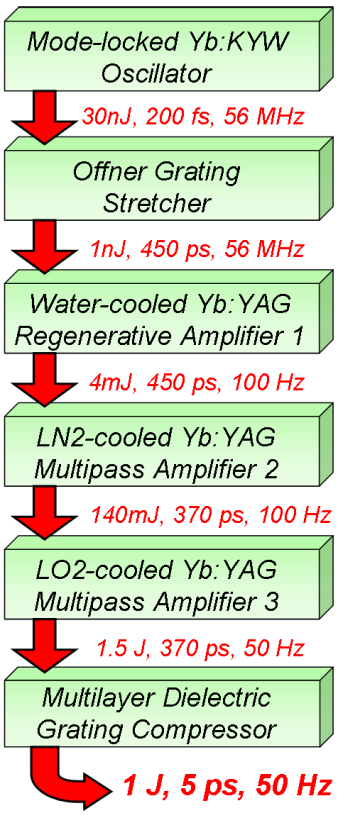

Figure 2.4: Block diagram of the compact diode pumped CPA laser system.

amplifier followed by two stages of multipass cryogenic Yb:YAG amplifiers. Following amplification, the pulses are compressed in vacuum by a dielectric grating compressor. The entire system is very compact with the oscillator, stretcher and all amplifiers occupying one 12' x 5' optical table, with the compressor chamber on an adjacent table. The following sections describe each stage.

2.4 Diode-Pumped Mode-locked Laser Oscillator

The CPA laser makes use of a laser diode-pumped mode-locked laser oscillator schematically illustrated in Figure 2.5. The laser crystal in this oscillator is ytterbium-doped potassium yttrium tungstate (Yb:KYW). Yb:KYW is an attractive material for diode-pumped mode-locked oscillators because of its strong absorption at 981nm, its emission bandwidth is several times larger than Yb:YAG, its low quantum defect

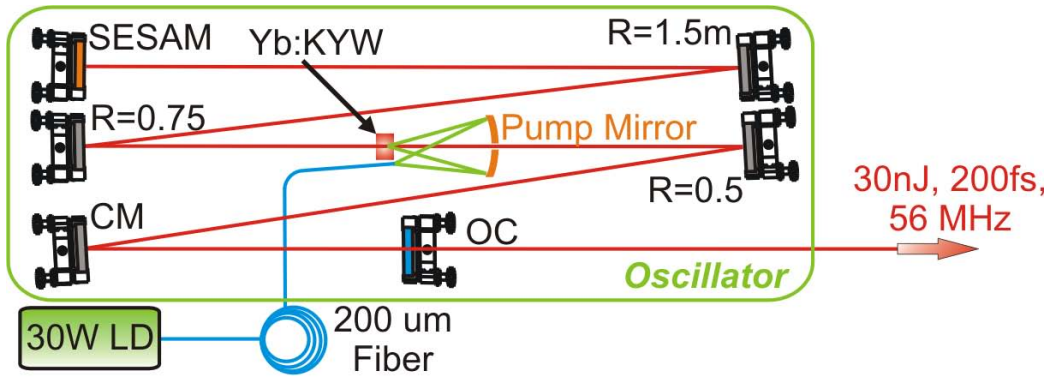

Figure 2.5: Schematic diagram of the diode pumped, modelocked Yb:KYW oscillator. CM: -2000 fs^2 GDD chirped mirror, OC, 6% output coupler, SESAM: semiconductor saturable absorber mirror, LD: 30 Watt, $\lambda = 980$ nm, laser diode coupled into a 200 μm optical fiber.

of only 4%, and a relatively high stimulated emission cross section of about 3×10^{-20} cm^2 [88, 89]. These advantages have led to the development of a number of high power laser oscillators producing femtosecond pulses at high average powers [88, 89]. In our setup, a 5mm x 5mm x 3mm thick antireflection (AR) coated 5%-at Yb:KYW crystal is mounted on to a water-cooled copper heat sink. This crystal is pumped by a 30 W, 981 nm, laser diode coupled into a 200 μm optical fiber. As shown in Figure 2.5, the light exiting the fiber is 1:1 imaged onto the Yb:KYW crystal by a 50.8 mm diameter, 101.6 mm radius concave mirror forming a uniform 200 μm spot. The pump mirror has a small hole drilled through it to allow the laser cavity beam to pass through. The laser cavity was designed to produce a mode-matched focal spot on the crystal with a large waist of several millimeters on the output coupler and a tunable focal spot size on the opposite end mirror by adjusting the cavity length. The oscillator is passively mode-locked by a saturable absorber semiconductor mirror (SESAM) [90]. The SESAM has a saturable loss of 2%, which is sufficient to maintain stable continuous mode locking over output powers of 1-2W. The output coupler consists of a home-made multilayer dielectric reflector coating with 6% transmission deposited on a window substrate that has an AR coating on the opposite face. The output coupler substrate is slightly wedged to eliminate small reflections from the AR

face disrupting stable mode locking.

Dispersion compensation in the oscillator is accomplished by a single chirped mirror made in house. This mirror was designed in a similar manner to that in [91]. The mirror is composed of 70 alternating layers of Ta_2O_3 and SiO_2 deposited through ion beam sputtering (IBS). It was designed to have a group delay dispersion (GDD) of -2000 fs^2 over a range of about 20 nm centered near the lasing wavelngth of 1030 nm. The calculated GDD is shown in Figure 2.6. This value of GDD was experimentally determined by inserting a prism pair into the cavity without the chirped mirror and finding the prism separation and insertion distance that resulted in the broadest bandwidth and most stable mode locking. The coating was measured to have a reflectivity greater than 99.9% over this entire wavelength range. Dispersion compensation through dispersive mirrors is advantageous because of its simpler alignment. It avoids the spatially dispersed beam that is obtained with a SESAM mode locked oscillator

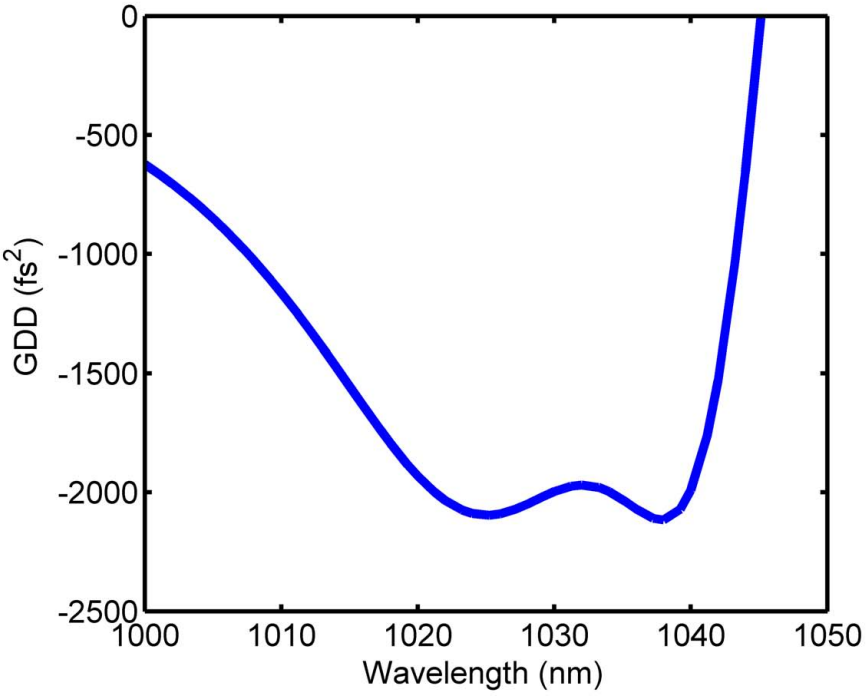

Figure 2.6: Designed group delay dispersion of the chirped mirror used for dispersion compensation in the mode-locked laser oscillator.

with a prism pair.

When pumped with 23 W of pump power the oscillator achieves stable, single pulse mode-locking with an average output power of 1.8 W. The repetition rate determined by the cavity length is 56 MHz, which results in an energy per pulse of 32 nJ. Higher pump powers were observed to result in multiple pulses and a CW beam component. However higher output power could probably be achieved by increasing the pump power in combination with an increased transmission output coupler. The spectrum of the output beam is shown in Figure 2.7 (a). This spectrum was obtained using a fiber-coupled spectrometer with ≈1 nm resolution. The center wavelength was about 1035 nm, with a bandwidth of 6.9 nm FWHM. The spectral intensity of the oscillator at 1030nm is about 20% of the peak, which is adequate for seeding the Yb:YAG amplifiers in the system. The duration of the pulses was measured with a home made second harmonic autocorrelator, the result of this measurement is shown in Figure 2.7 (b). Assuming a sech^2 pulse shape, the pulses had a duration of 190 fs FWHM. This pulse duration is nearly transform limited with a time-bandwidth product of 0.36.

The oscillator is very compact, occupying an area of 1 x 0.25 m^2, and it is also quite stable, only requiring realignment after several months of operation. The beam exiting the oscillator is stretched in a grating stretcher before seeding the chain of amplifiers. The grating pulse stretcher is discussed in the next section.

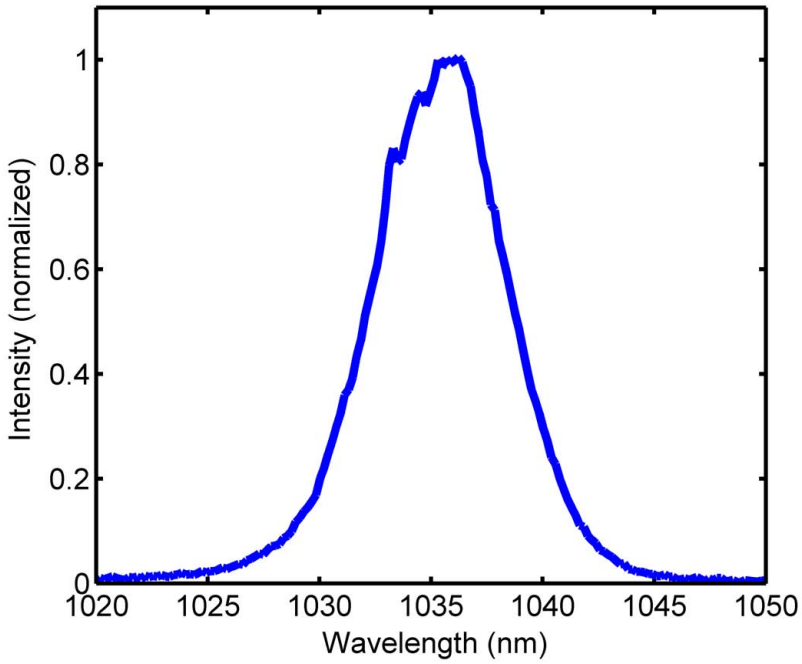

(a)

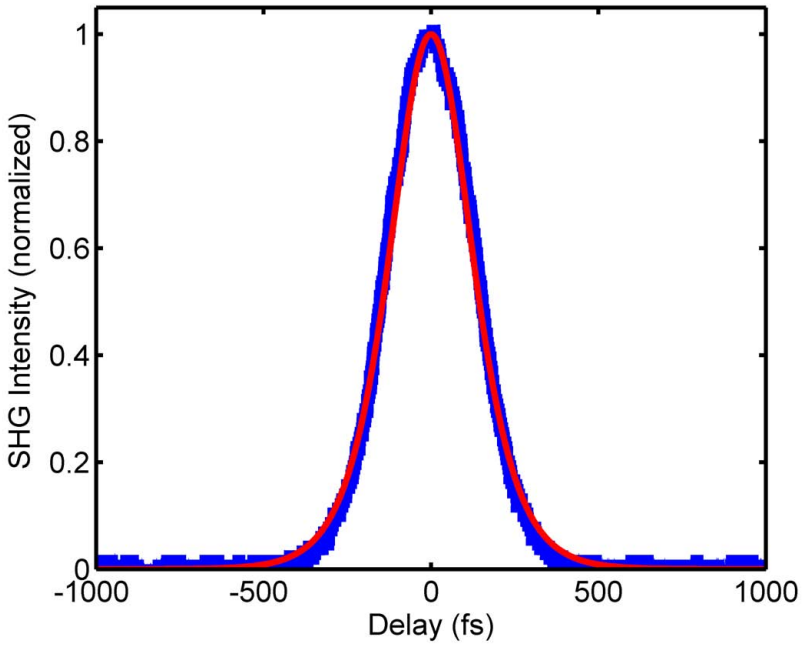

(b)

Figure 2.7: (a) Spectrum of beam exiting the modelocked oscillator. The pulses have a bandwidth of 6.9 nm FWHM. (b). Second order autocorrelation of pulses exiting the autocorrelator. The thin red line is a sech^2 fit of the data. The pulses have a duration of 190 fs FWHM assuming a sech^2 pulse shape.

2.5 Grating Pulse Stretcher

A diffraction grating pulse stretcher is used to temporally stretch the pulses from the oscillator to a duration of several hundred picoseconds prior to amplification. Because of the relatively narrow bandwidth of the amplified laser pulses as compared to conventional flashlamp pumped CPA laser such as Ti:AL_2O_3 a very large stretch factor, $^{\Delta T}/_{\Delta\lambda}$ is required. In order to accomplish this in a compact footprint a reflective, folded grating stretcher with an Offner-type telescope is used as shown in Figure 2.8. Additionally, the entire stretcher is double-passed with respect to the standard configuration, doubling the total stretch obtained. By applying the grating equation and geometry considerations, the variation of the group delay with wavelength for a parallel grating pair is [61]:

$$\Delta\tau = \frac{L(\lambda/d)\Delta\lambda}{cd(1-(\lambda/d - sin\gamma)^2)} \tag{2.5}$$

where L is the perpendicular distance between the gratings, λ is the center wavelength, d is the groove spacing of the grating, c is the speed of light, and γ is the angle of incidence on the first grating. As mentioned in the previous chapter, the inclusion of a telescope between the gratings can result in an effectively negative optical path

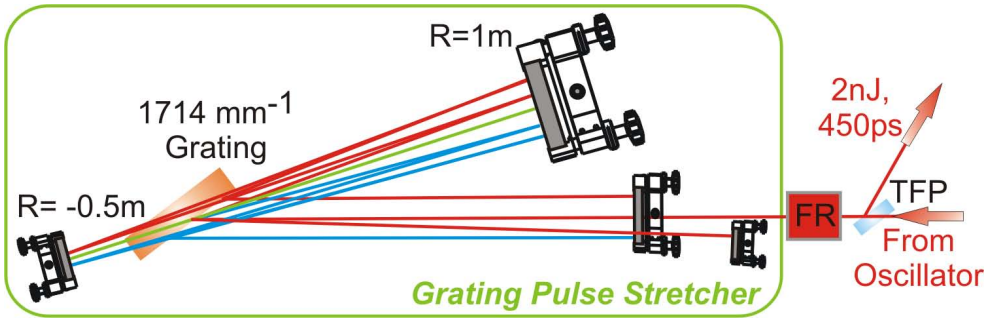

Figure 2.8: Schematic diagram of the grating pulse stretcher. An Offner configuration is used and the entire stretcher is double-passed by way of a Faraday rotator (FR), waveplate, and thin film polarizer(TFP). The beam is diffracted by the 1714 lines/mm holographic diffraction grating eight times.

separation resulting in positive dispersion [62]. In this folded stretcher one grating constitutes the grating pair, and the 1m radius concave mirror and -0.5 m convex mirror form an Offner triplet telescope [92] with an effective optical distance of -2.4 m for one pass through the stretcher. This large path difference is made possible by the Offner telescope, which allows for a longer negative effective distance while at the same time cancelling out spherical aberration [92]. When double-passed the stretcher has effective distance is -4.8 m. With a groove spacing of 1714 lines/mm, angle of incidence, $\gamma = 52.5°$, center wavelength, $\lambda = 1030$ nm, and $\Delta\lambda = 0.5$ nm, which is the bandwidth remaining after gain narrowing in the first amplifier, the stretched pulse duration is 440 ps. This value was confirmed by the deconvoluting a fast photodiode measurement of the output pulse from the impulse response of the photodiode. In this configuration, the stretcher passes about 1.5 nm bandwidth, which is sufficient for seeding the chain of amplifiers.

2.6 Active Mirror Amplifiers

As mentioned above, a chain of three amplifiers is used to produce pulses with energy up to a 1.5 J at high repetition rates. All of the amplifiers in this system use the "active mirror" geometry which allows for efficient heat removal at high average powers [93]. In this configuration, a usually thin laser crystal has a high reflector (HR) on one face and an anitireflection (AR) coating on the opposite face for both the pump and laser wavelengths. The HR face is in thermal contact with a heat sink or cooling fluid, as shown in Figure 2.9 (a). Because the heat is dissipated through a short distance, compared to conventional cylindrical laser rods, the overall increase in temperature is minimized. Furthermore, as can be seen in the figure, the thermal gradient is longitudinal in the laser propagation direction. This thermal gradient profile nearly eliminates thermal lensing, which is in contrast to cylindrical cooling which results in

radial parabolic temperature gradient [63]. This is illustrated by Figure 2.9 (b) which shows a finite element simulation of the temperature profile for an edge cooled laser rod and a face-cooled active mirror laser disk. Both are assumed to be equivalently-pumped with 4kW, 1.5ms, pump pulses at $\lambda = 940$nm at 100 Hz repetition rate, and only the fraction of pump power given by the thermal defect (1-940/1030) is assumed to contribute to heating. Both are Yb:YAG crystals at cryogenic temperature. This simulation solves Fourier's law of heat conduction, which is

$$\vec{q} = -k \quad T \tag{2.6}$$

where $\vec{q}$ is the local heat flux, k is the thermal conductivity which in the most general case is dependant on temperature, and T is the temperature gradient. For each

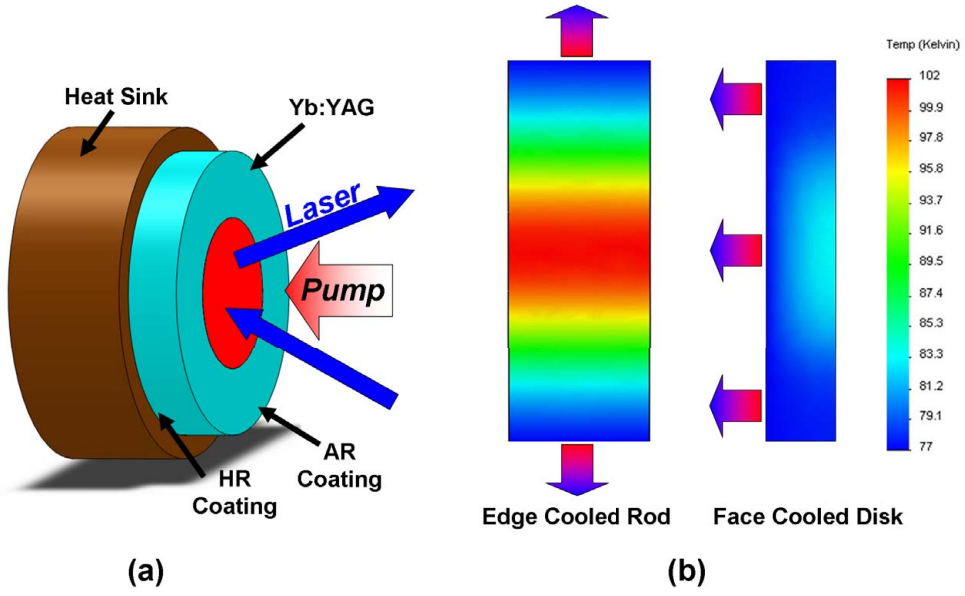

Figure 2.9: (a) Schematic of the active mirror laser geometry. (b) Comparison of edge cooling and active mirror face cooling techniques. Each map is the simulated thermal profile of a Yb:YAG crystal at liquid nitrogen temperature when pumped with a 4 kW peak power, 1.5 ms duration $\lambda = 940$ nm pulses at 100 Hz repetition rate. The active mirror crystal has a maximum temperature difference of 6° C, while the edge-cooled rod has a temperature difference of about 25 ° C. The thermal gradient is radial in the case of the edge-cooled rod, while it is mostly longitudinal for the active mirror geometry.

geometry the appropriate cooling surface is held at a constant temperature and the thermal power is uniformly distributed within a 16mm diameter cylinder in the center of the crystal. As can be seen from this figure the face-cooled active mirror is a much more thermally efficient geometry with a maximum temperature difference of only about 6° C, where the edge-cooled rod has a temperature difference of 25° C. Additionally, the temperature gradient of the active mirror is mostly longitudinal which does not contribute to thermal lensing.

Active mirror lasers have become nearly synonymous with "thin disk" lasers in which the the laser crystal is typically 100-200 μm thick. In this geometry, the heat removal distance is very short allowing for very high power operation. Additionally, because the heat removal is proportional to the beam size, this technique is scalable to very high average power simply by increasing the beam size on the disk. This method has been used very successfully to make CW lasers with up to 5.3kW average power from a single laser disk, up to 8 kW with multiple disks in one laser cavity [94] and mode-locked oscillators with up to 140 W average power [95]. While the thin disk approach is excellent for CW and low energy, high repetition rate pulsed laser amplifiers, there are severe limitations in scaling this technique to high energy amplifiers. Because of the low aspect ratio of the gain region for the beam sizes required for high energy operation, the transverse gain becomes much higher than the longitudinal gain. This can lead to large amplified spontaneous emission (ASE) which depletes the stored energy. If care is not take to eliminate reflections on the edges of the laser crystal, the feedback can further exacerbate the situation leading to parasitic laser oscillations. Figure 2.10 shows the simulated stored energy of a Joule-level, cryogenic Yb:YAG amplifier as a function of crystal thickness in the presence of ASE. The details of this model are discussed in Appendix A. As can be seen from this figure, the thin disk geometry limits the stored energy for large area, high energy amplifiers.

We have chosen an approach that provides a compromise between the highly efficient heat removal of the thin disk, active mirror laser geometry while still allowing for high energy storage in the amplifiers. Figure 2.10 shows that at a thickness of several mm efficient energy storage is still possible. Because of the high thermal conductivity of Yb:YAG at cryogenic temperature combined with the face-cooling of the active mirror geometry, high average power operation is possible, as can be seen from Figure 2.9. This "thick disk" approach with cryogenic Yb:YAG combines the thermal advantages of the active mirror with the high energy storage possible with thicker gain media.

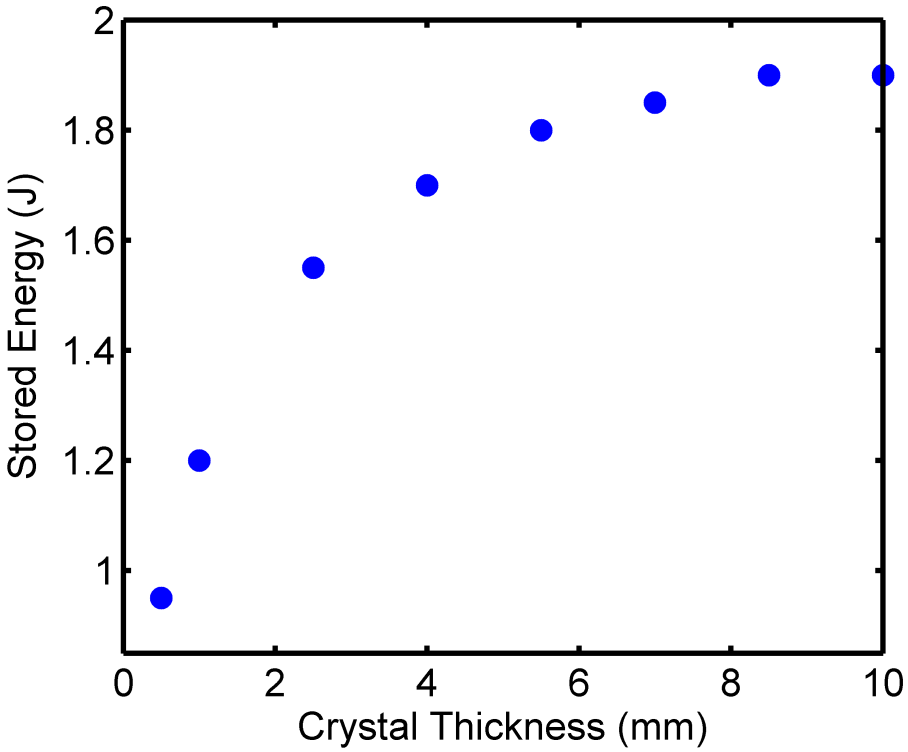

Figure 2.10: Simulated stored energy as a function of crystal thickness for a cryogenically-cooled Yb:YAG crystal in the presence of ASE. The model assumes 90% absorption of 2ms, 3kW, 940nm pump pulses in a 16mm diameter spot size.

2.7 Regenerative Preamplifer

The first stage of amplification is the room temperature Yb:YAG regenerative amplifier shown schematically in Figure 2.11. With a gain of 10^6 - 10^7 this is the highest gain amplifier in the system, capable of amplifying the stretched pulses from the stretcher to the mJ level. The optical cavity of the amplifier is designed to have a mode size of about 700 μm FWHM at the location of the laser crystal. The mode size increases to $\approx$2 mm on the opposite end of the cavity to reduce the laser intensity on the Pockels cell, quarter waveplate and thin film polarizer that are used to couple the seed pulses from the stretcher into the amplifier and to eject amplified pulses out of the amplifier. The laser crystal is a 1mm thick x 10mm diameter 10%-at Yb:YAG used in the active mirror configuration. The crystal is cut with a slight wedge between the faces of $\approx$1° to eliminate unwanted reflections in the cavity. The high reflecting face of the crystal is soldered to a water-cooled copper heatsink and the temperature is held at 20° C. The cavity is designed to make two double passes through the active region of the crystal per cavity single pass resulting in an increased gain to loss ratio. This also reduces the effects of spatial hole burning which are unavoidable in thin

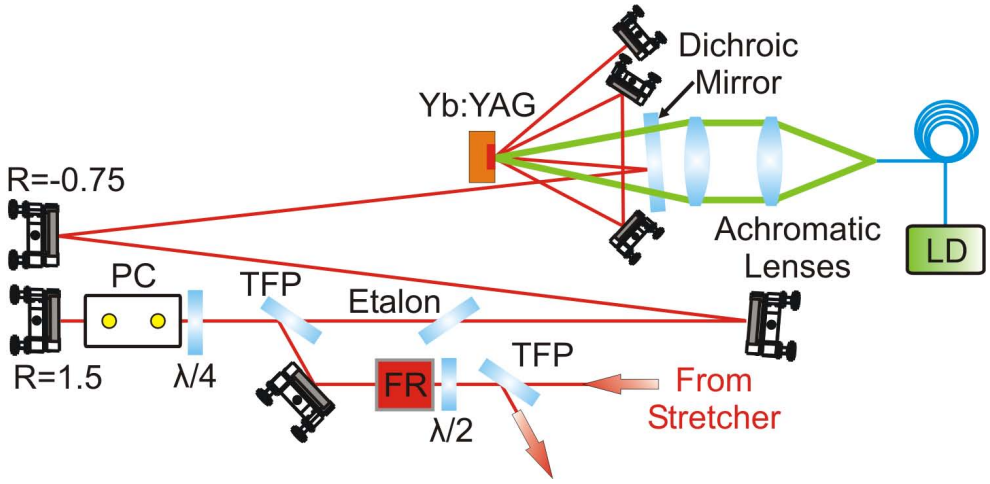

Figure 2.11: Schematic diagram of the first stage regenerative amplifier. FR: Faraday rotator, $\lambda/2$: half waveplate, $\lambda/4$: quarter waveplate, TFP: thin film polarizer, PC: Pockels Cell, LD: fiber-coupled laser diode.

disk, active mirror setups [96]. The Yb:YAG crystal is pumped by a 90 W average power λ = 940nm laser diode array coupled into a 600 um optical fiber. The laser diode is pulsed to produce square shaped temporal pulses of variable duration and repetition rate. Pump light emerging from the fiber is imaged through a dichroic mirror onto the crystal by a pair f = 100mm achromatic lenses, producing a relatively uniform 600 um spot. The pump optics couple the light into the crystal with an efficiency of 65%. A slight adjustment of the wavelength is necessary to match the peak gain of the cryogenically-cooled second stage amplifier. For this reason a home-made thin film etalon is inserted into the cavity that can be used to tune the center wavelength over a few nanometers with a tolerable loss of energy. A Faraday rotator and thin film polarizer are used to inject seed pulses from the stretcher and extract the amplified pulses which are collinear. The amplifier is compact, occupying

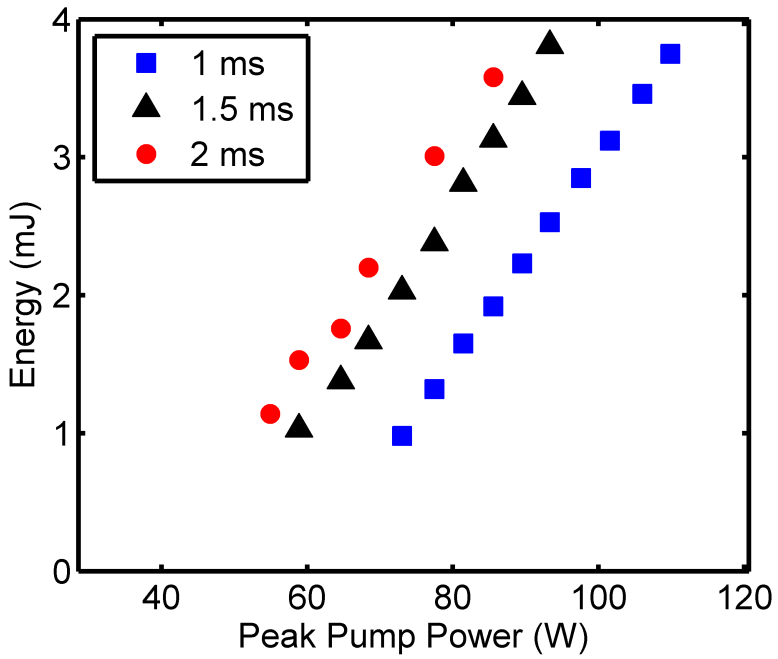

Figure 2.12: Output pulse energy of the regenerative amplifier as a function of peak pump power at 100 Hz repetition rate. The three data sets are for pump pulsewidths of 1ms, 1.5ms, and 2ms respectively. The number of cavity roundtrips before the pulse was ejected was optimized for each data point.

1 x 0.3 meter^2 of table space.

This amplifier produces pulses of up to 4 mJ energy at 100 Hz repetition rate, and energies up to 1.5 mJ at 300 Hz repetition rate. Figure 2.12 shows the pulse energy obtained at 100 Hz repetition rate as a function of peak pump power incident on the crystal. Results for pump pulse widths of 1 ms, 1.5 ms, and 2 ms are shown. The output pulse energy was limited to less than 4 mJ to avoid damage observed on the AR coated face of the crystal above this value. For each pump power, the Pockels cell timing was adjusted to optimize the number of cavity roundtrips allowed before the laser pulse was ejected from the amplifier. At the highest energies, the seed pulse makes 16 roundtrips through the amplifier. As expected, shorter pump pulse durations result in more efficient amplification, with 1 ms pulses having an optical to optical efficiency about 50% higher than that obtained with 2 ms duration pump

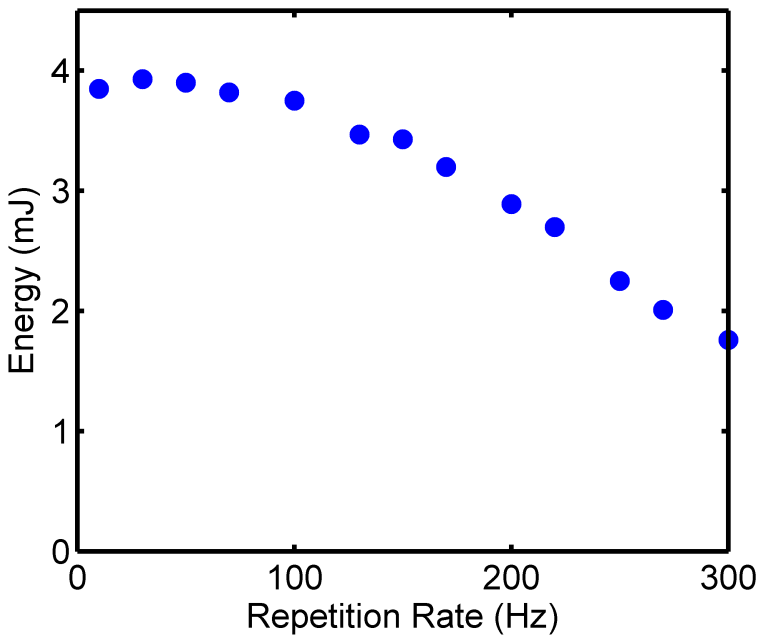

Figure 2.13: Pulse energy obtained from the room temperature regenerative amplifier as a function repetition rate for 1 ms duration 110 Watt pump pulses. The number of cavity roundtrips before the pulse was ejected from the cavity was optimized for each data point.

pulses. The energy output was very stable with a shot to shot standard deviation of 27 μJ (0.7%) when operated at the highest energy. The output pulse energy dependence on repetition rate is shown in Figure 2.13. With 1ms duration 110 W pump pulses, an energy of about 4mJ is obtained at repetition rates up to about 100Hz. However, under these pump conditions, the pulse energy deteriorates almost linearly with repetition rate after 100 Hz, resulting in an energy of 1.7 mJ at 300 Hz. This decay with increasing repetition rate is likely due to an imperfect thermal contact between the crystal and heat sink.

Figure 2.14(a) shows the spectrum of amplified pulses exiting the 100 Hz room temperature regenerative amplifier with the etalon tuned to match the measure peak gain wavelength of the cryogenic second stage amplifier described in the following section. Under these conditions, the pulses have spectral bandwidth of 0.55 nm FWHM and a measured temporal duration of about 440 ps FWHM prior to compression. The pulses were compressed by a pair of dielectric gratings to a duration of 3.6 ps FWHM assuming a sech^2 pulse shape, as illustrated by the second harmonic generation (SHG)

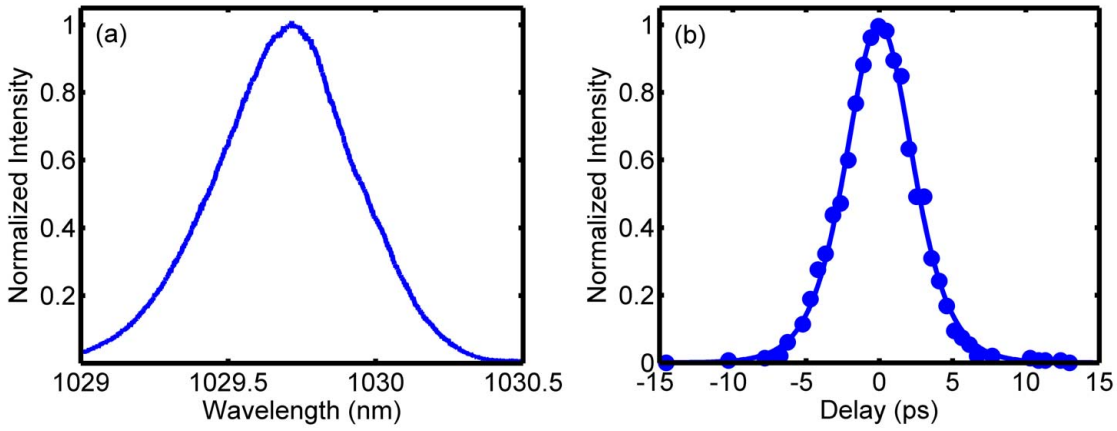

Figure 2.14: (a) Spectrum of 3.6 mJ pulses exiting the room temperature regenerative amplifier at 100 Hz repetition rate with the etalon tuned to match the cryogenic peak gain wavelength. These pulses have a bandwidth of 0.55 nm FWHM and were compressed to 3.5 ps FWHM duration (sech^2 fit). (b) Second harmonic autocorrelation of these pulses after compression. The solid curve is a sech^2 fit of the data.

autocorrelation shown in Figure 2.14(b). This grating pulse compressor is described in more detail later in this chapter.

2.8 Cryogenic Multipass Amplifier

Figure 2.15 shows a schematic of a 4-pass power amplifier based on liquid nitrogen cooled Yb:YAG. A 4.5mm thick 2%-at Yb:YAG crystal used in the active mirror configuration is soldered to a liquid nitrogen-filled copper heat sink. All edges of the square profile crystal were optically bonded to a Cr^{4+}:YAG cladding to prevent parasitic lasing. Cr:YAG is index matched to Yb:YAG and has high absorption at the laser wavelength preventing any significant feedback of spontaneous emission. Furthermore, this "thick disk" geometry combined with the high thermal conductivity at cryogenic temperature allows for excellent thermal behavior while limiting the transverse gain. The crystal assembly is mounted in vacuum onto the bottom of a

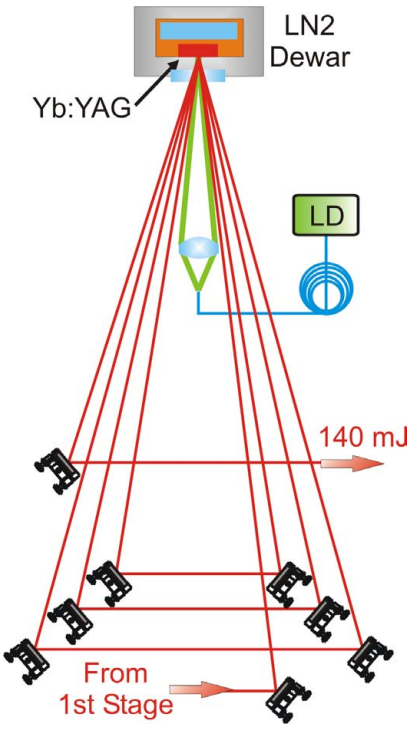

Figure 2.15: Schematic of the second stage cryogenic multipass amplifier.

home-made liquid nitrogen Dewar with capacity of about 3 liters which is sufficient for uninterrupted operation for several hours. The crystal is pumped through a dielectric multilayer coated window by a 500 W fiber-coupled laser diode. The pump light exiting the 600 μm fiber is imaged into a 4mm spot on the crystal by a single 25.4mm diameter, 35mm focal length achromatic lens. Millijoule laser pulses from the room temperature regenerative amplifier described above pass through a pair of crossed calcite polarizers with a Pockels cell between to isolate the two amplification stages and remove small pre-pulses that leak out of the regenerative amplifier. Following this isolation the laser pulses make 4 passes through the laser crystal.

Figure 2.16(a) shows that the small signal single pass gain at 100 Hz repetition rate reaches a value of 4.5 peak pump power of 400 W. Figure 2.16(b) shows the output pulse energy obtained at this repetition rate as a function of peak pump power for pump pulse durations of 0.7 ms, 1.0 ms, and 1.5 ms. In this measurement the seed pulses from the first amplification stage had an energy of 2.4 mJ after the isolation

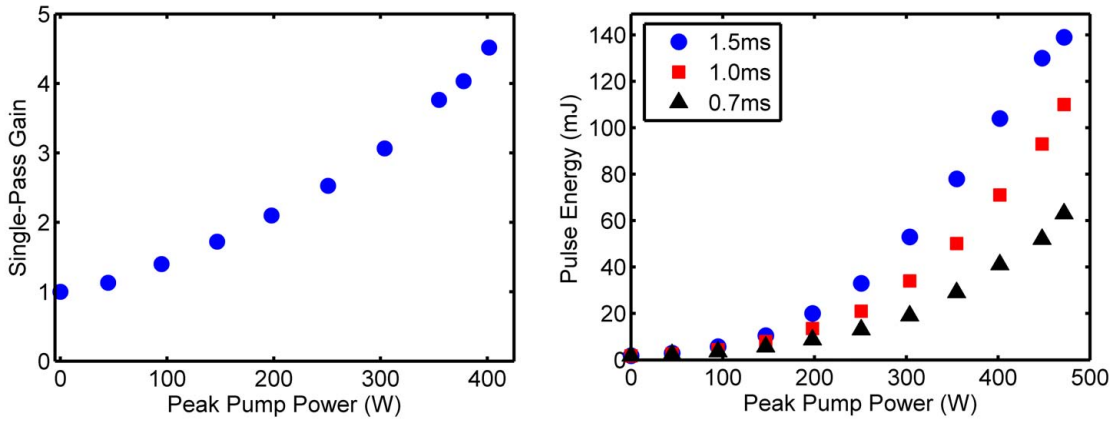

(a) (b)

Figure 2.16: (a) Single-pass small signal gain of the cryogenically-cooled multipass amplifier as a function of peak pump power at 100 Hz repetition rate. The pump pulse duration was 1.5 ms. (b) Energy obtained from the cryogenically-cooled multipass amplifier as a function of peak pump power at 100 Hz repetition rate for pump pulse durations of 1.5 ms, 1.0 ms, and 0.7 ms. The amplifier was seeded with 2.4 mJ pulses from the room temperature regenerative amplifier discussed above. The peak energy achieved was 140 mJ at 100 Hz repetition rate.

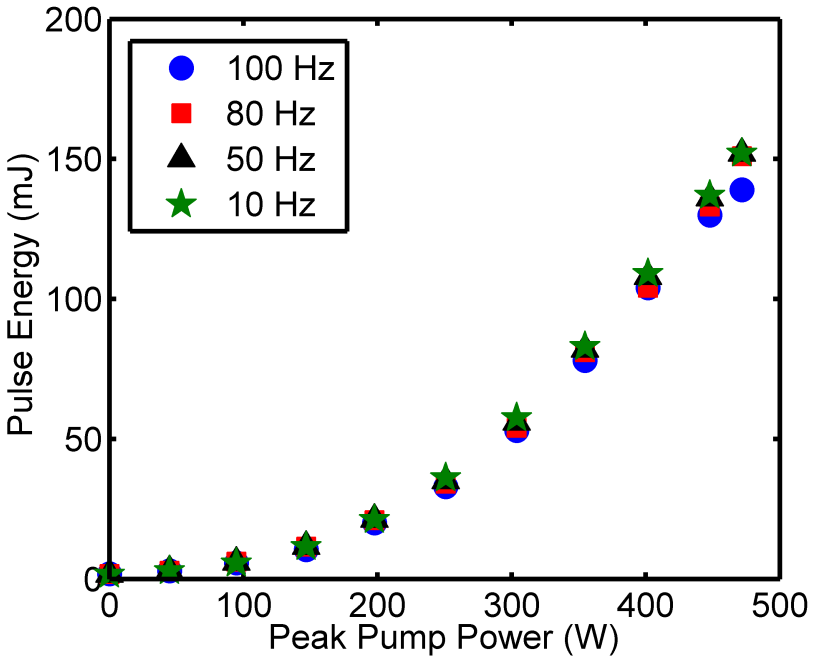

Figure 2.17: Energy obtained from the cryogenically-cooled multipass amplifier as a function of peak pump power for four different repetition rates. The pump pulse duration was 1.5 ms and the amplifier was seeded with 2.4 mJ pulses from the room temperature regenerative amplifier discussed above. The power scaling of the amplifier as a function of repetition rate is excellent showing very little change in energy up to 100 Hz.

polarizers. An output pulse energy of 140 mJ was obtained at 100 Hz repetition rate at a pump power of 470 W. The amplifier is very stable with a shot to shot standard deviation of 0.3% at 100 Hz, which is slightly better than the shot to shot deviation of the regenerative amplifier seeding the amplifier, this is possible because of saturation in the second amplifier. At the maximum output pulse energy the amplifier has an optical to optical efficiency of 20% which exceeds that reported for room temperature Yb:YAG amplifiers producing similar energies [66, 68]. Furthermore, higher efficiency could be achieved by increasing the fraction of absorbed pump power through double-passing the pump beam or increasing the Yb doping percentage. The well behaved thermal response of this amplifier can be seen in Figure 2.17, which shows the energy obtained as a function of peak pump power for repetition rates ranging from 10Hz-

100Hz. At repetition rates up to 80 Hz an energy of about 152 mJ is obtained, with no thermal effects noticeable. At 100Hz repetition rate, there is a slight reduction of the amplified energy to 140 mJ, which is due to a lower gain caused by localized heating. The amplified pulses have good beam quality, as can be seen from Figure 2.18, which shows near-field and far-field images of the beam after this amplifier along with a measurement of the M^2 factor. The measurement for both axes is $M^2 < 1.1$. However the beam is a slightly oval resulting from the asymmetrical gain profile of both the first and second stage amplifiers.

The spectrum of the amplified pulses exiting the multipass amplifier is shown in Figure 2.19(a). During amplification the spectrum narrows to 0.35 nm FWHM due to the narrow bandwidth of Yb:YAG at cryogenic temperature. The full energy pulses (140 mJ) were compressed with 72% efficiency to 4.8ps FWHM duration ($sech^2$) pulses of 100 mJ energy. A SHG autocorrelation trace of the compressed amplified pulses along with a $sech^2$ fit is shown in Figure 2.19(b).

This stage of amplification produces 140 mJ laser pulses at 100 Hz repetition rate with good beam quality to seed the Joule-level, 3^{rd} stage amplifier discussed in the next section.

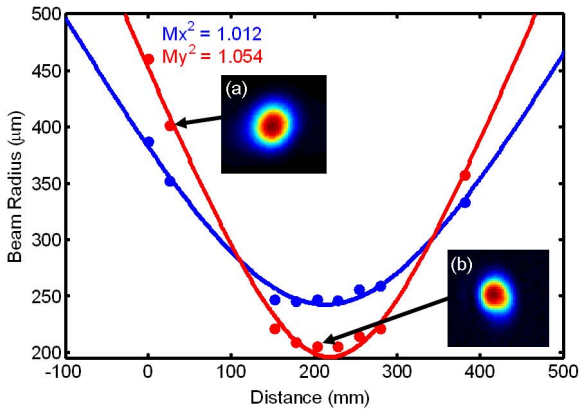

Figure 2.18: M^2 measurement of pulses exiting the cryogenic amplifier at 100 Hz repetition rate along with (a) far-field and (b) near-field images. This profile was measured by focusing the beam exiting the amplifier with a 600 mm focal length lens and measuring the 4σ beam width.

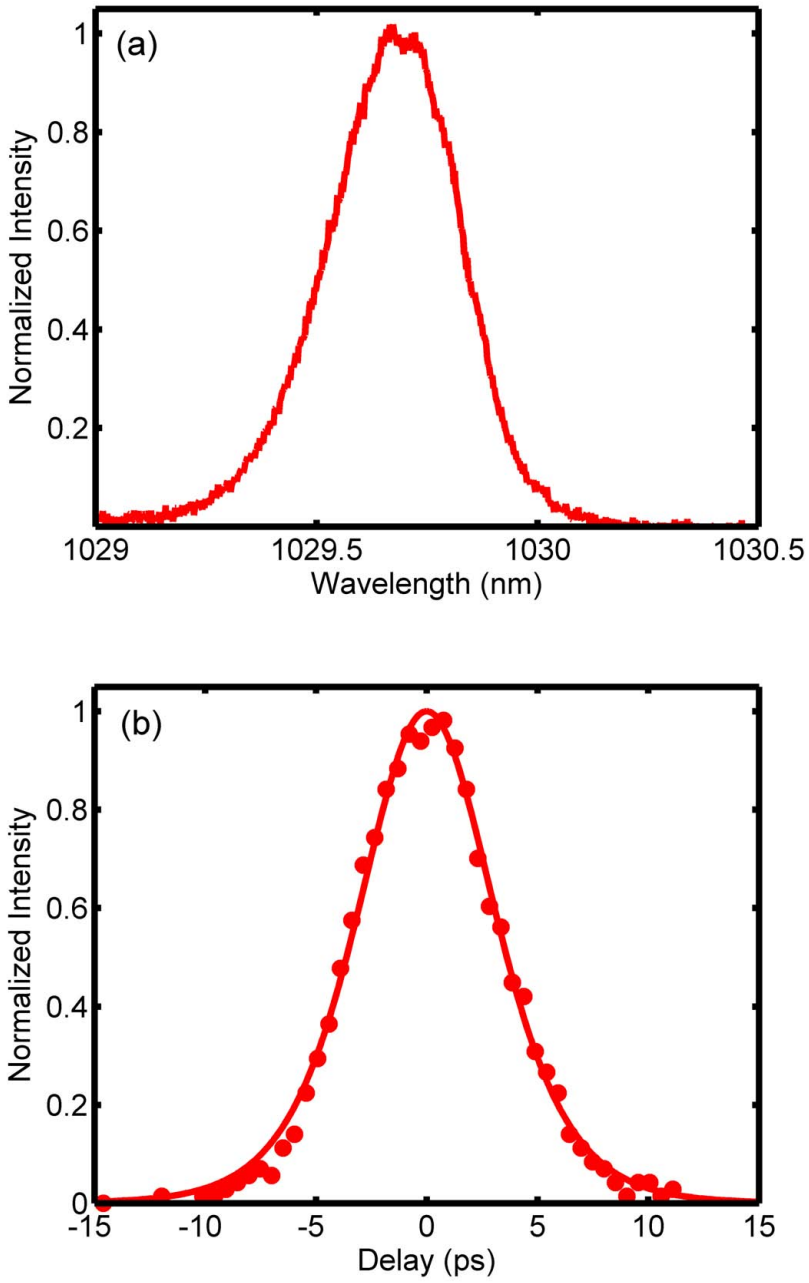

Figure 2.19: (a) Spectrum of laser pulses exiting the cryogenic multipass amplifier at 100 Hz repetition rate. These pulses have a bandwidth of 0.35nm FWHM. (b) Second harmonic generation autocorrelation of the pulses with the solid trace showing a sech^2 fit of the data. These pulses have a 4.9ps FWHM duration assuming sech^2 pulse shape.

2.9 High Repetition Rate Joule-Level Amplifier

The final stage of amplification is the 5-pass cryogenic Yb:YAG amplifier shown in Figure 2.20. This amplifier amplifies the 100mJ-level pulses from the cryogenic 4-pass amplifier described in the previous section to >1 J energy at 50 Hz repetition rate. In this amplifier, two 30 mm x 30 mm x 5.5 mm thick 2%-at Yb:YAG crystals are used in the active mirror configuration and are mounted in vacuum to a cryogenically-cooled head. Each crystal is pumped with up to 4.5 kW peak power pulses from 45 bar laser diode stacks emitting at 940 nm, with a total average pump power at 50 Hz repetition rate of over 700 W. The cryogenic cooling system developed to cool the Yb:YAG crystals is discussed first, followed by a description of the pump laser and beam reshaping optics. The resulting energy, beam quality, and pulse compression are then presented.

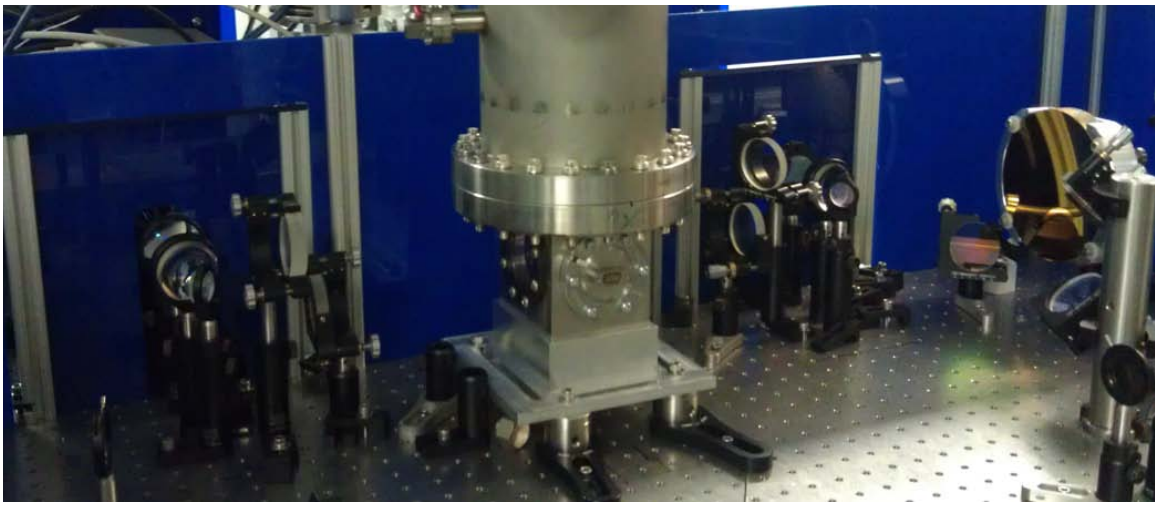

Figure 2.20: Photograph of the main amplifier. The crystal chamber is in the center, with the mirrors that comprise the multipass optics are also shown. One of the large mirrors for imaging the pump beam is visible on the right.

2.9.1 Cooling system

In conventional high power, thin disk lasers the laser crystal is soldered with low temperature indium or tin-indium solder to a copper heat sink which is then water-cooled. However, copper and YAG (and other Yb host materials) have very different coefficients of thermal expansion. When the soldered assembly is cooled to cryogenic temperature a large deformation occurs in a manner similar to a bi-metal as shown in Figure 2.21. The simulated deformation has a magnitude of about 70λ, which is unacceptable for an optic in a high power laser system. In addition to this simulation, we have experimentally observed the deterioration of beam quality that is obtained with this cooling method.

Another cryogenic cooling approach is to cool the laser crystal through direct contact with liquid nitrogen. This technique has been implemented successfully in several CW and ns-pulsed laser systems [98, 99], however there is a limitation in the heat flux that can be dissipated at low temperatures. At the lowest heat flux, heat is

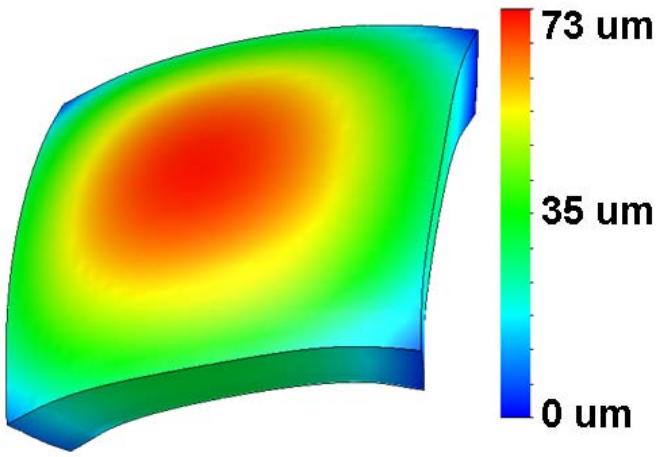

Figure 2.21: Finite element simulation of the deformation of a 30mm x 30 mm x 5.5 mm thick YAG crystal soldered to a copper heat sink upon cooling from room temperature to 77 K. The simulation included the temperature dependant expansion coefficients and elastic moduli of YAG and copper and assumed that the two materials are rigidly attached. A deformation of about 70 wavelengths resulted across the entire surface.

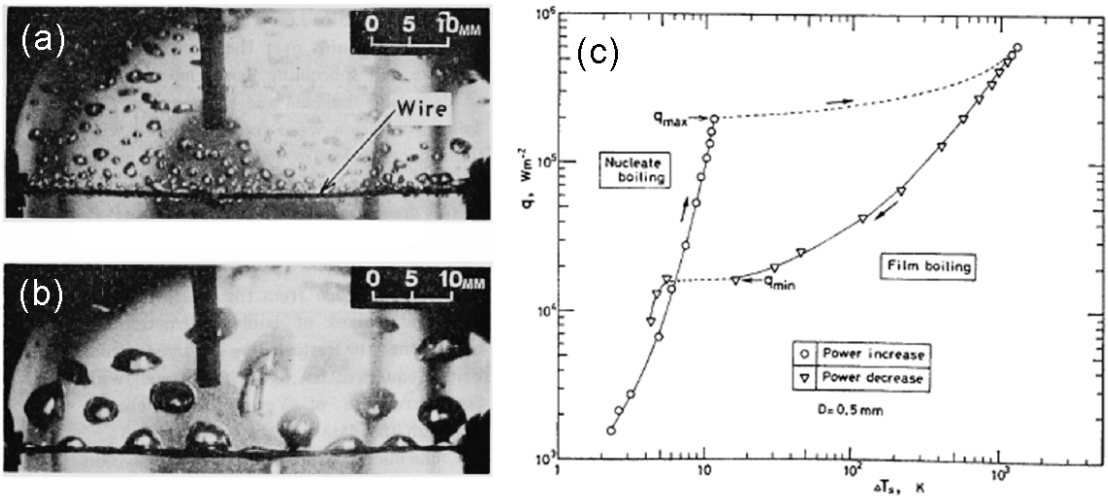

Figure 2.22: (a) Photograph of nucleate boiling occurring in liquid nitrogen from an electrically heated wire. (b) Film boiling. (c) Log-log plot of the different regimes of boiling heat transfer in liquid nitrogen. The heat flux is plotted as a function of the temperature difference between the surface and the liquid. From [97].

carried away from the crystal through free convection in the liquid nitrogen. As the flux is increased, nucleate boiling occurs on the surface of the crystal in which small bubbles form. This is the regime where most liquid nitrogen cooled lasers operate. In the nucleate boiling regime modest heat power fluxes can be achieved, and the temperature difference between the liquid nitrogen and the boiling surface is less than 10° C. If the heat power increases above a certain flux, known as the critical heat flux, the system departs from nucleate boiling into the film boiling regime. In this regime, the large amount of vapor locally formed shields the surface from contact with the liquid resulting in large drop in heat transfer efficiency. This is illustrated in Figure 2.22 which shows photographs of nucleate and film boiling in liquid nitrogen along with a plot of the heat power flux as a function of temperature difference between the surface and the liquid. As can be seen from this figure the critical heat flux for liquid nitrogen was measured to be about 20 W/cm^2 [97], although this depends on the surface material, roughness, and orientation. For practical purposes, this is the maximum thermal flux that can be cooled through direct contact with

boiling liquid nitrogen.

We experimentally determined that under our maximum pump conditions, 4.5kW peak power in a 1.5 ms duration pulse in a 16mm diameter spot on each crystal, that the critical heat flux limited us to about 20 Hz repetition rate using the direct liquid nitrogen cooling method. At repetition rates above 20 Hz, the crystals rapidly heated to very high temperatures. This motivated us to develop a novel cryogenic cooling technique for solid state lasers, direct forced convective cooling with a sub-cooled cryogenic liquid.

Figure 2.23 shows a block diagram of the cooling system. In this system, liquid oxygen is cooled to liquid nitrogen temperature in a vacuum-jacketed reservoir. Liquid oxygen was chosen because it has a boiling point of 90 K and a freezing point of 54 K at atmospheric pressure, and is therefore liquid and 13° C below its boiling point at the liquid nitrogen boiling temperature of 77 K. The liquid oxygen is first pumped through a heat exchanger at liquid nitrogen temperature consisting of a length of thin-walled copper tubing surrounded by liquid nitrogen. The sub-cooled liquid oxygen is then transported to the laser head by vacuum-jacketed stainless steel hoses. Inside the laser head, the liquid oxygen flows in a narrow channel across the HR face of each

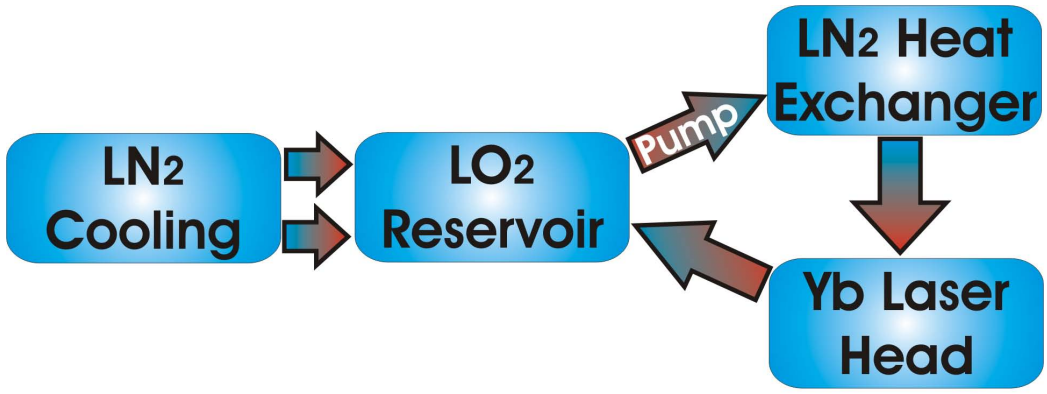

Figure 2.23: Block diagram of the cryogenic cooling system for the Joule-level amplifier. Liquid oxygen is pumped through a liquid nitrogen-cooled heat exchanger cooling it to about 77 K. The sub-cooled liquid oxygen is then pumped through vacuum jacketed lines to the amplifier head where it directly cools the laser crystals. The liquid oxygen then returns to the reservoir which is also cooled by liquid nitrogen.

Yb:YAG crystal. The flow on the back of the crystal is turbulent, Reynolds number = 2.1 $\times 10^4$, allowing the liquid oxygen to be heated uniformly. The liquid oxygen then returns to the reservoir, remaining liquid throughout the whole process, removing the limitation of the critical heat flux that accompanies boiling heat transfer. The flow is sufficient to cool the amplifier when operated at 100 Hz repetition rate with a $\approx 2^\circ$ C temperature rise in the fluid assuming *all* of the pump power is converted to heat. This assumption is of course the worse case, only a fraction of the pump power is locally converted to heat.

The computed temperature distribution of the Yb:YAG crystals under 100 Hz repetition rate operation is shown in Figure 2.24. This finite element simulation assumed that the Yb:YAG crystal was pumped with 4 kW, 1.5 ms $\lambda = 940$ nm pulses at 100 Hz repetition rate in a 16 mm diameter spot and only the thermal defect fraction contributed to heating. Under these conditions, the maximum temperature increase is about 6° C, and the gradient is primarily longitudinal in the gain region. The amplifier head, shown in Figure 2.24(a), is made of invar, which is a low thermal expansion nickel-iron alloy. The difference in thermal contraction between invar and YAG is minimal, compared to other common metals. This results in minimal deformation of the laser crystal due to thermal contraction as shown in the simulation results of Figure 2.24(c).

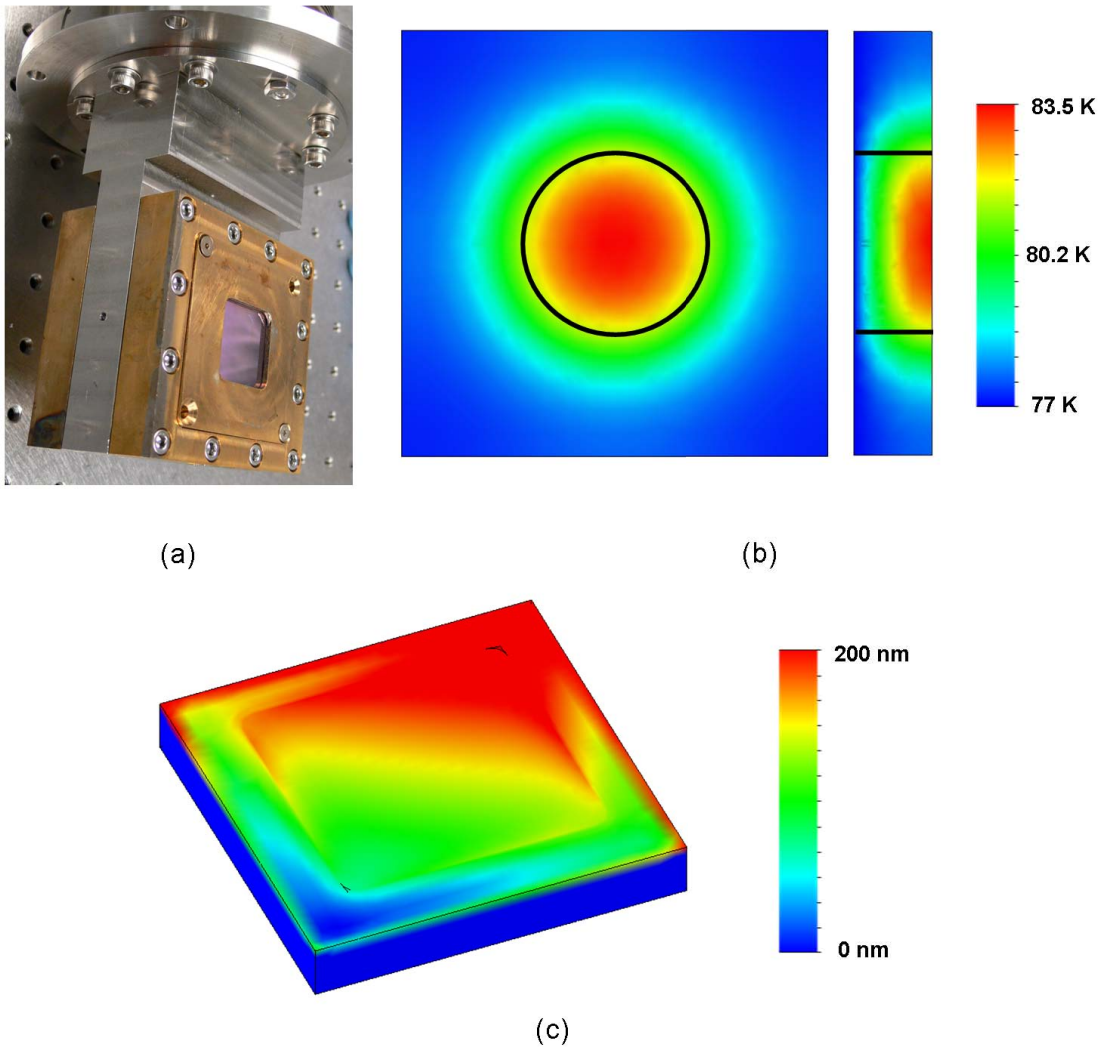

Figure 2.24: (a) Photograph of the two Yb:YAG crystals mounted on the invar amplifier head. (b) Computed temperature distribution in the Yb:YAG crystals at 100 Hz repetition rate operation. The profiles on the AR face and in cross-section are shown. The bold lines indicate the gain region. (c) Finite element simulation of the minimal deformation of the symmetrically stressed Yb:YAG-invar assembly when cooled to liquid nitrogen temperature.

2.9.2 High Power Laser Diode Pump System

Each crystal in the amplifier is pumped by a 4.5 kW average power laser diode array emitting at $\lambda = 940$nm with a spectral width of 5 nm FWHM. Each array is a vertical stack of 45 laser diode bars with a width of 10 mm and height of 1.5 mm. Each bar has a microlens to collimate the fast axis of the individual emitters resulting in a vertical divergence of $^1/_4{}^\circ$ FWHM. The arrays have a slow axis (horizontal) divergence of about 10° FWHM. The resulting beam profile is composed of a series of vertical lines that is about 75 mm tall x 10 mm wide that is quickly diverging horizontally. In order to reshape this beam into a round, uniform spot suitable for pumping the amplifier we developed the system shown in Figure 2.25 that combines both imaging and nonimaging optics.

In order to reshape the beam into a round homogeneous spot the pump light is focused into a 4 mm diameter silica rod. The beam is reshaped and homogenized by many total internal reflections (TIR) from the outside edge of the rod. To couple the

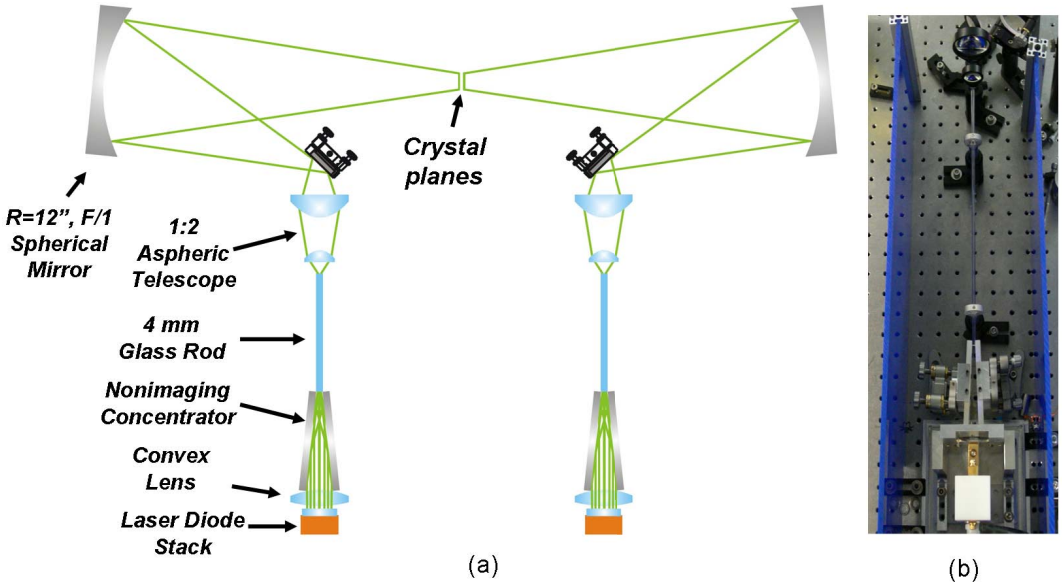

Figure 2.25: (a) Schematic diagram of the optical pump system for the Joule-level amplifier. (b) Photograph showing a laser diode stack, focusing lens, nonimaging concentrator, beam reshaping and homogenizing rod, and aspheric telescope.

pump light into the rod, a 12 cm focal length plano convex lens is used to focus the collimated vertical axis into a small width. A nonimaging concentrator consisting of two 75 mm x 100 mm dielectric multilayer mirrors guides the pump radiation in the horizontal axis into a 3-4 mm wide spot allowing for efficient coupling into the rod [100]. In order to couple the beam exiting the rod into the laser crystal, the plane of the end the rod is imaged onto the crystal plane by a two aspheric lenses and a large aperture f/1 spherical mirror. The two aspheric lenses form a 1:2 telescope reducing the excessive divergence of the light exiting the rod and producing an 8 mm image on the 45° flat mirror. The pump beam is then relay imaged by the concave mirror with a magnification of about 2x onto the crystal. This system was designed using raytrace simulations. A measured image of the pump profile in the laser crystal plane is shown in Figure 2.26. The pump profile is close to flat with soft edges and is free of damage-causing hot features. The profile has a diameter of about 16 mm FWHM with nearly all of the energy contained within a 17 mm diameter. This system was measured to have an overall efficiency of 88% at the maximum power.

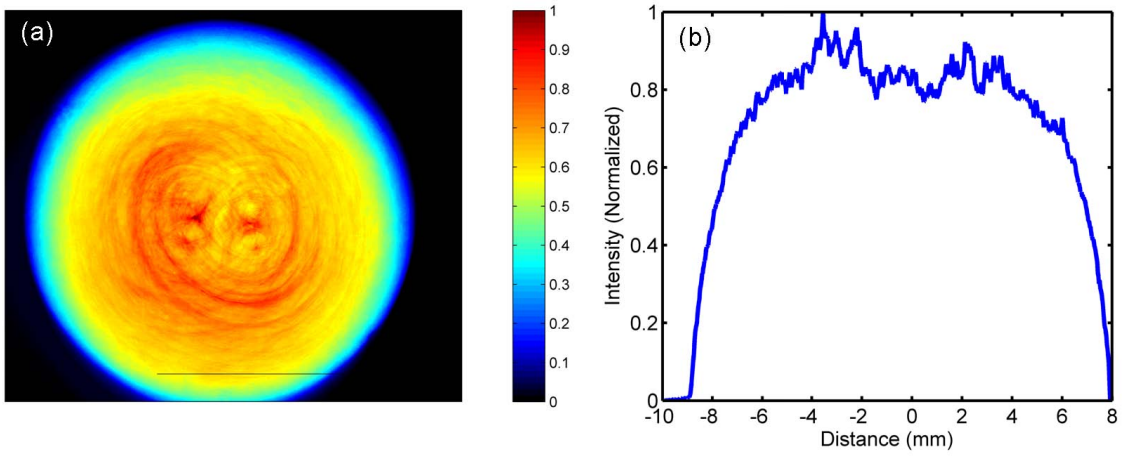

Figure 2.26: (a) Measured image of the pump beam. The pump profile is flattop with soft edges and is free of any *hot spots*. (b) Horizontal lineout of the pump profile. The width of the profile is ≈16 mm FWHM.

2.9.3 Performance

Figure 2.27 shows the beam path of the laser through the amplifier. 100 mJ pulses from the second stage cryogenic amplifier are first spatially filtered by an 8 mm diameter serrated aperture that removes the low intensity tails of the beam profile without causing excessive diffraction effects. This results in a more flat-top beam profile. The beam is then made to diverge slightly as it passes through the amplifier. The beam makes two passes through the crystal on the left and three passes through the right crystal. A pass is defined here as passing through the crystal, reflecting off the HR coating on the back face, and passing back through the crystal. In order to accomplish these passes in a small footprint the beam is not confined to a single plane as can be seen from the figure.

Figure 2.28 shows the output energy as a function of peak pump power at 50 Hz repetition rate of the 5-pass amplifier when seeded with 100 mJ pulses from the second stage amplifier. The pump pulses had a square profile of 1.7 ms duration. At the maximum peak pump power of nearly 8kW, a pulse energy of 2 J was obtained at 50 Hz, however at this energy optical damage occurs sporadically on the AR surfaces

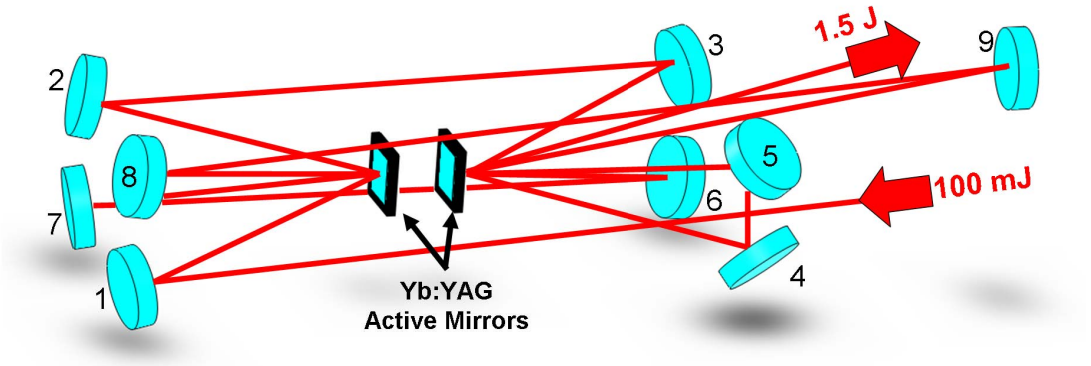

Figure 2.27: 3-D perspective illustration of the multipass Joule-level amplifier. The pump beams and optics, crystal chamber and optics mounts are omitted for clarity. 100 mJ pulses from the 2nd stage make a total of 5 passes through the two Yb:YAG crystals (two for the left crystal, three on the right crystal). The mirrors are numbered in the order that the beam is incident on them.

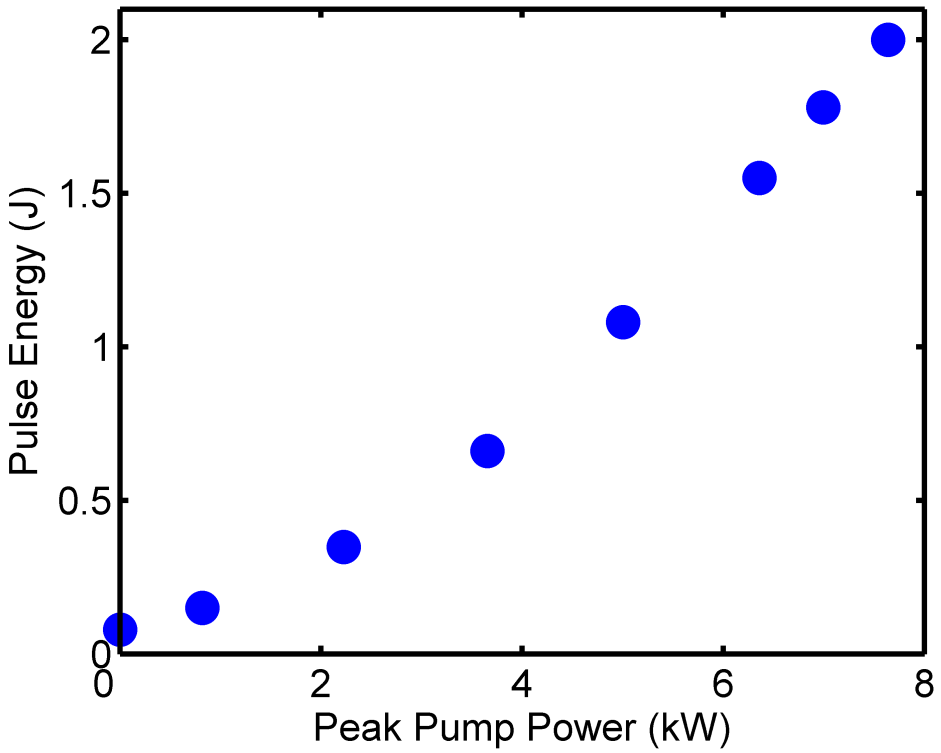

Figure 2.28: Output pulse energy of the 5-pass, Joule-level amplifier as a function of peak pump power at 50 Hz repetition rate. Optical damage occurs at the highest energies, for reliable operation the amplifier output energy is maintained at 1.5 J.

of the laser crystals and on the vacuum-side of the AR-coated window on the crystal chamber. For reliable, non-damaging operation the output energy of this amplifier is limited to 1.5 J. The optical to optical efficiency of the amplifier when producing 1.5 J pulses at 50 Hz repetition rate is 15%, which is comparable to other diode pumped amplifiers producing greater than 100 mJ pulses [66, 68].

The amplified pulses have good beam quality as can be seen from the measurement shown in Figure 2.29. For this measurement the 1.5 J pulses at 50 Hz repetition exiting the amplifier were focused with a 500 mm focal length lens and the beam was measured with a CCD. The 4σ width was determined in each direction for each image and a least-squares fit to the Gaussian propagation equation was made to determine the M^2 parameters. The M^2 parameter for the x and y axes are 1.16 and 1.24 respectively. There is some residual astigmatism, but is not significant enough

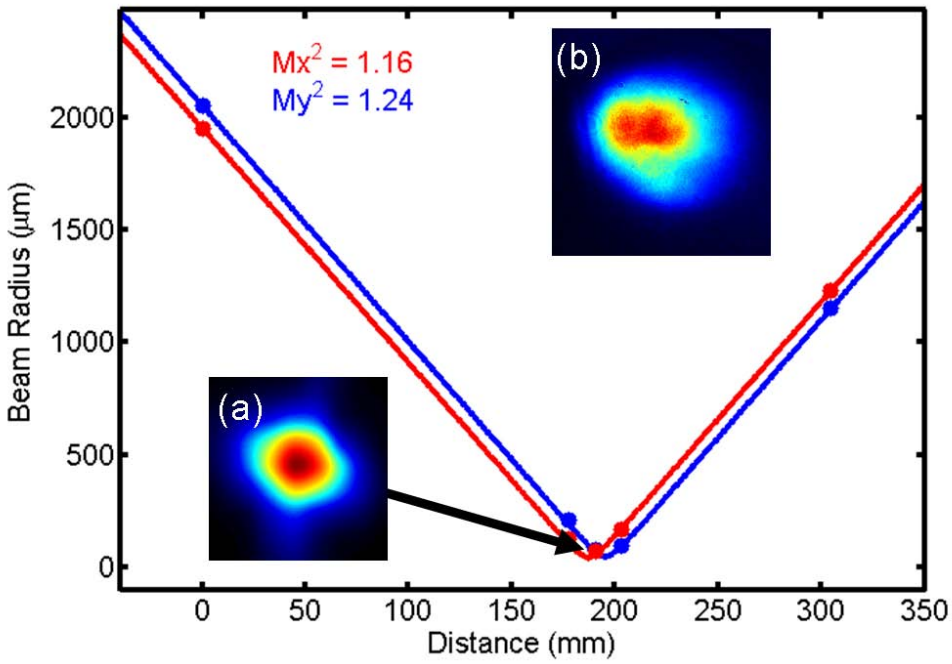

Figure 2.29: M^2 measurement of the 3rd stage amplified pulses at 50 Hz repetition rate with (a) near field and (b) far field beam images. The beam was focused with a 500 mm focal length lens for the measurement. The M^2 of both axes are less than 1.25.

to cause concern for our purposes. The far field profile shows that most of the energy is concentrated in a relatively flat-top area in the center and is free of any hot spots or significant modulation. The peak fluence at 1.5 J energy is about 1.2 $\frac{J}{cm^2}$, and no nonlinear effects such as self-focusing were observed. Furthermore, no thermal lensing was observed.

The pulses exiting this amplifier are compressed to picosecond duration by a pulse compressor composed of high efficiency, high damage threshold dielectric gratings. This compressor is discussed in the next section.

2.10 Grating Pulse Compressor

Figure 2.30 (a) shows a schematic diagram of the pulse compressor. The compressor consists of two high efficiency, high damage threshold multilayer dielectric gratings

with 1740 lines/mm optimized for a wavelength 1.03 μm. The amplified beam exiting the final amplifier is expanded to a width of 40mm (3ω) to reduce the fluence and minimize the risk of optical damage to the gratings. The angle of incidence on the first grating is about 55.5° and the distance between the gratings is about 2510 mm in order to achieve the shortest pulse duration. The compressor is folded twice to attain this large distance in a minimal footprint. The compressor supports a bandwidth of 1 nm, as can be seen from the raytrace simulation of the Figure 2.30(b), and it is contained in a vacuum chamber to prevent distortions of the high intensity beam. Under the parameters above, the grating diffraction efficiency is about 95%, and the overall efficiency of the compressor was measured to be 75%. This allows the 1.5 J pulses generated at 50 Hz repetition rate to be compressed producing ≈1 J energy

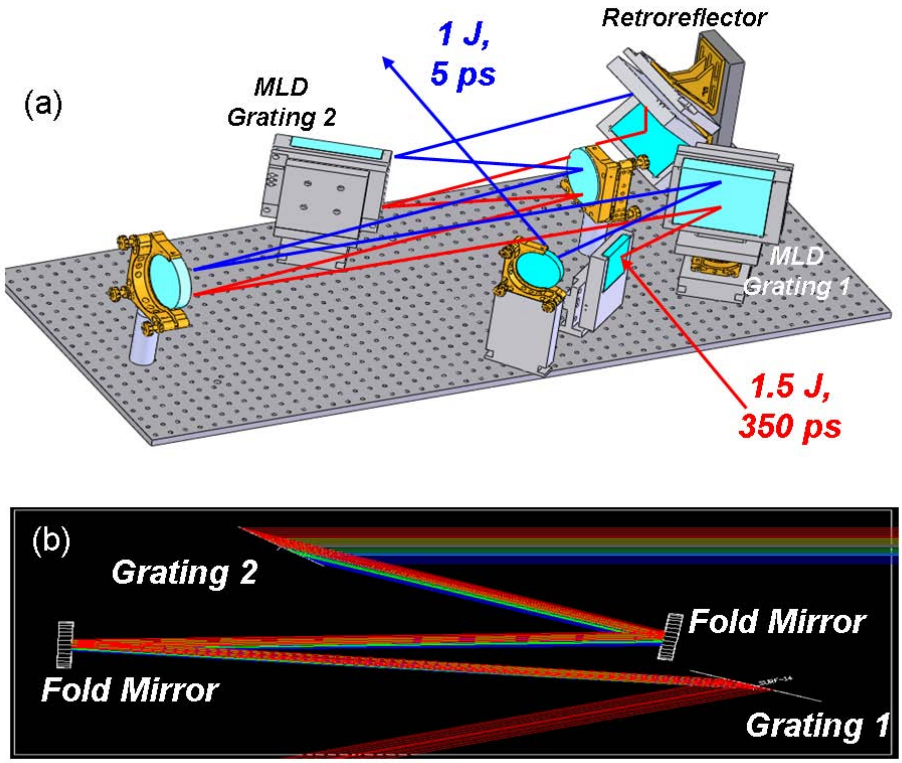

Figure 2.30: (a) 3-D schematic of the grating pulse compressor. The first pass throught the compressor is shown in red, while the second pass is traced in blue. (b) Raytrace simulation of the compressor. The difference in wavelength between the red and blue traces is 1 nm.

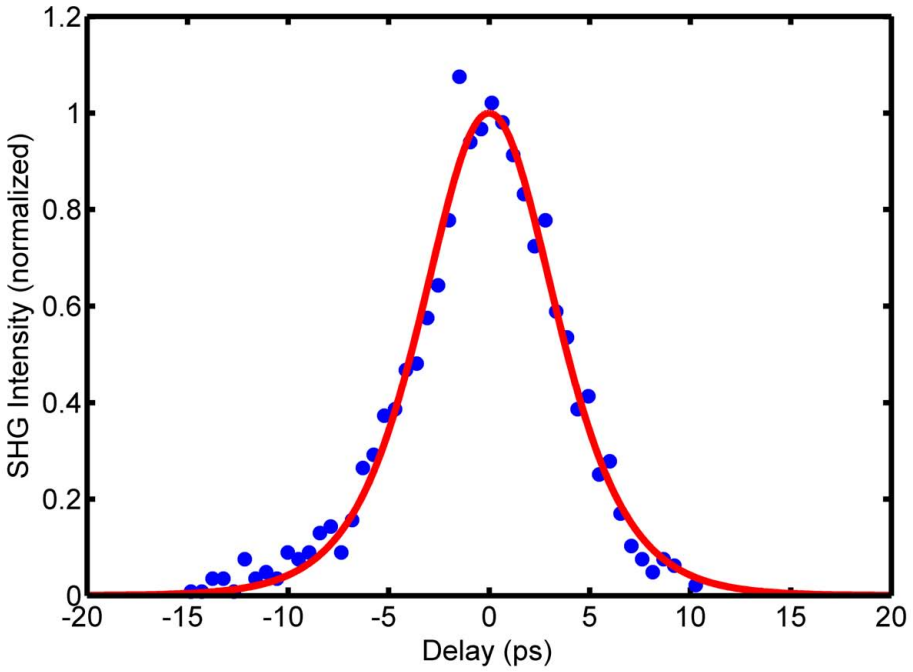

Figure 2.31: Second harmonic generation autocorrelation of compressed 1 J pulses at 50 Hz repetition rate. The trace is a least squares sech^2 fit of the data. Assuming this pulse shape, the pulses have a duration of 5.1 ps FWHM.

pulses with 5 ps FWHM duration. Figure 2.31 shows the SHG autocorrelation of 1 J laser pulses exiting the compressor. Assuming a sech^2 pulse shape the compressed pulses have a duration of 5.1ps FWHM, which is nearly the same as the 4.9 ps FWHM pulses acheived with the 100 mJ pulses exiting the 2nd amplification stage. This shows that there is negligible further narrowing of the bandwidth upon amplification to Joule-level.

2.11 Summary

We have developed a compact, all diode pumped, chirped pulse amplification laser system based on Yb:YAG that produces 1.5 J pulses at 50 Hz repetition rate. The system output was compressed resulting in 5 ps duration 1 J laser pulses. To the best of our knowledge, this is the highest repetition rate CPA laser to produce Joule

pulses demonstrated to date. This high average power was made possible by a novel cryogenic cooling technique, direct cooling with a sub-cooled cryogenic liquid. The short pulse duration and high average power was achieved by combining a broader bandwidth room temperature Yb:YAG preamplifier with the excellent thermal characteristics and high gain of cryogenic Yb:YAG power amplifiers. These techniques can be scaled to higher repetition rates and higher pulse energies. This compact and efficient high power picosecond laser system is expected to have a significant impact in applications such as the pumping of high average brightness table-top soft x-ray lasers, the efficient x-ray generation from plasmas, and in pumping of optical parametric amplifiers for the generation of high intensity laser pulses of a few femtosecond duration.

Chapter 3

Demonstration of an All-Diode-Pumped Soft X-Ray Laser

3.1 Introduction

In this chapter, the first demonstration of a soft x-ray laser driven by a diode-pumped laser is described [67]. Lasing was obtained on the 18.9 nm line of nickel-like molybdenum at a repetition rate of 10 Hz. Figure 3.1 shows a block diagram of the soft x-ray laser system. The driving laser is a version of the system described in Chapter 2 with a different amplifier configuration that produces 1 J, 8.5 ps duration laser pulses at 10 Hz repetition-rate. This laser, with the exception of the pulse compressor, occupies a single 5 x 12 ft^2 optical table. The pump laser is based on the passively mode-locked Yb:KYW laser oscillator described in the previous chapter, a cryogenically-cooled Yb:YAG regenerative amplifier, and a cryogenically cooled Yb:YAG multipass amplifier, all pumped by laser diodes.

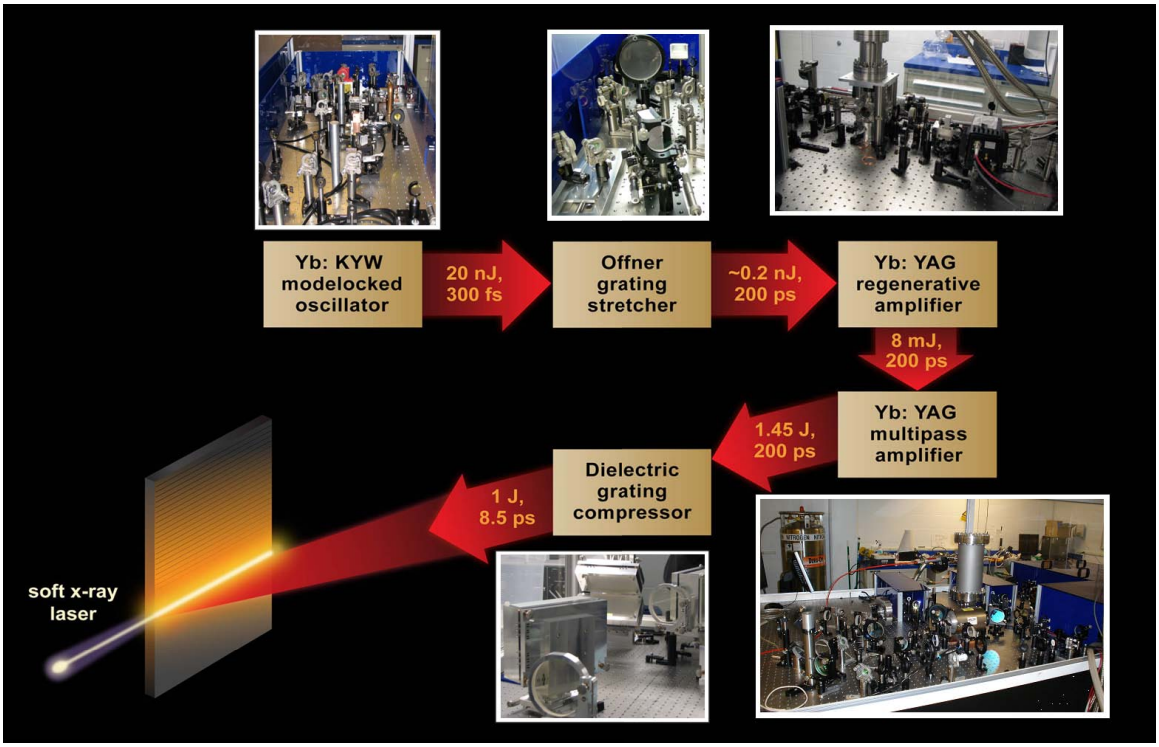

Figure 3.1: Block diagram of the diode-pumped soft x-ray laser. The oscillator, stretchers and amplifiers fit on a single 12' x 5' optical table.

3.2 Diode-Pumped Cryogenic Yb:YAG CPA Laser

The output of the laser oscillator described in the previous chapter is divided to generate a sequence of three amplified 1.03 μm laser pulses that are used to generate the soft x-ray laser. The first and second pulses are sent through a negative GVD stretcher, while the third pulse is sent through the positive GVD stretcher previously described. After amplification, the duration of the first two pulses is 160 ps and the duration of the third pulse is 200 ps. The relative energies of the pulses and the delays between them are adjusted, the pulses are recombined, and then sent to the amplifiers and a grating pulse compressor (negative GVD grating pair). This grating pair further stretches the first two pulses while compressing the final heating pulse. This allows us to generate a sequence of two long pulses for plasma creation, followed by a short, plasma heating pulse. Furthermore, since the alignment of the three beams is determined by the cavity of the regenerative amplifier, the spatial overlap

of the three pulses is ensured by design.

The first stage of amplification is a cryogenically-cooled regenerative amplifier that boosts the combined pulse energy to 7 mJ using a 2 mm thick 5 %-at Yb:YAG crystal that is cryo-cooled using a closed cycle helium cryostat. The crystal temperature is tuned to about 100 K utilizing an electrical heater to increase the bandwidth of the amplified pulses. The regenerative amplifier is pumped by a 90 W fiber-coupled laser diode emitting at a wavelength of 940 nm. The diodes are modulated to produce 1.2 ms pulses that are focused into a ≈400 μm diameter spot on the crystal. The repetition rate of the amplifier was varied between 10 and 100 Hz with practically no reduction in energy or beam quality.

The millijoule pulses exiting the regenerative amplifier increased to the Joule-level in a compact multi-pass amplification stage, schematically shown in Figure 3.2. The gain medium is split into two 5.5 mm thick 2%-at Yb:YAG crystals in an active-mirror configuration. Off-axis spontaneous emission is absorbed by a Cr:YAG cladding elim-

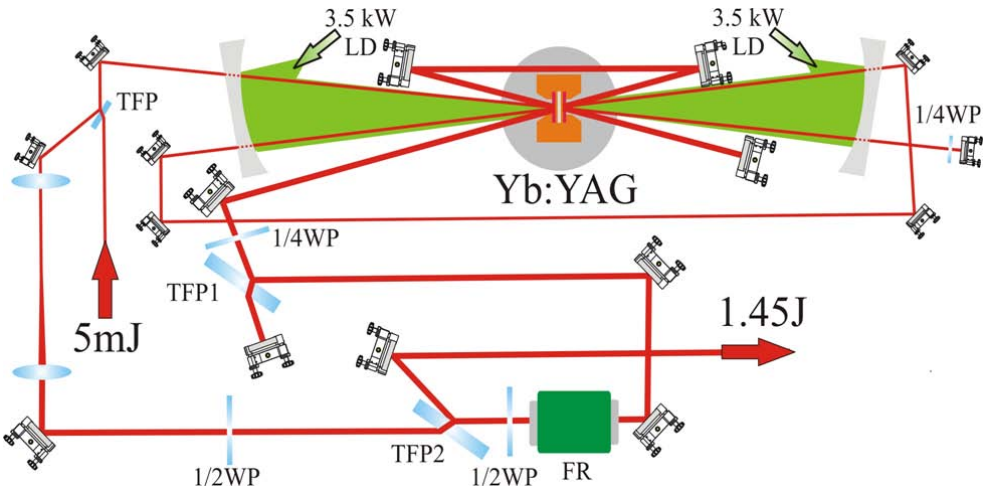

Figure 3.2: Schematic layout of multi-pass amplifier. The beam from the regenerative amplifier makes four passes through the gain medium changing the polarization from p to s after the second pass. Next the beam is expanded, sent through the Faraday rotator, and further amplified in additional four passes. Subsequently the polarization changes from s to p, the beam goes through TFP1 and is sent back on itself to make four more passes. Finally the beam switches polarization back to s, and is ejected by TFP2. FR: Faraday Rotator; WP: Waveplate; TFP: Thin Film Polarizer.

inating parasitic lasing. The crystals are mounted on the opposite faces of a cold finger that is cooled by liquid nitrogen in an evacuated chamber. Each of the crystals is pumped by 3.5 kW pulses of 2 ms duration produced by a stack of 940 nm laser diodes. The pump beams are shaped to illuminate a circular region of 16 mm diameter on each of the Yb:YAG laser crystals. The beam exiting the regenerative amplifier makes 12 passes through the amplifier. The beam diameter is increased to 8 mm to make the initial four passes through the amplifier (two on each crystal) passing through small holes in the large mirrors used to focus the pump beams onto the crystals. After these initial four passes the amplified pulses reach ≈100 mJ. Subsequently, the beam is expanded to match the size of the pump beams and is sent eight additional times through the gain media (four times through each crystal) by means of changing the polarization. In Figure 3.3(a) the energy of the pulses exiting the amplifier is plotted as a function of diode pump power. We measured a maximum energy of 1.45 J at 10 Hz repetition rate. The laser was operated at repetition rates up to 50 Hz with slight thermal lensing, but with significantly decreased output pulse energy due to a reduction in the gain caused by localized heating of the gain medium that lowers the stimulated emission cross-section. A reduction of the excessively long

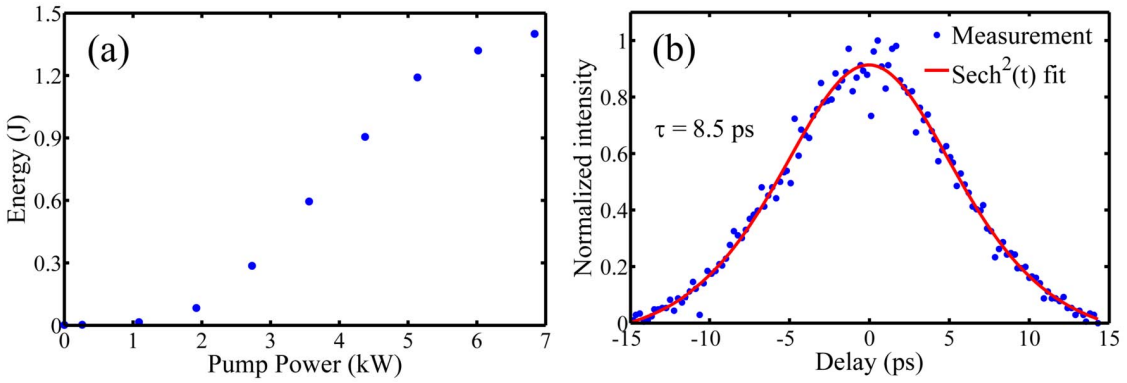

Figure 3.3: (a) Un-compressed Yb:YAG laser output pulse energy as a function of pump peak power from 2 ms pump pulses. A maximum energy of 1.45 J was obtained with a peak pump power of 7 kW. (b) Hyperbolic secant squared fit of the autocorrelation data corresponding to 8.5 ps FWHM pulses

rise and fall times of the diode laser pulses used in the present set up combined with better thermal management can help to mitigate this limitation. Non-linear effects were observed to have an onset at about 1 J, but the B-integral can be reduced by further stretching the input pulse.

3.3 Demonstration of an 18.9nm Soft X-Ray Laser

The amplified pulses are sent to a 70% efficient pulse compressor in vacuum based on dielectric multilayer gratings. The short pulse is compressed to 8.5 ps FWHM ($sech^2$ pulses) as shown in the autocorrelation trace in Figure 3.3(b), while the pre-pulses are further stretched to 350 ps FWHM. This sequence of pulses is shown in Figure 3.4.

To generate the soft x-ray laser, this set of collinear pulses is focused at a grazing incidence angle of 29 degrees into a 4 mm wide polished Mo target to form a 3.5

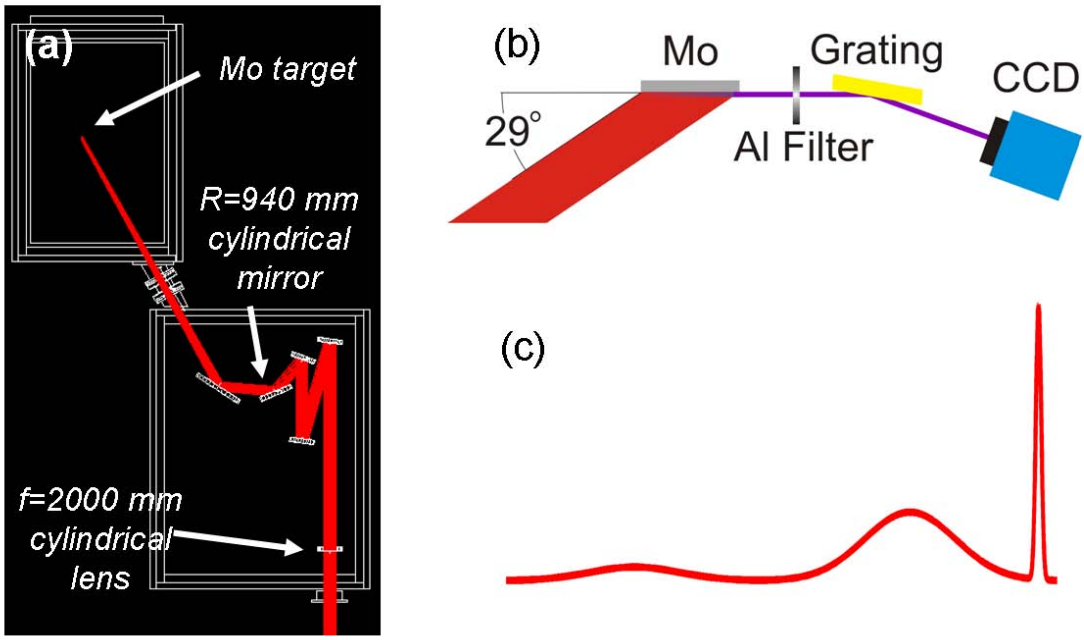

Figure 3.4: (a) Raytrace of the line focusing optics for generating the x-ray laser. (b) Illustration of the soft x-ray spectrometer for characterizing the plasma emission. (c) A sequence of two 350 ps pulses and one 8.5 ps pulse creates and heats the Mo plasma.

mm FWHM long line with a width of ≈35 μm FWHM. The line focus was generated by the combination of a cylindrical lens to focus the beam horizontally along the length of the line, and a cylindrical mirror used at the same angle of incidence as the target to focus vertically. This is illustrated in the raytrace of Figure 3.4. The x-ray detection setup is shown in Figure 3.4(b). The axial soft x-ray plasma emission is analyzed using a 1200 mm^{-1} variable space grating and a back-thinned CCD. Two 0.3 μm thick aluminum filters were used to block the visible light emitted by the plasma. Figure 3.5(a) shows a single shot on-axis spectra taken with 700 mJ of total pump energy incident on the target. The intensity of the 18.9 nm spectral line is at about the same level as other spectral lines of the plasma emission. However, when the pump energy is increased, there is clear evidence of amplification on the 18.9 nm line of Ni-like Mo as it is shown in Figure 3.5(b). This particular spectrum was obtained

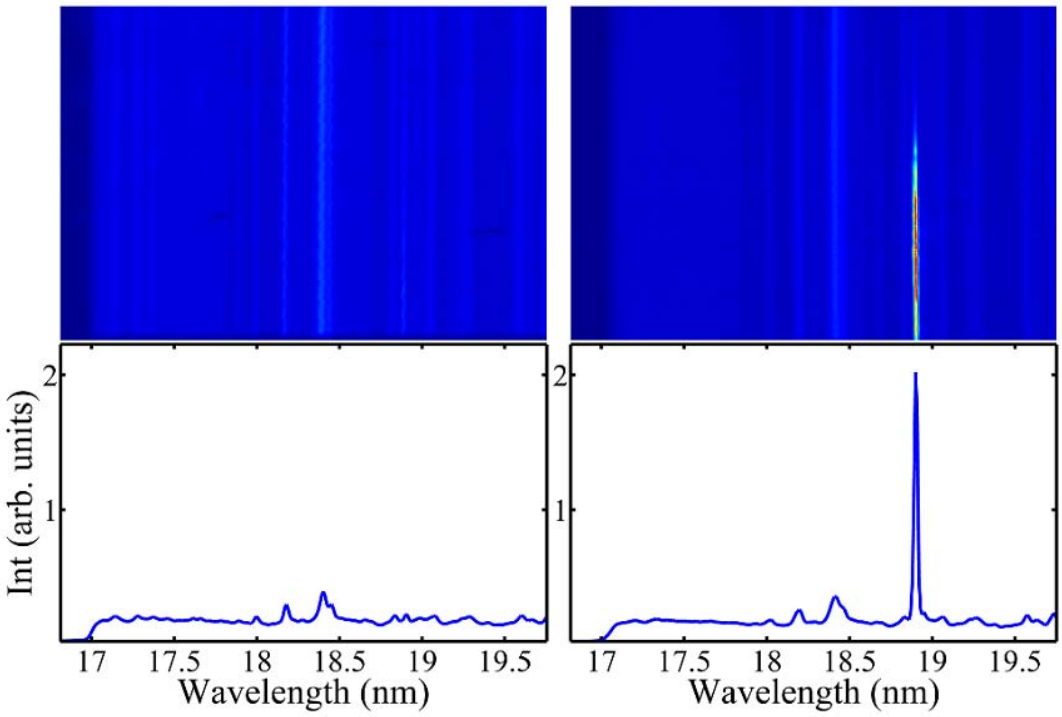

Figure 3.5: (a) On-axis soft x-ray spectrum of the molybdenum plasma taken with a total pump energy on target of 700 mJ. (b) The same spectrum taken with 940 mJ of pump energy, showing lasing in the 18.9 nm laser line of Ni-like Mo.

with a total pump energy on target of about 940 mJ (10 mJ and 320 mJ pre-pulses separated by 4 ns, followed by a 620 mJ short pulse after 800 ps). The non-optimized soft x-ray laser output energy was estimated to be 50 nJ. Improvement of the line focus quality can be expected to significantly increase the output energy.

3.4 Summary

In summary, we have demonstrated the first soft x-ray laser, driven by a solid-state laser system entirely pumped by laser diodes. Lasing in the 18.9 nm line of Ni-like Mo was observed using a compact Yb:YAG system that generates compressed pulses of 8.5 ps duration with up to 1 J energy. Future work can be expected to lead to the development of very compact soft x-ray lasers that will operate at unsurpassed repetition rates.

Chapter 4

Conclusion

In summary, we have developed a compact chirped pulse amplification laser system entirely pumped by laser diodes that produces 1.5 J at 50 Hz repetition rate. Compression results in 1 J pulses with 5 ps FWHM duration. The short duration, high energy, and high average power were enabled by combining a broader bandwidth room temperature Yb:YAG preamplifier with cryogenically-cooled Yb:YAG power amplifiers. This allowed us to take advantage of the low saturation fluence and excellent thermal characteristics of cryogenic Yb:YAG while avoiding excessive bandwidth loss in the first stage of amplification. Furthermore, a new cryogenic cooling technique was developed to allow the Joule-level amplifier to operate at high repetition rate without excessive heating or reduction of beam quality. The technique, heat removal by direct contact with a flowing, sub-cooled cryogenic fluid, allows for high thermal fluxes, in contrast to other cryogenic thermal management techniques. This all-diode-pumped system is the highest repetition rate CPA system that produces 1 J laser pulses demonstrated to date.

Additionally, a version of this laser system was employed to make the first demonstration of a soft x-ray laser driven by an all-diode-pumped laser. Lasing was achieved at 10 Hz repetition rate on the 18.9 nm line of nickel-like molybdenum using tran-

sient collisional grazing incidence pumping. Future work can be expected to lead to the development of very compact soft x-ray lasers at wavelengths below 20 nm that will operate at previously unobtainable repetition rates. This will enable applications requiring high average power such as nanomachining, nanopatterning, some imaging applications.

Planned future work includes further increases of the repetition rate and the demonstration of soft x-ray lasers at increased repetition rate, as well as the generation of ultrashort laser pulses. Additionally, this laser system is an ideal pump source for high energy optical parametric chirped pulse amplifiers producing femtosecond pulses in the mid-infrared region of the spectrum.

References

[1] T. Maiman, "Stimulated optical radiation in ruby," *Nature*, vol. 187, pp. 493–494, 1960.

[2] D. Attwood, *Soft X-Rays and Extreme Ultraviolet Radiation*. New York: Cambridge University Press, 2007.

[3] W. Chao, B. D. Harteneck, J. A. Liddle, E. H. Anderson, and D. T. Attwood, "Soft X-ray microscopy at a spatial resolution better than 15nm," *Nature*, vol. 435, pp. 1210–1213, June 2005.

[4] C. A. Brewer, F. Brizuela, P. Wachulak, D. H. Martz, W. Chao, E. H. Anderson, D. T. Attwood, A. V. Vinogradov, I. A. Artyukov, A. G. Ponomareko, V. V. Kondratenko, M. C. Marconi, J. J. Rocca, and C. S. Menoni, "Single-shot extreme ultraviolet laser imaging of nanostructures with wavelength resolution," *Opt. Lett.*, vol. 33, pp. 518–520, Mar 2008.

[5] F. Brizuela, Y. Wang, C. A. Brewer, F. Pedaci, W. Chao, E. H. Anderson, Y. Liu, K. A. Goldberg, P. Naulleau, P. Wachulak, M. C. Marconi, D. T. Attwood, J. J. Rocca, and C. S. Menoni, "Microscopy of extreme ultraviolet lithography masks with 13.2 nm tabletop laser illumination," *Opt. Lett.*, vol. 34, pp. 271–273, Feb 2009.

[6] M. Capeluto, G. Vaschenko, M. Grisham, M. Marconi, S. Luduena, L. Pietrasanta, Y. Lu, B. Parkinson, C. Menoni, and J. Rocca, "Nanopattern-

ing with interferometric lithography using a compact lambda=46.9-nm laser," *Nanotechnology, IEEE Transactions on*, vol. 5, pp. 3 – 7, jan. 2006.

[7] P. Wachulak, M. Grisham, S. Heinbuch, D. Martz, W. Rockward, D. Hill, J. J. Rocca, C. S. Menoni, E. Anderson, and M. Marconi, "Interferometric lithography with an amplitude division interferometer and a desktop extreme ultraviolet laser," *J. Opt. Soc. Am. B*, vol. 25, pp. B104–B107, Jul 2008.

[8] http://www.itrs.net/Links/2009ITRS/Home2009.htm, "International Technology Roadmap for Semiconductors 2009 Edition," 2009.

[9] P. Antoine, A. L'Huillier, and M. Lewenstein, "Attosecond pulse trains using high-order harmonics," *Phys. Rev. Lett.*, vol. 77, pp. 1234–1237, Aug 1996.

[10] G. Sansone, E. Benedetti, F. Calegari, C. Vozzi, L. Avaldi, R. Flammini, L. Poletto, P. Villoresi, C. Altucci, R. Velotta, S. Stagira, S. De Silvestri, and M. Nisoli, "Isolated single-cycle attosecond pulses," *Science*, vol. 314, no. 5798, pp. 443–446, 2006.

[11] F. Krausz and M. Ivanov, "Attosecond physics," *Rev. Mod. Phys.*, vol. 81, pp. 163–234, Feb 2009.

[12] S. Gordienko, A. Pukhov, O. Shorokhov, and T. Baeva, "Relativistic doppler effect: Universal spectra and zeptosecond pulses," *Phys. Rev. Lett.*, vol. 93, p. 115002, Sep 2004.

[13] G. Mourou and T. Tajima, "More intense, shorter pulses," *Science*, vol. 331, no. 6013, pp. 41–42, 2011.

[14] J. Jackson, *Classical Electrodynamics*. New York: Wiley, 3rd ed., 1998.

[15] W. Ackermann *et al.*, "Operation of a free-electron laser from the extreme ultraviolet to the water window," *Nature Photonics*, vol. 1, pp. 336–342, 2007.

[16] P. Emma *et al.*, "First lasing and operation of an angstrom-wavelength free-electron laser," *Nature Photonics*, vol. 4, pp. 641–647, 2010.

[17] T. Togashi, E. J. Takahashi, K. Midorikawa, M. Aoyama, K. Yamakawa, T. Sato, A. Iwasaki, S. Owada, T. Okino, K. Yamanouchi, F. Kannari, A. Yagishita, H. Nakano, M. E. Couprie, K. Fukami, T. Hatsui, T. Hara, T. Kameshima, H. Kitamura, N. Kumagai, S. Matsubara, M. Nagasono, H. Ohashi, T. Ohshima, Y. Otake, T. Shintake, K. Tamasaku, H. Tanaka, T. Tanaka, K. Togawa, H. Tomizawa, T. Watanabe, M. Yabashi, and T. Ishikawa, "Extreme ultraviolet free electron laser seeded with high-order harmonic of Ti:sapphire laser," *Optics Express*, vol. 19, p. 317, Jan. 2011.

[18] M. Lewenstein, P. Balcou, M. Y. Ivanov, A. L'Huillier, and P. B. Corkum, "Theory of high-harmonic generation by low-frequency laser fields," *Phys. Rev. A*, vol. 49, pp. 2117–2132, Mar 1994.

[19] K. S. K.C. Kulander and J. Krause, *Super-Intense Laser-Atom Physics*. Plenum, 1993.

[20] F. Irons and N. Peacock, "Experimental evidence for population inversion in C+5 in an expanding laser-produced plasma," *Journal of Physics B: Atomic and Molecular Physics*, vol. 7, p. 1109, 1974.

[21] D. Kim, C. H. Skinner, G. Umesh, and S. Suckewer, "Gain measurements at 18.22 nm in C VI generated by a Nd:glass laser," *Opt. Lett.*, vol. 14, pp. 665–667, Jul 1989.

[22] D. V. Korobkin, C. H. Nam, S. Suckewer, and A. Goltsov, "Demonstration of Soft X-Ray Lasing to Ground State in Li III," *Phys. Rev. Lett.*, vol. 77, pp. 5206–5209, Dec 1996.

[23] S. Suckewer, C. H. Skinner, H. Milchberg, C. Keane, and D. Voorhees, "Amplification of stimulated soft-X-ray emission in a confined plasma column," *Physical Review Letters*, vol. 55, pp. 1753–1756, Oct. 1985.

[24] W. T. Silfvast and O. R. Wood, "Photoionization lasers pumped by broadband soft-x-ray flux from laser-produced plasmas," *J. Opt. Soc. Am. B*, vol. 4, pp. 609–618, Apr 1987.

[25] H. C. Kapteyn and R. W. Falcone, "Auger-pumped short-wavelength lasers in xenon and krypton," *Phys. Rev. A*, vol. 37, pp. 2033–2038, Mar 1988.

[26] M. A. Duguay and P. M. Rentzepis, "Some approaches to vacuum uv and x-ray lasers," *Applied Physics Letters*, vol. 10, pp. 350–352, june 1967.

[27] T. S. Axelrod, "Inner-shell photoionization-pumped x-ray lasers. Sulfur," *Physical Review A*, vol. 13, pp. 376–382, Jan. 1976.

[28] H. C. Kapteyn, "Photoionization-pumped x-ray lasers using ultrashort-pulse excitation," *Appl. Opt.*, vol. 31, pp. 4931–4939, Aug 1992.

[29] N. Rohringer, D. P. Ryan, R. A. London, M. A. Purvis, J. Dunn, J. J. Rocca, F. Albert, R. Hill, and J. D. Bozek *Nature*, to be published.

[30] W. B. Bridges, "Laser Oscillation in Singly Ionized Argon in the Visible Spectrum," *Applied Physics Letters*, vol. 4, pp. 128–130, Apr. 1964.

[31] A. N. Zherikhin, K. N. Koshelev, and V. S. Letokhov, "Gain in the far vacuum ultraviolet region due to transitions in multiply charged ions," *Soviet Journal of Quantum Electronics*, vol. 6, no. 1, p. 82, 1976.

[32] A. V. Vinogradov and V. N. Shlyaptsev, "Calculations of population inversion due to transitions in multiply charged neon-like ions in the 200 2000 A range," *Soviet Journal of Quantum Electronics*, vol. 10, no. 6, p. 754, 1980.

[33] D. L. Matthews, P. L. Hagelstein, M. D. Rosen, M. J. Eckart, N. M. Ceglio, A. U. Hazi, H. Medecki, B. J. MacGowan, J. E. Trebes, B. L. Whitten, E. M. Campbell, C. W. Hatcher, A. M. Hawryluk, R. L. Kauffman, L. D. Pleasance, G. Rambach, J. H. Scofield, G. Stone, and T. A. Weaver, "Demonstration of a soft x-ray amplifier," *Phys. Rev. Lett.*, vol. 54, pp. 110–113, Jan 1985.

[34] B. J. MacGowan, L. B. da Silva, D. J. Fields, C. J. Keane, J. A. Koch, R. A. London, D. L. Matthews, S. Maxon, S. Mrowka, A. L. Osterheld, J. H. Scofield, G. Shimkaveg, J. E. Trebes, and R. S. Walling, "Short wavelength x-ray laser research at the Lawrence Livermore National Laboratory," *Physics of Fluids B*, vol. 4, pp. 2326–2337, July 1992.

[35] Y. V. Afanas'ev and V. N. Shlyaptsev, "Formation of a population inversion of transitions in ne-like ions in steady-state and transient plasmas," *Soviet Journal of Quantum Electronics*, vol. 19, no. 12, p. 1606, 1989.

[36] P. V. Nickles, V. N. Shlyaptsev, M. Kalachnikov, M. Schnürer, I. Will, and W. Sandner, "Short Pulse X-Ray Laser at 32.6 nm Based on Transient Gain in Ne-like Titanium," *Physical Review Letters*, vol. 78, pp. 2748–2751, Apr. 1997.

[37] J. Dunn, Y. Li, A. L. Osterheld, J. Nilsen, J. R. Hunter, and V. N. Shlyaptsev, "Gain Saturation Regime for Laser-Driven Tabletop, Transient Ni-Like Ion X-Ray Lasers," *Physical Review Letters*, vol. 84, pp. 4834–4837, May 2000.

[38] P. B. Corkum, "Plasma perspective on strong field multiphoton ionization," *Physical Review Letters*, vol. 71, pp. 1994–1997, Sept. 1993.

[39] S. Sebban, R. Haroutunian, P. Balcou, G. Grillon, A. Rousse, S. Kazamias, T. Marin, J. P. Rousseau, L. Notebaert, M. Pittman, J. P. Chambaret, A. Antonetti, D. Hulin, D. Ros, A. Klisnick, A. Carillon, P. Jaeglé, G. Jamelot,

and J. F. Wyart, "Saturated Amplification of a Collisionally Pumped Optical-Field-Ionization Soft X-Ray Laser at 41.8 nm," *Physical Review Letters*, vol. 86, pp. 3004–3007, Apr. 2001.

[40] S. Sebban, T. Mocek, D. Ros, L. Upcraft, P. Balcou, R. Haroutunian, G. Grillon, B. Rus, A. Klisnick, A. Carillon, G. Jamelot, C. Valentin, A. Rousse, J. P. Rousseau, L. Notebaert, M. Pittman, and D. Hulin, "Demonstration of a Ni-Like Kr Optical-Field-Ionization Collisional Soft X-Ray Laser at 32.8nm," *Physical Review Letters*, vol. 89, p. 253901, Nov. 2002.

[41] J. J. Rocca, V. Shlyaptsev, F. G. Tomasel, O. D. Cortázar, D. Hartshorn, and J. L. A. Chilla, "Demonstration of a discharge pumped table-top soft-x-ray laser," *Physical Review Letters*, vol. 73, pp. 2192–2195, Oct. 1994.

[42] B. R. Benware, C. D. Macchietto, C. H. Moreno, and J. J. Rocca, "Demonstration of a High Average Power Tabletop Soft X-Ray Laser," *Physical Review Letters*, vol. 81, pp. 5804–5807, Dec. 1998.

[43] J. Filevich, K. Kanizay, M. C. Marconi, J. L. A. Chilla, and J. J. Rocca, "Dense plasma diagnostics with an amplitude-division sof t-x-ray laser interferometer based on dif f raction gratings," *Optics Letters*, vol. 25, pp. 356–358, Mar. 2000.

[44] R. Keenan, J. Dunn, V. N. Shlyaptsev, R. F. Smith, P. K. Patel, and D. F. Price, "Efficient pumping schemes for high average brightness collisional x-ray lasers," in *Society of Photo-Optical Instrumentation Engineers (SPIE) Conference Series* (E. E. Fill, ed.), vol. 5197 of *Society of Photo-Optical Instrumentation Engineers (SPIE) Conference Series*, pp. 213–220, Dec. 2003.

[45] B. M. Luther, Y. Wang, M. A. Larotonda, D. Alessi, M. Berrill, J. J. Rocca, J. Dunn, R. Keenan, and V. N. Shlyaptsev, "High Repetition Rate Collisional

Soft X-Ray Lasers Based on Grazing Incidence Pumping," *IEEE Journal of Quantum Electronics*, vol. 42, pp. 4–13, Jan. 2006.

[46] R. Keenan, J. Dunn, P. K. Patel, D. F. Price, R. F. Smith, and V. N. Shlyaptsev, "High-Repetition-Rate Grazing-Incidence Pumped X-Ray Laser Operating at 18.9 nm," *Physical Review Letters*, vol. 94, p. 103901, Mar. 2005.

[47] B. M. Luther, Y. Wang, M. A. Larotonda, D. Alessi, M. Berrill, M. C. Marconi, J. J. Rocca, and V. N. Shlyaptsev, "Saturated high-repetition-rate 18.9-nm tabletop laser in nickellike molybdenum," *Optics Letters*, vol. 30, pp. 165–167, Jan. 2005.

[48] Y. Wang, M. A. Larotonda, B. M. Luther, D. Alessi, M. Berrill, V. N. Shlyaptsev, and J. J. Rocca, "Demonstration of high-repetition-rate tabletop soft-x-ray lasers with saturated output at wavelengths down to 13.9 nm and gain down to 10.9 nm," *Physical Review A*, vol. 72, p. 053807, Nov. 2005.

[49] D. Alessi, B. M. Luther, Y. Wang, M. A. Larotonda, M. Berrill, and J. J. Rocca, "High repetition rate operation of saturated tabletop soft x-ray lasers in transitions of neon-like ions near 30 nm," *Optics Express*, vol. 13, p. 2093, Mar. 2005.

[50] J. J. Rocca, Y. Wang, M. A. Larotonda, B. M. Luther, M. Berrill, and D. Alessi, "Saturated 13.2 nm high-repetition-rate laser in nickellike cadmium," *Optics Letters*, vol. 30, pp. 2581–2583, Oct. 2005.

[51] D. H. Martz, D. Alessi, B. M. Luther, Y. Wang, D. Kemp, M. Berrill, and J. J. Rocca, "High-energy 13.9 nm table-top soft-x-ray laser at 2.5 Hz repetition rate excited by a slab-pumped Ti:sapphire laser," *Optics Letters*, vol. 35, pp. 1632–+, May 2010.

[52] D. Alessi, D. H. Martz, Y. Wang, M. Berrill, B. M. Luther, and J. J. Rocca, "Gain-saturated 10.9 nm tabletop laser operating at 1 hz repetition rate," *Opt. Lett.*, vol. 35, pp. 414–416, Feb 2010.

[53] G. Vaschenko, C. Brewer, F. Brizuela, Y. Wang, M. A. Larotonda, B. M. Luther, M. C. Marconi, J. J. Rocca, C. S. Menoni, E. H. Anderson, W. Chao, B. D. Harteneck, J. A. Liddle, Y. Liu, and D. T. Attwood, "Sub-38 nm resolution tabletop microscopy with 13 nm wavelength laser light," *Optics Letters*, vol. 31, pp. 1214–1216, May 2006.

[54] Y. Wang, E. Granados, M. A. Larotonda, M. Berrill, B. M. Luther, D. Patel, C. S. Menoni, and J. J. Rocca, "High-Brightness Injection-Seeded Soft-X-Ray-Laser Amplifier Using a Solid Target," *Physical Review Letters*, vol. 97, p. 123901, Sept. 2006.

[55] F. Pedaci, Y. Wang, M. Berrill, B. Luther, E. Granados, and J. J. Rocca, "Highly coherent injection-seeded 13.2 nm tabletop soft x-ray laser," *Optics Letters*, vol. 33, p. 491, 2008.

[56] Y. Wang, E. Granados, F. Pedaci, D. Alessi, B. Luther, M. Berrill, and J. J. Rocca, "Phase-coherent, injection-seeded, table-top soft-X-ray lasers at 18.9 nm and 13.9 nm," *Nature Photonics*, vol. 2, pp. 94–98, Feb. 2008.

[57] H. Bravo, B. Szapiro, P. Watchulak, M. Marconi, W. Chao, E. Anderson, C. Menoni, and J. Rocca, "Demonstration of nanomachining with focused extreme ultraviolet laser beams," *Selected Topics in Quantum Electronics, IEEE Journal of*, vol. PP, no. 99, p. 1, 2011.

[58] D. Strickland and G. Mourou, "Compression of amplified chirped optical pulses," *Optics Communications*, vol. 56, pp. 219–221, Dec. 1985.

[59] R. Ell, U. Morgner, F. X. Kärtner, J. G. Fujimoto, E. P. Ippen, V. Scheuer, G. Angelow, T. Tschudi, M. J. Lederer, A. Boiko, and B. Luther-Davies, "Generation of 5-fs pulses and octave-spanning spectra directly from a Tisapphire laser," *Optics Letters*, vol. 26, pp. 373–375, Mar. 2001.

[60] Wikipedia, "Chirped pulse amplification," 2011.

[61] E. Treacy, "Optical pulse compression with diffraction gratings," *Quantum Electronics, IEEE Journal of*, vol. 5, pp. 454 – 458, sep 1969.

[62] O. Martinez, "3000 times grating compressor with positive group velocity dispersion," *Quantum Electronics, IEEE Journal of*, vol. 23, pp. 59 – 64, jan 1987.

[63] W. Koechner, *Solid-State Laser Engineering*. New York: Springer-Verlag, 6 ed., 2006.

[64] M. D. Perry, D. Pennington, B. C. Stuart, G. Tietbohl, J. A. Britten, C. Brown, S. Herman, B. Golick, M. Kartz, J. Miller, H. T. Powell, M. Vergino, and V. Yanovsky, "Petawatt laser pulses," *Optics Letters*, vol. 24, pp. 160–162, Feb. 1999.

[65] Coherent Inc., "Onyx mccp 1.6mm high power array," 2011.

[66] J. Tümmler, R. Jung, H. Stiel, P. V. Nickles, and W. Sandner, "High-repetition-rate chirped-pulse-amplification thin-disk laser system with joule-level pulse energy," *Optics Letters*, vol. 34, pp. 1378–+, Apr. 2009.

[67] F. J. Furch, B. A. Reagan, B. M. Luther, A. H. Curtis, S. P. Meehan, and J. J. Rocca, "Demonstration of an all-diode-pumped soft x-ray laser," *Opt. Lett.*, vol. 34, pp. 3352–3354, Nov 2009.

[68] S. Klingebiel, C. Wandt, C. Skrobol, I. Ahmad, S. A. Trushin, Z. Major, F. Krausz, and S. Karsch, "High energy picosecond Yb:YAG CPA system at 10

Hz repetition rate for pumping optical parametric amplifiers," *Optics Express*, vol. 19, p. 5357, Mar. 2011.

[69] K.-H. Hong, S.-W. Huang, J. Moses, X. Fu, C.-J. Lai, G. Cirmi, A. Sell, E. Granados, P. Keathley, and F. X. Kärtner, "High-energy, phase-stable, ultrabroadband kHz OPCPA at 2.1 μm pumped by a picosecond cryogenic Yb:YAG laser," *Opt. Express*, vol. 19, pp. 15538–15548, Aug 2011.

[70] C. Hönninger, I. Johannsen, M. Moser, G. Zhang, A. Giesen, and U. Keller, "Diode-pumped thin-disk Yb:YAG regenerative amplifier," *Applied Physics B: Lasers and Optics*, vol. 65, pp. 423–426, Sept. 1997.

[71] H. Liu, S. Biswal, J. Paye, J. Nees, G. Mourou, C. Hönninger, and U. Keller, "Directly diode-pumped millijoule subpicosecond Yb:glass regenerative amplifier," *Opt. Lett.*, vol. 24, pp. 917–919, Jul 1999.

[72] J. Kawanaka, K. Yamakawa, H. Nishioka, and K. ichi Ueda, "30-mJ, diode-pumped, chirped-pulse Yb:YLF regenerative amplifier," *Opt. Lett.*, vol. 28, pp. 2121–2123, Nov 2003.

[73] K. Ogawa, Y. Akahane, M. Aoyama, K. Tsuji, S. Tokita, J. Kawanaka, H. Nishioka, and K. Yamakawa, "Multi-millijoule, diode-pumped, cryogenically-cooled Yb:KY(WO4)2 chirped-pulse regenerative amplifier," *Opt. Express*, vol. 15, pp. 8598–8602, Jul 2007.

[74] Y. Akahane, M. Aoyama, K. Ogawa, K. Tsuji, S. Tokita, J. Kawanaka, H. Nishioka, and K. Yamakawa, "High-energy, diode-pumped, picosecond Yb:YAG chirped-pulse regenerative amplifier for pumping optical parametric chirped-pulse amplification," *Optics Letters*, vol. 32, pp. 1899–1901, July 2007.

[75] T. Metzger, A. Schwarz, C. Y. Teisset, D. Sutter, A. Killi, R. Kienberger, and F. Krausz, "High-repetition-rate picosecond pump laser based on a yb:yag disk

amplifier for optical parametric amplification," *Opt. Lett.*, vol. 34, pp. 2123–2125, Jul 2009.

[76] A. Pugžlys, G. Andriukaitis, D. Sidorov, A. Irshad, A. Baltuška, W. J. Lai, P. B. Phua, L. Su, J. Xu, H. Li, R. Li, S. Ališauskas, A. Marcinkevičius, M. E. Fermann, L. Giniūnas, and R. Danielius, "Spectroscopy and lasing of cryogenically cooled Yb, Na:CaF_2," *Applied Physics B: Lasers and Optics*, vol. 97, pp. 339–350, Oct. 2009.

[77] K. Ogawa, Y. Akahane, and K. Yamakawa, "100-mJ diode-pumped, cryogenically-cooled Yb:YLF chirped-pulse regenerative amplifier," in *CLEO:2011 - Laser Applications to Photonic Applications*, p. CMB4, Optical Society of America, 2011.

[78] A. H. Curtis, B. A. Reagan, K. A. Wernsing, F. J. Furch, B. M. Luther, and J. J. Rocca, "Demonstration of a compact 100 Hz, 0.1 J, diode-pumped picosecond laser," *Optics Letters*, vol. 36, p. 2164, June 2011.

[79] D. Rand, D. Miller, D. J. Ripin, and T. Y. Fan, "Cryogenic yb3+-doped materials for pulsed solid-state laser applications," *Opt. Mater. Express*, vol. 1, pp. 434–450, Jul 2011.

[80] D. N. Papadopoulos, A. Pellegrina, L. P. Ramirez, P. Georges, and F. Druon, "Broadband high-energy diode-pumped Yb:KYW multipass amplifier," *Opt. Lett.*, vol. 36, pp. 3816–3818, Oct 2011.

[81] D. Brown, R. Cone, Y. Sun, and R. Equall, "Yb:yag absorption at ambient and cryogenic temperatures," *Selected Topics in Quantum Electronics, IEEE Journal of*, vol. 11, pp. 604 – 612, may-june 2005.

[82] L. D. Deloach, S. A. Payne, L. L. Chase, L. K. Smith, W. L. Kway, and W. F. Krupke, "Evaluation of absorption and emission properties of Yb(3+) doped

crystals for laser applications," *IEEE Journal of Quantum Electronics*, vol. 29, pp. 1179–1191, Apr. 1993.

[83] J. E. Geusic, H. M. Marcos, and L. G. van Uitert, "Laser Oscillations in Nd-DOPED Yttrium Aluminum, Yttrium Gallium and Gadolinium Garnets," *Applied Physics Letters*, vol. 4, pp. 182–184, May 1964.

[84] G. A. Slack, D. W. Oliver, R. M. Chrenko, and S. Roberts, "Optical Absorption of $Y_3Al_5O_{12}$ from 10- to 55 000-cm^{-1} Wave Numbers," *Physical Review*, vol. 177, pp. 1308–1314, Jan. 1969.

[85] R. L. Aggarwal, D. J. Ripin, J. R. Ochoa, and T. Y. Fan, "Measurement of thermo-optic properties of Y3Al5O12, Lu3Al5O12, YAIO3, LiYF4, LiLuF4, BaY2F8, KGd(WO4)2, and KY(WO4)2 laser crystals in the 80-300 K temperature range," *Journal of Applied Physics*, vol. 98, pp. 103514 –103514–14, nov 2005.

[86] J. Dong, M. Bass, Y. Mao, P. Deng, and F. Gan, "Dependence of the Yb^{3+} emission cross section and lifetime on temperature and concentration in yttrium aluminum garnet," *Journal of the Optical Society of America B Optical Physics*, vol. 20, pp. 1975–1979, Sept. 2003.

[87] K.-H. Hong, J. T. Gopinath, D. Rand, A. M. Siddiqui, S.-W. Huang, E. Li, B. J. Eggleton, J. D. Hybl, T. Y. Fan, and F. X. Kärtner, "High-energy, kHz-repetition-rate, ps cryogenic Yb:YAG chirped-pulse amplifier," *Optics Letters*, vol. 35, p. 1752, May 2010.

[88] H. Liu, J. Nees, and G. Mourou, "Diode-pumped Kerr-lens mode-locked YbKY(WO 4) 2 laser," *Optics Letters*, vol. 26, pp. 1723–1725, Nov. 2001.

[89] F. Brunner, T. Sudmeyer, E. Innerhofer, F. Morier-Genoud, R. Paschotta, V. E. Kisel, V. G. Shcherbitsky, N. V. Kuleshov, J. Gao, K. Contag, and

U. Keller, "240-fs pulses with 22-W average power from a mode-locked thin-disk Yb:KY(WO4)2 laser," *Optics Letters*, vol. 27, pp. 1162–1164, July 2002.

[90] U. Keller, K. Weingarten, F. Kartner, D. Kopf, B. Braun, I. Jung, R. Fluck, C. Honninger, N. Matuschek, and J. Aus der Au, "Semiconductor saturable absorber mirrors (sesam's) for femtosecond to nanosecond pulse generation in solid-state lasers," *Selected Topics in Quantum Electronics, IEEE Journal of*, vol. 2, pp. 435 –453, sep 1996.

[91] V. Pervak, C. Teisset, A. Sugita, S. Naumov, F. Krausz, and A. Apolonski, "High-dispersive mirrors for femtosecond lasers," *Optics Express*, vol. 161, pp. 10220–+, June 2008.

[92] G. Cheriaux, P. Rousseau, F. Salin, J. P. Chambaret, B. Walker, and L. F. Dimauro, "Aberration-free stretcher design for ultrashort-pulse amplification," *Optics Letters*, vol. 21, pp. 414–416, Mar. 1996.

[93] D. Brown, J. Kelly, and J. Abate, "Active-mirror amplifiers: Progress and prospects," *Quantum Electronics, IEEE Journal of*, vol. 17, pp. 1755 – 1765, sep 1981.

[94] A. Giesen and J. Speiser, "Fifteen years of work on thin-disk lasers: Results and scaling laws," *Selected Topics in Quantum Electronics, IEEE Journal of*, vol. 13, pp. 598 –609, may-june 2007.

[95] C. R. E. Baer, C. Kränkel, C. J. Saraceno, O. H. Heckl, M. Golling, R. Peters, K. Petermann, T. Südmeyer, G. Huber, and U. Keller, "Femtosecond thin-disk laser with 141 W of average power," *Optics Letters*, vol. 35, p. 2302, June 2010.

[96] R. Paschotta, J. Aus der Au, G. J. Spühler, S. Erhard, A. Giesen, and U. Keller, "Passive mode locking of thin-disk lasers: effects of spatial hole burning," *Applied Physics B: Lasers and Optics*, vol. 72, pp. 267–278, 2001.

[97] M. Kida, Y. Kikuchi, O. Takahasi, and I. Michiyoshi, "Pool-Boiling Heat Transfer in Liquid Nitrogen," *Journal of Nuclear Science and Technology*, vol. 18, pp. 501–513, 1981.

[98] H. Furuse, J. Kawanaka, K. Takeshita, N. Miyanaga, T. Saiki, K. Imasaki, M. Fujita, and S. Ishii, "Total-reflection active-mirror laser with cryogenic Yb:YAG ceramics," *Optics Letters*, vol. 34, p. 3439, Oct. 2009.

[99] Y. Takeuchi, J. Kawanaka, A. Yoshida, R. Yasuhara, T. Kawashima, H. Kan, and N. Miyanaga, "Sub-khz cryogenic yb:yag regenerative amplifier by using a total-reflection active mirror," *Applied Physics B: Lasers and Optics*, vol. 104, pp. 29–32, 2011. 10.1007/s00340-010-4366-2.

[100] R. Winston, *Nonimaging Optics*. Boston: Elsevier, 2005.

[101] L. M. Frantz and J. S. Nodvik, "Theory of pulse propagation in a laser amplifier," *Journal of Applied Physics*, vol. 34, pp. 2346 –2349, aug 1963.

[102] D. Albach, J.-C. Chanteloup, and G. L. Touzé, "Influence of ASE on the gain distribution in large size, high gain Yb^3+:YAG slabs," *Optics Express*, vol. 17, p. 3792, Feb. 2009.

Appendix A

Amplified Spontaneous Emission Simulations

A.1 Introduction

Amplified spontaneous emission (ASE) and parasitic lasing present a major limitation in achievable energy storage and gain of large volume, high energy amplifiers. These problems are further exacerbated when thermally efficient disk amplifiers with low aspect ratios are used due to the large transverse gain. In order to design efficient high energy amplifiers parasitic lasing must be mitigated and the effects of ASE must be take into account. We have developed a three dimensional numerical simulation that calculates the stored energy and gain distributions of solid state amplifiers in the presence of ASE for arbitrary pump profiles in both time and space. We have also developed a post-processor that models the amplifier performance when injected with a seed of arbitrary energy and spatial profile using the results of the energy storage simulation [101]. In this appendix, these models are compared to the corresponding experimental results obtained with the amplifiers presented in Chapter 2.

A.2 Model Description

The model is constructed in a similar manner to that reported in [102]. The rate equation for the laser upper level population density, n, is:

$$\frac{dn}{dt} = \frac{P/V}{h\nu} - \frac{n}{\tau} + \Phi_{\mathrm{ASE}}[\sigma_{\mathrm{a}}(n_{\mathrm{tot}} - n) - \sigma_{\mathrm{e}} n], \tag{A.1}$$

where P/V is the pump power density, hν is the pump photon energy, τ is the fluorescence lifetime of the laser upper level, Φ_{ASE} is the photon flux of amplified spontaneous emission, σ_{a} and σ_{e} are the absorption and stimulated emission cross sections at the emission center wavelength respectively, and $\mathrm{n_{tot}}$ is the total density of lasing atoms (doping density). The first term is the density of pump photons absorbed, the second represents spontaneous emission, and the final term is the absorption and stimulated emission of ASE. The model solves the rate equation in temporal steps at all points within the laser volume. The laser medium is divided into a mesh of cubic cells. The main computation is in the evaluation of the ASE flux, Φ_{ASE}. This is computed by evaluating the following integral for each cell:

$$\Phi_{\mathrm{ASE}}(\vec{r_0}) = \int \frac{1}{4\pi \quad \rho(\vec{r}, \vec{r_0})^{\ 2}} \frac{n(\vec{r})}{\tau} G(\vec{r} \qquad \vec{r_0}) dV. \tag{A.2}$$

The term in the integral is the ASE flux at point $\vec{r_0}$ originating from spontaneous emission at point $\vec{r}$ which are separated by a distance ρ and $G(\vec{r} \qquad \vec{r_0})$ is the gain between the points. By integrating over the entire volume the total ASE flux at $\vec{r_0}$ is obtained. In the model this integral is solved numerically by transforming this into a summation. As this summation must be done for each cell and at each time step this is a fairly computationally heavy calculation. In order to reduce the run time, the simulation can be run using the Monte Carlo integration numerical technique, in which the integrand is only explicitly evaluated at a few random points in the

volume and result of the integration is obtained by assuming these few points are representative of the volume as a whole. For relatively uniform pumping without large amounts ASE, a good result can be obtained with a very small number of Monte Carlo points.

For each time step, the model calculated the population inversion density at all points in the volume by solving the evaluating the following expression derived from the rate equation above:

$$n(x,y,z,t) = n(x,y,z,t-\Delta t)+\Delta t\left(\frac{P/V}{h\nu}-\frac{n(x,y,z,t-\Delta t)}{\tau}-\Phi_{\mathrm{ASE}}\sigma_{\mathrm{e}}n(x,y,z,t-\Delta t)\right), \tag{A.3}$$

where Δt is the time step. The ASE flux is derived from the integral above and the pumping density is a given parameter.

The assumptions made in this model are:

- The gain medium is uniform everywhere, there is no change in doping or other physical parameters such as the stimulated emission cross section. This is a good approximation for most solid state lasers, however as the stimulated emission cross section of cryogenically-cooled Yb:YAG changes quickly with temperature, very high average power operation may deviate from the model.

- The model is not spectrally resolved. It assumes all spontaneous emission is emitted at the center wavelength. This is an acceptable approximation for narrow bandwidth materials, however, it does overestimate the effects of ASE.

- In order to calculate the gain term when evaluating the ASE flux, the gain coefficient is assumed to be the average of the values at $\vec{r_0}$ and $\vec{r}$. This simplifies the calculation enormously by avoiding ray-tracing or other radiation transport calculations. This is a good approximation when the pumping is relatively uniform.

- For our purposes absorption of spontaneous emission is neglected as it is not important for 4-level systems. However, it would be easy to include.

- Most reflections from the edges or faces of the gain medium are neglected. For our absorbing-cladding crystals this is acceptable. In order to take into account the active mirror reflection the model assumes a mirror image of the gain medium side by side which takes into account the reflection of ASE on the HR surface.

A.3 Simulation Results

A.3.1 100 mJ Cryogenic Yb:YAG Amplifier

Figure A.1 shows the results generated from the ASE model when simulating the 100 mJ-level cryogenic Yb:YAG amplifier presented in Chapter 2. A cell size of 100 μm and temporal step of 100 μs were used in the model. Assuming the pump parameters used in the actual experiment a total of 180 mJ is stored in the amplifier with a single pass small signal gain of 4.9, in good agreement with the actual single-pass gain. As can be seen from this figure, ASE is not a large factor for this small beam size. Maps of the single pass gain, ASE flux and the transverse and longitudinal pump profiles are illustrated in the figure. Figure A.2 shows the simulated amplification of a 2.4 mJ seed making four passes through this stored energy profile. The simulated pulse energy of 160 mJ agrees well with the measured pulse energy of 152 mJ at 10 Hz repetition rate after 4 passes. Additionally, the amplification model predicts a peak fluence of $\approx$1.4 J/cm^2 in a fairly uniform beam.

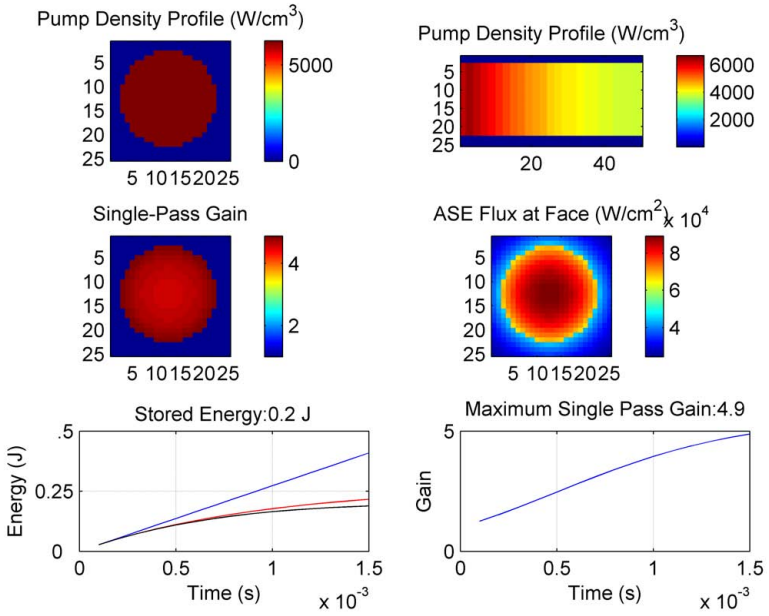

Figure A.1: Results of the simulation of the stored Energy in the 100 mJ-level cryogenic amplifier described in Chapter 2. The top two maps show the transverse and longitudinal pump density profiles. The middle maps show the a map of the single pass gain and the ASE flux at one face of the gain medium. The blue, red, and black lines represent the total pump energy absorbed taking into account the quantum defect, stored energy neglecting ASE, stored energy with ASE, respectively.

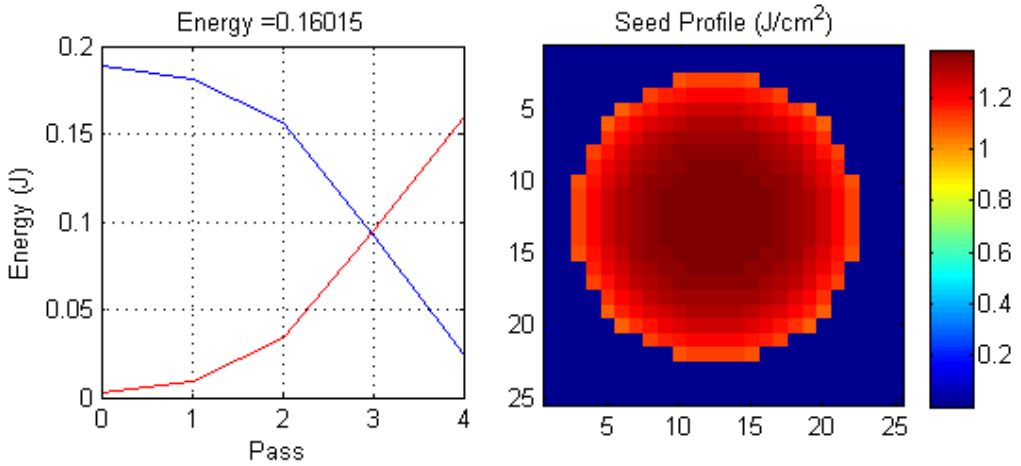

Figure A.2: Simulated amplification of a 2.4 mJ seed pulse under the pump conditions above. The red trace shows the pulse energy for each pass while the blue line shows the remaining stored energy. The figure on the right shows a map of the fluence of the amplified pulses.

A.3.2 Joule-Level Cryogenic Yb:YAG Amplifier

Figure A.3 shows the model results for the main power amplifier described in Chapter 2. Each crystal was assumed to be pumped by a 4 kW peak power pulses with a spot diameter of 17 mm, matching the experimental operation of the amplifier at the maximum pump power. The cell size was 200 μm and the time step was 100 μs. Monte Carlo integration with 200 points per integration was used in this run, as can be seen from the ASE flux map showing a non-physical variation in intensity. However, these fluctuations in the flux are not significant enough to influence the

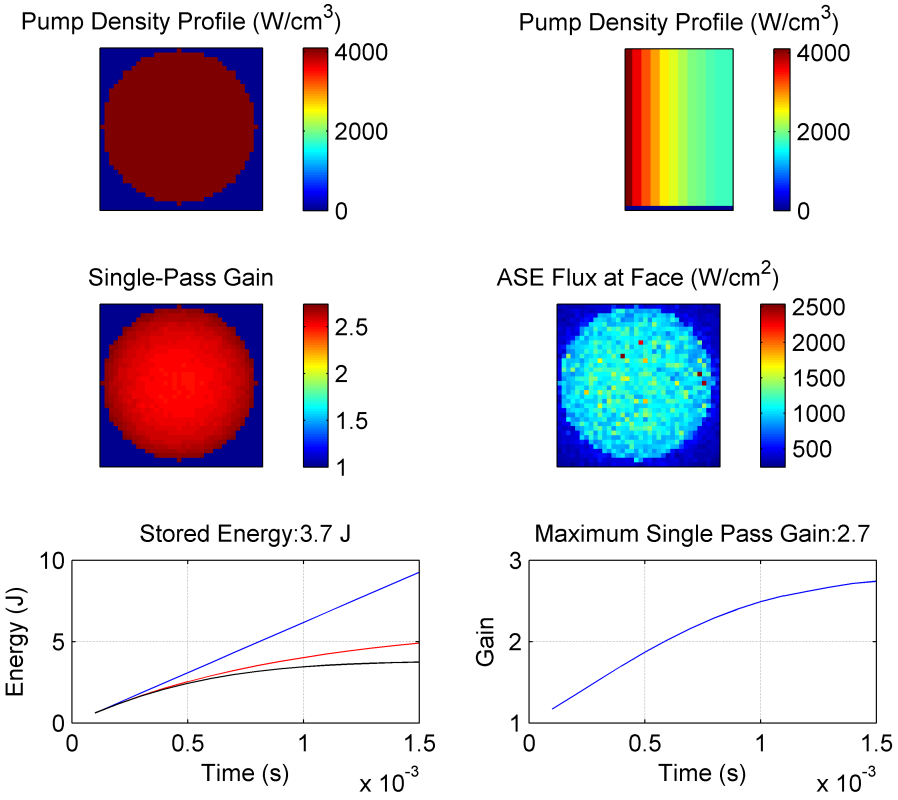

Figure A.3: Results of the simulation of the stored Energy in the Joule-level cryogenic amplifier described in Chapter 2. The top two maps show the transverse and longitudinal pump density profiles. The middle maps show the a map of the single pass gain and the ASE flux at one face of the gain medium. The blue, red, and black lines represent the total pump energy absorbed taking into account the quantum defect, stored energy neglecting ASE, stored energy with ASE for the two crystals combined that constitute this amplifier.

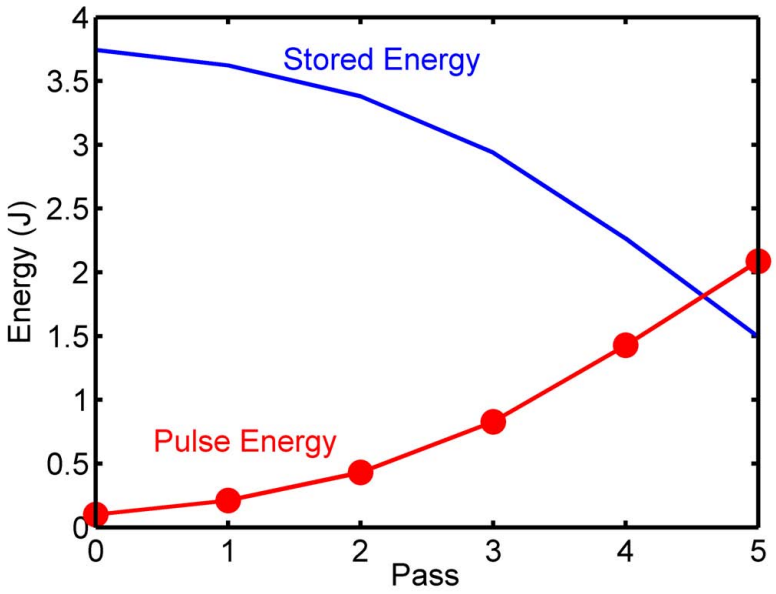

Figure A.4: Simulated Amplification of 100 mJ seed pulses to the Joule level. After 5 passes the simulation predicts a pulse energy of 2.1 J, in close agreement with the experimentally measured value of 2.0 J.

results as can be seen from the smooth gain profile. This simulation was completed in less than 10 minutes on a standard PC. In this large gain medium, the model predicts that ASE causes a non-negligible ≈20% reduction in stored energy. A stored energy of 3.7 J is obtained with a maximum single pass gain of 2.7, which is in agreement with the experimentally measured small signal gain. Figure A.4 shows the simulated amplification of 100 mJ energy pulses in this amplifier. Assuming the measured loss and a closely mode-matched beam size, the pulse attains an energy of 2.1 J in 5 passes through the gain medium. This is in excellent agreement with the measured 2 J pulses.

A comparison of the measured and simulated amplified pulse energy obtained as a function of peak pump power is shown in Figure A.5. To obtain the simulated data points the model was run with several different peak pump powers. This plot shows that the simulation is in good agreement with the measured values over a wide range of pump powers. These include regimes at low pump power where ASE is not

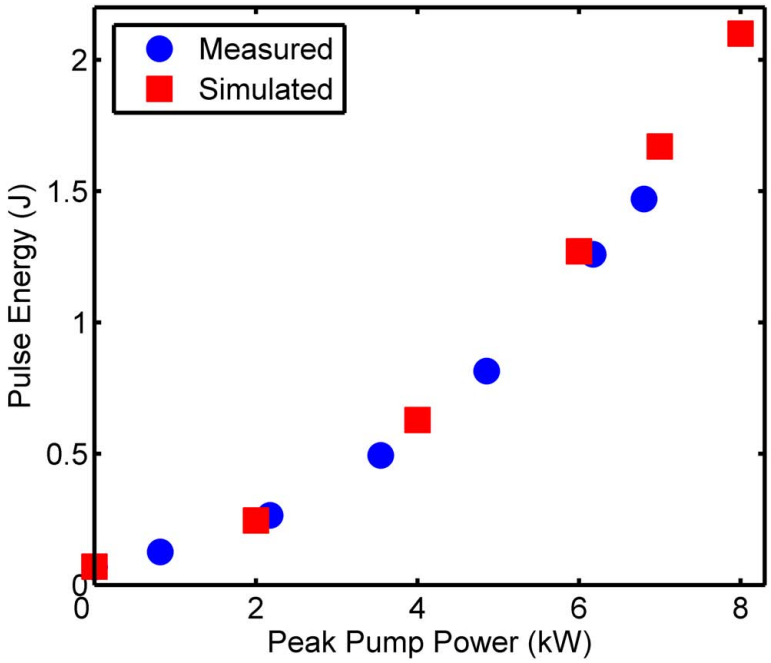

Figure A.5: Simulated and experimentally measured pulse energy obtained from the Joule-level amplifier as a function of peak pump power. For both the experiment and the simulation the amplifier was pumped with 1.5 ms duration pulses and was seeded with 100 mJ laser pulses. The measured data was obtained at 100 Hz repetition rate. The measured optical loss was used in the model.

significant and at high gain where ASE depletes the stored energy.